Majorana Zero Modes: investigating implementations of nanowire/superconductor setups

by

Malcolm J. A. Jardine

MPhys, University of Strathclyde, 2017

Submitted to the Graduate Faculty of

the Dietrich School of Arts and Sciences in partial fulfillment

of the requirements for the degree of

Doctor of Philosophy

University of Pittsburgh

2023

UNIVERSITY OF PITTSBURGH

DEPARTMENT OF PHYSICS AND ASTRONOMY

This dissertation was presented

by

Malcolm J. A. Jardine

It was defended on

July 14th 2023

and approved by

Sergey Frolov, Professor, University of Pittsburgh

Noa Marom, Professor, Carnegie Mellon University

Ayres Frietas, Professor, University of Pittsburgh

Roger Mong, Associate Professor, University of Pittsburgh

Thomas Purdy, Assistant Professor, University of Pittsburgh

Majorana Zero Modes: investigating implementations of nanowire/superconductor setups

Malcolm J. A. Jardine, PhD

University of Pittsburgh, 2023

This thesis aims to address some of the open questions surrounding the 1D semiconductor-nanowire/ superconductor hybrid system for investigating Majorana Zero Modes (MZMs), with focus on Ab Initio calculation of electronic properties of the semiconductor/superconductor interface and magnetic field implementation. MZMs are zero-energy states localized near boundaries of 1D and 2D topological superconductors. They are of interest due to their potential use as topologically protected qubits for fault-tolerant quantum computing. The semiconductor/ superconductor system, also called the hybrid system, could act as an effective p-wave superconductor which would harbor these MZM states. This platform has many open questions: such as which materials are best to use, requiring tools such as density functional theory; and how to best implement the magnetic field, possibly done using micro-scale magnets.

The first topic of this thesis is how Density Functional Theory (DFT) is employed to investigate the effects of interfacing materials relevant to these hybrid system MZM experiments. DFT is a computational approach used to approximately solve the electronic structure of condensed phase problems. We consider the materials α-Sn, InSb and CdTe, among others. We investigate, using the DFT+U method, inserting a CdTe tunnel barrier as the proximity to the superconductor could adversely affect InSb's properties. The results of DFT+U(BO) are validated against ARPES experiments for α-Sn and CdTe. It is found that 16 monolayers ($\sim$ 3.5 nm) of CdTe provides an effective barrier between the InSb/α-Sn interface.

Following this we investigate the need of relatively high external magnetic fields, that also changes direction for T-junction nanowire setups, in the MZM experimental approach. We propose devices that incorporate micromagnets to address this challenge. Numerical simulations of stray magnetic fields from micromagnet configurations are performed within

the micromagnetic simulation software of MuMax3. This is combined with an effective MZM hybrid model and solved to find Majorana wavefunctions in the system. The devices proposed start with a four-magnet design to align magnetic field with the nanowire, and then scales up to nanowire T-junctions, where micromagnets provide the required magnetic field. The feasibility of the approach is assessed by performing magnetic imaging of prototype patterns.

Keywords: Majorana Zero Mode (MZM), semiconductor-nanowire/ superconductor hybrid device, density functional theory (DFT), electronic structure, angle resolved photoemission spectroscopy (ARPES), metal-semiconductor interface, Metal Induced Gap States (MIGS), tunnel barrier, InSb, CdTe, Sn, micromagnets.

Table of Contents

List of Figures

Dedication

I dedicate this to my Gran, for her love and support throughout my PhD and life. Your generosity allowed me to travel back home many times over the years, which is something I will always be thankful for.

Figure 0.1:

Preface

I am extremely grateful to my Ph.D. advisor, Sergey Frolov, for his guidance and his support during my graduate studies. I appreciate that, while he is an experimentalist, he was able to find a space in his group for a theorist such as myself, he made me feel welcome and feel like I was part of the group. I enjoyed working within his group, and greatly appreciate him giving me the necessary freedom and also guidance to complete my Ph.D. Through his connections, I was then put in contact with Noa Marom of CMU, who also deserves my deep gratitude for welcoming me into her group and guiding me through my DFT projects. I have greatly enjoyed working with her, Derek and the rest of her team. I appreciate their teachings and collaborative efforts over the last 3 years, from which I have become the physicist I am today. It is through this work with Noa that I learnt where my efforts are best served, working with large simulations and bringing together many different ideas and people to work for a common goal. My collaborators also deserve mention, in particular those of Chris Palmstrøm and Moïra Hocevar and their students, as well as students from Frolov lab, from whom I have learned and gained a great deal from. I also thank all of my committee members for their constructive feedback and guidance. Additionally, I would like to express my gratitude to my course instructors at Pitt and CMU, who helped teach me the necessary physics to progress in my work. I have really enjoyed my time at the University of Pittsburgh, and will always remember my years here very fondly.

Lastly, I can't begin to express my gratitude towards my parents, my gran, my whole family and Anna who have always supported me with the love and help that got me through my Ph.D. I also need to thank my friends in Scotland and Pittsburgh, particularly those in my cohort as we went through this process together, who have always been there for me to laugh, cry, drink, and everything in between during my years in Pittsburgh.

1.0 Introduction

Over the past 50 years the promise of quantum computing has been touted as a way to revolutionise the way we perform certain classes of computations. Some areas that stand to benefit are optimization problems such as financial modeling and route optimization; medical applications such as drug discovery and simulating of protein folding; the protection and dissemination of data via encryption; and the simulation of quantum systems which help understand and probe the world we live in [8, 9]. However, simulating a quantum system on a classical one is an inherently difficult task, and improving our methods is an important goal for modern technology. Two example applications of quantum systems that could affect our everyday life are how to improve battery technology and how to make better clocks for navigation purposes [10, 11]. To tackle such problems a new generation of quantum tools are required, with a promising route being developing and improving quantum computers.

At its core, a quantum computer uses quantum bits (or qubits) in place of standard electronic bits, and unitary operations in place of transistor based logic gates. A qubit is just a two level quantum system, like the spin of an electron which can be up or down, or the ground and excited states in a superconducting qubit. These quantum bits can encode the usual binary information of 1's and 0's. However, they can also be in a superposition of a 1 and 0 state. The use of this new logic channel allows quantum computers to arrive at solutions to certain classes of problems much faster than classical computers. There are problems that are intractable on classical computers because it would take impossibly long to solve them, but can be done relatively quickly on a quantum computer. [9]. To this end, there are currently quantum computers with 100's of qubits with sufficiently high fidelity to perform useful calculations, which are approaching the quantum advantage limit [12]. That is, the point where a programmable quantum device can solve a problem that no classical computer could solve in any reasonable time period. However, there are still enormous technological hurdles to overcome in making programmable quantum computers and scaling up the number of qubits. One of the the most pressing issues is that of decoherence, i.e. a quantum system's ability to hold the useful quantum information in it's state.

One idea for how to tackle this issue is to use topological qubits, due to their promise of improving the reliability of quantum computations [13, 14, 15, 16, 17]. A topological qubit would be immune to small or adiabatic perturbations to the state, and thus protect the encoded information compared to current qubit implementations. The topology of a state can be compared to the often used example of a ball and a doughnut, where small perturbations to a ball will not transform the system into the doughnut. It is only a large change to the system, i.e. changing its topology, that can transform one into the other. This leads researchers to search for such topological states that can be used for quantum computation, and one of the most promising avenues for topological qubits are that of Majorana Zero Modes (MZMs). MZMs are zero-energy energy quasiparticle states that are localized near the boundaries and topological defects of one-and two-dimensional topological superconductors [18, 19, 20, 21]. There are several different platforms that are hypothesized to harbour these states, and we will be investigating one of the most promising platforms of the semiconductor-nanowire/superconductor hybrid system [22]. This system combines the nanowire's inherently strong spin-orbit coupling with proximity-induced s-wave superconductivity, via contact with conventional superconductors, and also an magnetic field, to allow the system to act an effective p-wave superconductor that could harbour these MZM states.

The search into the platforms that could harbour such topological states is a very active area of research with many open questions. One of the most pressing is how can experimental systems be engineered so these states, such as Majorana Zero Modes, can be observed and controlled. One important avenue of study is how the implemented materials affect this system, with experimental and theoretical research required to answer questions such what is the electron density in relevant materials, how can nanowires be effectively grown, and what happens when two materials are interfaced? One way to theoretically tackle the last of these questions is to use Density functional theory calculations.

Density functional theory (DFT) is the workhorse of first principles electronic structure simulations, and relies on approximate exchange-correlation functionals to describe the many-body quantum mechanical interactions between electrons. This method is Ab Initio, or from first principles, such that it does not rely on empirical parameters. It is used to

investigate the electronic structure, calculating properties such as the band structure and the density of states, of relatively large quantum mechanical systems (10s to 100s of atoms) that can represent bulk and finite crystal structures. It does this by considering the electronic density and therefore only having dimensionality 3 (x,y,z). This is in contrast to using the wave function to investigate the system, which is an extremely complicated object with dimensionality equal to 3N, where N is the amount of electrons in the system, and has a Hilbert space that grows exponentially with the number of electrons. DFT can then perform energy minimisation to access all the required properties of the system. This allows qualitative and quantitative results to compare or even precede experiments, such that the complete relevant search space doesn't need to be investigated in experimental setups.

This thesis is laid out as follows. In section 2 it describes what MZMs are, the topological superconductor model where they were first described, the promising experimental platform of the hybrid semiconductor/superconductor where MZM could be found and manipulated, and lastly touch on why these are relevant to quantum computing. Section 3 discusses the relevant details of density functional theory and describes the Bayesian optimization implementation to obtain the Hubbard U parameters. Section 4 details the work that implements DFT to understand the electronic effects of adding a CdTe barrier between semiconductor/metal interface of InSb/α-Sn. The use of Hubbard U corrections is also discussed, whose values are machine-learned via Bayesian optimization (BO) and are added to certain atomic orbitals of the materials as this can improve the accuracy of the relevant electronic properties while not significantly increasing computational cost. This section also discusses the methods used and results obtained for comparing the DFT data to experimental ARPES data for α-Sn and CdTe. Additionally, the ongoing work of implementing ZnTe and CdSe barriers between the InAs/Al interface is presented. Section 5 is the other part of this thesis's work, which is the numerical simulations of stray magnetic fields from different micro-scale magnets in various configurations. The fields are then used to solve for Majorana wavefunctions in a hybrid semiconductor/superconductor model which is done for straight and T-junction nanowire setups.

2.0 Majorana:

2.1 Theory

We have presented Majorana states as a possible qubit, but what are they? A good place to start is to consider their history. They were first proposed by Ettore Majorana, in the late 1930s, by modifying the Dirac equation such that it has real solutions [23]. The Dirac equation is a relativistic wave equation that describes spin half particles, such as electrons, bringing together quantum mechanics and relativity, explaining phenomena such as the fine structure of the hydrogen spectrum. Following this, with Majorana obtaining real solutions from derivative Majorana equation, he introduced a new particle which has been dubbed the "Majorana fermion". These proposed particles are real under complex conjugation, and therefore describe electrically neutral particles. Since then it has been hypothesized that neutrinos are Majorana fermions with this still being an active area of research. However, while they were first encountered in particle physics, of relevance here is their condensed matter comparison, which were first proposed in condensed matter models around 2000.

For reasons that will be discussed, in condensed matter systems the term that is used to discuss these states are Majorana bound states, or Majorana zero modes (MZMs). This is because they are fundamentally different to Ettore Majorana's proposed fermionic particles, as Majorana zero modes are quasiparticle states that are non-abelian anyons, not Fermions. A quasiparticle state is a non-fundamental object that is made of other particles acting as a collective and can then be mathematically described as particle. Additionally, MZMs appear in different situations than Majoranas in particle physics, as MZMs appear in low-dimensional and low-energy systems.

Now, some concrete mathematical descriptions for Majoranas will be presented. First, we consider the usual Dirac fermion operators that are often used in condensed matter physics, or, in the language of second quantization, the fermionic annihilation (holes) and creation operators (electrons). In general, these are described by $c_\alpha(p)$ and $c_\alpha^\dagger(p)$, where $c_\alpha(p)$ destroys a fermion at some position or momentum p and state α (e.g. spin, site), and

$c_\alpha^\dagger(p)$ creates a fermion at position or momentum p and state α. These follow the fermionic anticommutation relation of

$$\left\{c_\alpha(p), c_\beta^\dagger(p)\right\} = \delta_{\alpha,\beta}. \tag{1}$$

This is a natural way to describe electrons and holes in condensed matters systems, such as fermions moving around and interacting in a lattice model.

Following this, dropping the label of p and α for clarity, we can define Majorana fermion operators as

$$\gamma_1 = c + c^\dagger \qquad \gamma_2 = i\left(c - c^\dagger\right), \tag{2}$$

and it can be seen that these operators are real, i.e. $\gamma_i^\dagger = \gamma_i$, and obey the commutation relation $\{\gamma_i, \gamma_j\} = 2\delta_{i,j}$ to maintain the usual Dirac fermion commutation relations. We can also express the Dirac fermion operators in terms of the Majorana operators as

$$c = \tfrac{1}{2}(\gamma_1 - i\gamma_2) \qquad c^\dagger = \tfrac{1}{2}(\gamma_1 + i\gamma_2). \tag{3}$$

Note that so far nothing has fundamentally changed, this is a unitary transformation and therefore is always allowed. However, taking a look at this equation some insight can already be gained on what Majoranas are. In a condensed matter system this suggests that the Majorana fermions are composed of superpositions of electrons and holes, or, on the other hand, this could interpreted as a single fermion being composed of two Majoranas. This will become more apparent in the following section where a system with Majoranas that compose a single fermionic state are spatially separated. The next step is to introduce a system where these states appear and to show how this transformation offers some useful insight.

2.2 Majorana Kitaev Chain Model

Majoranas were first theoretically investigated in condensed matter systems in 2001 by Kitaev. He proposed the following model of a one-dimensional, topological p-wave superconductor [24]. This is a toy model, particularly as it uses spinless fermions (spin label is

suppressed) which are not something readily available in nature. The Kitaev chain Hamiltonian for an n-site system is

$$\hat{H} = -\mu \sum_{i=1}^{n} \left[c_i^\dagger c_i \right] - \frac{1}{2} \sum_{i=1}^{n-1} \left[t c_i^\dagger c_{i+1} - \Delta e^{i\phi} c_i c_{i+1} + H.c. \right], \tag{4}$$

which has c_i that destroys a spinless fermion at site i, $c_i^\dagger$ creates a spinless fermion, μ is the chemical potential, $t > 0$ is the site hopping energy and $\Delta e^{i\phi}$ is the phase dependent p-wave superconducting pairing term, which can be set to $\phi = 0$ without loss of generality. The superconducting pairing potential couples electrons on neighboring sites with the same spin, which departs from s-wave which couples electrons with opposite spin on the same site. The lack of spin also leads this model to breaks time-reversal symmetry. The model is depicted in Figure 2.1 (top), where μ can be described as the energy of a fermion occupying the site, or the energy for having two Majoranas on the same site. Similarly, the hopping and and nearest neighbour superconducting term can be viewed as the interaction energy of Majoranas on different sites. Black boxes represent how a Dirac fermion is composed of two Majorana operators on the same site. The middle panel depicts the trivial regime, where all Majoranas are paired with each other on the same site,

To find the unpaired zero energy Majoranas modes in this model we take the following limit of $t = \Delta$ and $\mu = 0$, which is just to make it mathematically straightforward to explicitly write down the MZMs. The physical meaning of this could mean that no energy is required for electron occupancy (or equivalently no energy penalty for two Majoranas on the same site), and the hopping energy and nearest neighbour p-wave interaction to be the same, or equivalently the interaction of the neighbouring sites Majoranas be the same. However, this is just a mathematical exercise. In this limit Equation 4 reduces to

$$\begin{aligned}
\hat{H} &= -\tfrac{1}{2}\Delta \sum_{i=1}^{n-1} \left[c_i^\dagger c_{i+1} + c_{i+1}^\dagger c_i - c_i c_{i+1} - c_{i+1}^\dagger c_i^\dagger \right] \\
&= -\tfrac{1}{2}\Delta \sum_{i=1}^{n-1} \left[-c_{i+1} c_i^\dagger + c_{i+1}^\dagger c_i + c_{i+1} c_i - c_{i+1}^\dagger c_i^\dagger \right] \\
&= -\tfrac{1}{2}\Delta \sum_{i=1}^{n-1} \left[\left(c_{i+1}^\dagger + c_{i+1} \right) \left(c_i - c_i^\dagger \right) \right].
\end{aligned} \tag{5}$$

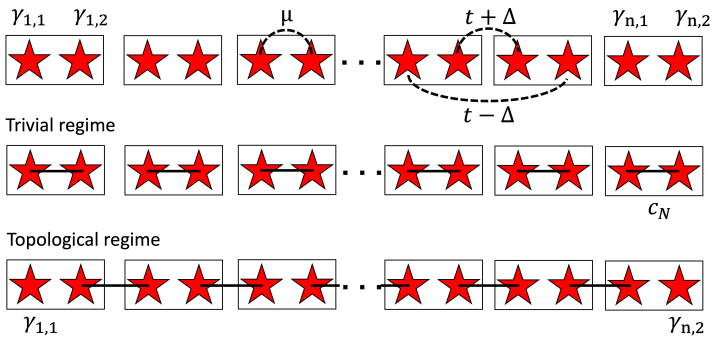

Figure 2.1: (Top) Kitaev model with spinless electrons (black box) on cite i rewritten in terms of a pair of Majorana operators (red stars). The chemical potential, μ, pairs Majorana operators that belong to the same electron, hopping, t, and pair tunneling, Δ, pair Majorana operators belonging to adjacent electrons. (middle) The Kitaev model in the trivial regime limit with all Majoranas paired. (bottom) The model in the topological phase with two unpaired Majorana operators which describe the MZMs at the ends of the system.

The last line can now be rewritten using the Majorana operators definition in terms of c and $c^\dagger$, given in Eq.3, to arrive at

$$\hat{H} = \frac{i\Delta}{2} \sum_{i=1}^{n-1} \gamma_{i+1,1}\gamma_{i,2}. \tag{6}$$

This can now be diagonalized using the following transformation of basis, $b_i = \frac{1}{2}\left(\gamma_{i+1,1} + i\gamma_{i,2}\right)$ and $b_i^\dagger = \frac{1}{2}\left(\gamma_{i+1,1} - i\gamma_{i,2}\right)$. These new operators represent Dirac fermions that are composed of Majoranas from neighboring sites, demonstrated by the solid lines connecting Majoranas in Figure 2.1. In this basis the Hamiltonian is now

$$\hat{H} = \Delta \sum_{i+1}^{n-1} b_i^\dagger b_i, \tag{7}$$

which show that the eigen basis for the Kitaev model in this limit is the number of spinless fermions that exist across the segments that we have defined. Now, this is where Kitaev's insight becomes apparent. With this setup two Majorana states do not appear in this Hamiltonian, $\gamma_{1,1}$ and $\gamma_{n,2}$, i.e. the two Majorana states at the ends of the chain, shown in 2.1 (bottom).

These Majorana states describe a non-local fermion, given by

$$b_M = \tfrac{1}{2}\left(\gamma_{1,1} + i\gamma_{N,2}\right)$$
$$b_M^\dagger = \tfrac{1}{2}\left(\gamma_{1,1} - i\gamma_{N,2}\right). \tag{8}$$

Additionally, with this fermionic state not appearing in the Hamiltonian, it can be created or destroyed at 0 energy. I.e. it doesn't add or remove energy to have these in the system. In this setup these two Majorana modes have been separated, but are correlated by describing one fermionic state. If we are able to spatially control these Majoranas separately, it is possible to think about moving them around each other. This procedure is known as braiding and is how quantum computers would use MZMs to perform gate operations on the MZM qubits . These Majorana zero modes don't only appear in the limit of $t = \Delta$ and $\mu = 0$, but under the condition

$$|\mu| < t, \tag{9}$$

defined as the topological regime. Within this the unpaired Majorana fermions are left at the ends of the 1D chain. Outside this is the trivial regime, shown in the middle panel in 2.1 with all the Majoranas paired up on the same site.

A way to visualize MZMs is to diagonalize the Kitaev chain model hamiltonian. If this is done for some finite n-site system, the eigenvector with eigen value 0 (or closest to in a finite system) is the MZM, and this eigenvector appears as a state localized at the ends of the 1D system. This is shown in 2.2, done in the Majorana basis, i.e. shown as γ_1 and γ_2 to emphasize that it is two separate Majoranas that are localized at the ends of the chain which belong to one Dirac fermion state. In addition to the Kitaev model there are other systems, such as in 2D, where the MZMs appear. In 2D systems the MZMs appear in a different manner, as vortices on the surface. This work will focus on the 1D chain model for MZMs.

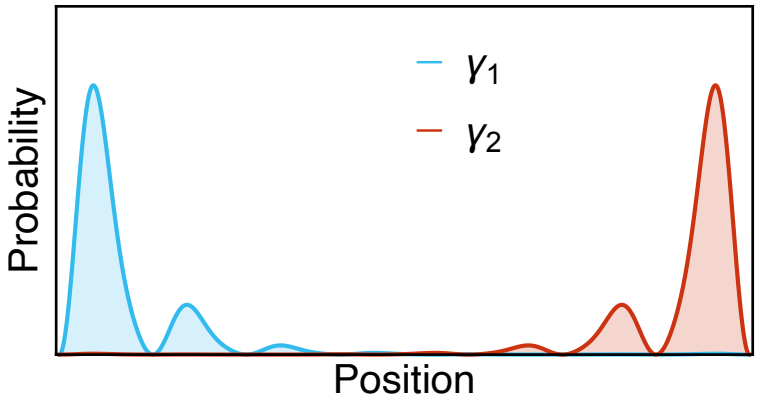

Figure 2.2: The positional dependence of the closest to 0-energy eigenvector in a Kitaev chain model for a finite system. This has been split into the Majorana basis.

2.2.1 Majoranas for quantum computation

With the knowledge of what Majorana zero modes are in condensed matter systems, we can now briefly discuss why there is interest in topological qubits and why MZMs can be used for them [21]. One of the current complications with building quantum computers is that small energy fluctuations can change the state being used for the qubit, introducing errors. For example, if the spin of an electron is used to encode the information the spin could randomly flip. For MZM, their first benefit is the topological protection offered due to the non-locality of the MZM state. When a Kitaev chain crosses from the topologically trivial state to the topological state, i.e. when the topological condition is met, given in Eq.9, there are two non-local MZMs bound at the end of the 1D chain. The two spatially separated MZMs describe one Dirac fermion, and this state is protected by the superconducting gap. As long as there are no perturbations larger than this, and the system remains in the topological regime, the information stored in the MZM is protected. This means energy fluctuations smaller than the gap cannot decohere the quantum state.

The second benefit of using MZMs is one can use their non-Abalien properties to encode quantum gate operations into a braiding procedure of Majorana zero modes, i.e. moving these states around each other [17]. The non-Abelian nature of MZMs means their commutation

rules are neither those of fermions or bosons, which can be seen in Section 2.1. This is unusual, as often we only deal with the symmetric bosons and anti-symmetric fermions wave function exchange statistics. The exchange relation of a quantum state is an extremely importance principle, at the root of the Pauli principle, superfluidity, the metallic state, Bose-Einstein condensation, and a long list of other phenomena. In the usual 3 spatial and 1 time dimension, (3+1)D, there are actually only these two types of exchange statistics. However, due to the low dimensionality and the indistinguishable degenerate ground states (there are two MZMs at 0 energy) this systems can have non-Abalien properties. Therefore, using a Majorana braid to encode gate operations is a fault tolerant way to perform computations due the topological protection of the MZMs.

However, the 1D p-wave topological superconductors that harbour these states have yet to be realized experimentally. The question is where to look for them, and there have been several experimentally accessible models proposed and investigated over last 15 years. The next section will discuss one of the most prominent experimentally feasible proposals, the hybrid semiconductor-superconductor system.

2.3 Experimental Search

The issue with the Kitaev model is that it uses spinless fermions with a p-wave superconducting interaction. There is not a readily available analogue to this in the real world. Since the advent of the Kitaev model, physicists have searched many places for an experimentally accessible platform that describes, or can effectively describe, a p-wave topological superconductor. Some of the proposed platforms are topological insulators and superconductors, systems that show the fractional quantum hall-effect, magnetic chains on a superconductor, or hybrid devices that couple a strong spin orbit coupled semiconductor nanowire to a conventional superconductor [20]. The proposal that this work will focus on is the last one, with this platform gaining a huge amount of attention over the last 10 years.

2.3.1 Majorana nanowire mode

One of the most promising platforms to find an effective Kitaev chain model with MZMs is in semiconductor-nanowire, superconductor hybrid systems. This candidate system was first proposed in the works of [18, 19]. These hybrid systems utilize the nanowire's inherently strong spin-orbit coupling; proximity-induced s-wave superconductivity via contact with conventional superconductors; and an external magnetic field to act as effective p-wave superconductors. We will discuss how this systems achieves this.

To realize MZMs in the hybrid setup one needs to engineer the single spin superconductivity, which wasn't an issue with the Kitaev model as spin was ignored. The superconductivity in conventional superconductors is spin-singlet, i.e. the two electrons are paired with opposite spins. Therefore the required setup has a single band with different spin directions for positive k and for negative k which will realize the single particle superconducting states needed for MZMs. The first step is lifting the spin degeneracy of states in a s-wave superconductor, the spin degeneracy means one cannot isolate a single electron. This arises due to the symmetry of the pairing potential Δ, i.e $\Delta(k) = \Delta(-k)$. However, in the Kitaev model the p-wave pairing potential phase is k-dependent and therefore breaks time reversal symmetry, lifting the spin degeneracy. The s-wave degeneracy can be lifted by applying a magnetic field, shown in Figure 2.3 in panels (a) to (b). However, with a strong enough magnetic field the superconductivity is destroyed, so the field can not be made arbitrarily large.

The next step is that a conventional superconductor couples a spin up Dirac fermion at positive k with spin down one at negative k. To that end, the s-wave superconductor can be brought in proximity with a semiconductor which has a large spin orbit interaction. The spin orbit interaction bands are split such that, for example, one has spin left for positive k and spin right for negative k, while the other band has the opposite. This is shown in Figure 2.3 in panel (c), however this is a cartoon picture as spin is undefined in this system. With only spin orbit coupling the problem is that there is still a degeneracy point at k=0 where the bands cross. Combining this with a magnetic field can lift this, but there is not complete opposite spin for positive and negative k but some opposite component to the spins such

that the superconductivity can be induced in the semiconductor nanowire.

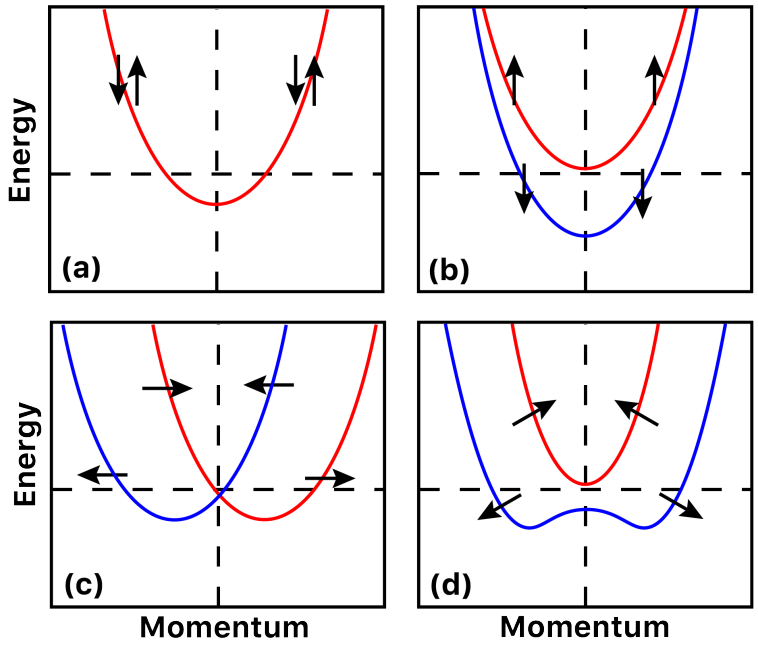

Figure 2.3: Spin orientation of a conduction band for a semiconductor-superconductor hybird model. (a) without spin orbit coupling or magnetic field. (b) with magnetic field only. (c) with spin orbit coupling only. (d) with spin orbit coupling and magnetic field.

With all these ingredients the model Hamiltonian for this system can be written down. The 1D semiconductor nanowire-superconductor model Hamiltonian is:

$$\begin{aligned}\hat{H}_{NW} = & \left(\tfrac{p^2}{2m^*} - \mu + \alpha_R \left(\boldsymbol{\sigma} \times \mathbf{p}\right) \cdot \hat{\mathbf{z}}\right) \tau_z \\ & + V_z \left(\cos\theta\sigma_x + \sin\theta\sigma_y\right) + \Delta_s \tau_x \sigma_y\end{aligned} \tag{10}$$

which acts on the Nambu spinor basis $\hat{\psi}_x = \left(c_{\uparrow x}, c_{\downarrow x}, c^\dagger_{\uparrow x}, -c^\dagger_{\downarrow x}\right)^T$. The momentum $\mathbf{p}$ points in the direction of a section of semiconductor-nanowire, Δ_s is the s-wave superconducting pairing term, $V_z = \frac{1}{2} g_{eff} \mu_B B$ is the Zeeman energy with B the magnetic field, θ is the angle of the field relative to the positive x-axis, τ and σ are Pauli matrices representing the particle-hole and spin spaces respectively, and α_R is the Rashba spin orbit coupling term. The SOC term has $\cdot\hat{\mathbf{z}}$ as this is the direction of the internal electric field which induces the Rashba SOC, the direction arises because of the crystal asymmetry from the nanowire growing on

the substrate, and the nanowire coating can affect this as well [25] These parameters are taken constant because the nanowire is considered to be made of a homogeneous material.

For an infinite system to be in the topological phase the following condition must be met

$$V_z > \sqrt{\mu^2 + \Delta_s^2} \tag{11}$$

When this system is deep in the topological phase it is known that this reduces to a p-wave topological system described by Eq.(4). To simulate the model in a finite one-dimensional system the continuum model is discretized on a 1D lattice in the electronic state basis, shown in Eq. (29).

2.3.2 Magnetic field

We make special note of a the effect and application of the magnetic field in this model, as this is the topic of the project discussed in 5. Too high a magnetic field destroys superconductivity as this disrupts the paired electrons in the Cooper pairs. This is because they have opposite spin and momentum at any moment in time, and, the applied magnetic field exerts a force that tries to unbalance the electrons momentum, aligning both spins with the field direction. However, it takes a certain amount of energy to disrupt the Cooper pairs, so a superconductor can tolerate magnetism up to a point before reverting to a normally conducting state. Additionally, the effect of the magnetic field on the hybrid model is direction dependent. Often it is assumed that the applied magnetic field is uniform, where in experimental setups this field is applied from large external magnet. However, one can envisage the external field being applied by micro to nano-scale magnets, who's stray field changes on the scale of the hybrid nanowire system. The local control over the field magnitude and direction offered by this is advantageous, particularly for 2D geometries where it may be required to position some of the wires at an angle with other wires, such as in junction set-ups appropriate for braiding. Achieving local field control in braiding, or even simple set-ups, could offer novel ways to control Majorana-based devices.

3.0 Density Functional Theory

3.1 Introduction

Density Functional Theory (DFT) is an approximate numerical method to solve the electronic structure of problems of condensed phases in physics, chemistry, and materials science. It is an Ab initio, first principles method, meaning this is done without empirical parameters. It is a theory of of interacting, correlated, many-body systems of electrons. Using it we can investigate a variety of different systems, such as bulk materials or surfaces, or finite setups such as interfaces or nanoclusters, and then obtain properties such as the band structure, density of states, electronic density, forces and adhesion energy, among many others, principally at the ground state at 0K. DFT operates via the Kohn–Sham equation an the use of functionals that describe the spatially dependent electron density, and, through self-consistent minimization of the energy of the system, can access all these system properties through the Hohenberg and Kohn theorem.

3.1.1 Motivations

The non-relativistic many-body Schrödinger equation is an eigenvalue problem as defined below:

$$\hat{H}\Psi = E\Psi. \tag{12}$$

$\hat{H}$ is the many-body Hamiltonian operator, E represents the energy, and Ψ is the many-body wave function. This wave function will provide all the information on the systems, such as how the electrons behave. The wave function is extremely complicated with a dimensionality equal to 3N, where N is the amount of electrons in the system, and the Hilbert space grows exponentially with the number of electrons.

We can write the exact form of the Hamiltonian for the system of interest (e.g. atom, crystal structure), [26]

$$\hat{H} = -\frac{\hbar^2}{2m_e}\sum_i \nabla_i^2 - \sum_I \frac{\hbar^2}{2M_I}\nabla_I^2 + \frac{1}{2}\sum_{i\neq j}\frac{e^2}{|r_i - r_j|} + \frac{1}{2}\sum_{I\neq J}\frac{Z_I Z_J e^2}{|R_I - R_J|} - \sum_{i,I}\frac{Z_I e^2}{|r_i - R_I|}. \tag{13}$$

Where $\hbar$ is the normalized Planck constant, m_e and M_I are the mass of an electron and nuclei, e is the charge of an electron, and Z is the atomic number of a nuclei. The first term in Equation (13) represents the kinetic energy of the electrons, the second term represents the kinetic energy of the nuclei, the third and fourth terms represent the electron-electron and nuclei-nuclei coulomb interactions, and the final term represents the electron-nuclei coulomb interactions. This is clearly a many-body, complicated operator which depends on several interacting terms. However, the approximation by Born and Oppenheimer was used to simplify the picture [27]. By using the fact that the mass of a proton/neutron is 1700 times larger than the mass of an electron, they concluded that the motion of the nucleus relative to the electrons is negligible, therefore accurate results can be obtained even if the nuclei are considered to be stationary objects. Such a simplification allows for the removal of two terms from the Hamiltonian, namely, the kinetic energy of the nuclei and the nuclei-nuclei coulomb interaction, which go to zero and become an additive constant. The Hamiltonian is now described only by the electrons and how they interact with each other and their stationary environment:[26]

$$\hat{H} = \hat{T} + \hat{V}_{\text{int}} + \hat{V}_{\text{ext}} + E_{\text{II}} \tag{14}$$

Where $\hat{T}$ represents the kinetic energy operator for the electrons, $\hat{V}_{\text{int}}$ is the electron-electron interaction, $\hat{V}_{\text{ext}}$ is the external potential of the nuclei acting on the electrons, and E_{II} is the constant energy contribution of the nuclei-nuclei interaction and will be ignored from now on for the sake of simplicity. Using this simplified Hamiltonian the Schrödinger equation can still only be solved for trivial systems due to the strongly correlations of the electrons, and therefore the solution is non-separable and scales exponentially as more electrons are added to the system. This challenge is what motivated physicists to look past the many-body wave function towards simpler, more attainable solutions.

3.1.2 The Electron Density

To deal with the exponential increase in calculation with the number of electrons, using the electron density was investigated as a possible solution. Electronic density, $n(\mathbf{r})$, just gives the charge distribution in space, and it therefore only has dimensionality 3 (x,y,z).

In the 1920's Thomas and Fermi proposed their approach to write the total energy as a functional of the electron density:[28, 29]

$$E_{\mathrm{TF}}[n] = C_1 \int d^3r\, n(\mathbf{r})^{(5/3)} + \int d^3r\, V_{\mathrm{ext}}(\mathbf{r}) n(\mathbf{r}) + \frac{1}{2} \int d^3r\, d^3r'\, \frac{n(\mathbf{r}) n(\mathbf{r}')}{|\mathbf{r} - \mathbf{r}'|}. \tag{15}$$

Where the first term is the kinetic energy of the electrons (for a non-interacting homogeneous electron gas in the Thomas Fermi approximation), the second term is the external potential, and the third term is the classical electrostatic Hartree potential, all as functionals of the electron density, where the electron density is given as:

$$n(\mathbf{r}) = \langle \Psi | \hat{n}(\mathbf{r}) | \Psi \rangle = N \int dr_2\, dr_3\, \ldots\, dr_N |\Psi(\mathbf{r}, \mathbf{r}_2, \ldots, \mathbf{r}_N)|^2. \tag{16}$$

This functional failed to produce accurate results due to the oversimplified kinetic energy term and the lack of electron-electron interactions. However, this was an important first step in showing that the electron density was a useful variable. Then, in 1964, the unique relationship between the electron density and the wave function was shown in the seminal paper of Hohenberg and Kohn [30]. This paper laid the foundations for DFT by detailing two proofs which showed that:

1. There is a unique 1:1 mapping between the external potential of a system and it's electron density.
2. If a universal functional for the kinetic energy and electron-electron interactions can be defined in terms of the electron density, then such a functional can be minimized to find the exact ground state energy and electron density for any given external potential.

This exact functional can be written as:

$$E_{\mathrm{HK}}[n] = F_{HK}[n] + \int d^3r\, V_{\mathrm{ext}}(\mathbf{r}) n(\mathbf{r}) = F_{HK}[n] + V_{\mathrm{ext}}[n] \tag{17}$$

Where $F_{\mathrm{HK}}[n]$ is the universal functional, which can be defined as the the summation of the exact kinetic energy functional, $T[n]$, and the exact electron-electron interaction, $E_{\mathrm{int}}[n]$. The second term is the density functional of the external potential, which is the same as defined above in Equation (15). Unfortunately, the theorem provides no information on what is or how to obtain the universal functional, and would require a search of all possible densities and all possible external potentials in order for it to be determined. Therefore, more simplifications must be made in order for this new knowledge to be put into practice.

3.1.3 Kohn-Sham Auxiliary System

An auxiliary system can be thought of as a simplified and more easily solvable system that has the same desired properties as the real system (e.g. ground state electron density) while neglecting the properties that are not of interest (e.g. excited states). To build such a system, Kohn and Sham asked if an auxiliary system on non-interacting electrons could arrive at the same ground state electron density as a system of interacting electrons [31]. One of the most important realizations of the Kohn-Sham auxiliary system was the development of the exchange correlation functional, which can be derived by adding and subtracting the single particle kinetic energy functional ($T_s[n]$) and the classical electrostatic Hartree potential ($E_{\text{Hartree}}[n]$) to the exact functional (E_{HK}):

$$E_{\text{HK}}[n] = F_{HK}[n] + V_{\text{ext}}[n] + T_s[n] - T_s[n] + E_{\text{Hartree}}[n] - E_{\text{Hartree}}[n] \tag{18}$$

By rearranging the above equation, the Hohenberg-Kohn functional can be separated into it's known an unknown terms:

$$E_{\text{HK}}[n] = (T_s[n] + V_{\text{ext}}[n] + E_{\text{Hartree}}[n]) + (F_{HK}[n] - T_s[n] - E_{\text{Hartree}}[n]) \tag{19}$$

The unknown terms can now be grouped into a new term called the exchange correlation functional, $E_{\text{xc}}[n]$. By further breaking down the universal functional, F_{HK}, into it's individual components, it can be seen that the exchange correlation functional is just the summation of the difference between the true and single particle kinetic energies and the true electron-electron interaction and the Hartree energy.

$$E_{\text{xc}}[n] = F_{HK}[n] - T_s[n] - E_{\text{Hartree}}[n] = (T[n] - T_s[n]) + (E_{\text{int}}[n] - E_{\text{Hartree}}[n]) \tag{20}$$

The exact functional can now be expressed in terms of the known single particle equations, also called the Hartree equations, and the exchange-correlation term to account for the difference between the true interacting system and the auxiliary non-interacting system.

$$E_{\text{HK}}[n] = T_s[n] + V_{\text{ext}}[n] + E_{\text{Hartree}}[n] + E_{\text{xc}}[n]. \tag{21}$$

Minimizing this energy functional under the constraint of ortho-normalized wave functions, gives the seminal Kohn-Sham equation [31]. Such an equation can then be solved self-consistently to arrive at the ground state electron density of the system by summing the square moduli of the single particle wave functions [31].

$$\left[-\frac{\hbar^2}{2m^e}\nabla^2 + V_{\text{ext}}(r) + V_{\text{Hartree}}([n], r) + V_{\text{xc}}([n], r)\right]\psi_i(r) = \epsilon_i\psi_i(r) \quad n(r) = \sum_i |\psi_i(r)|^2 \quad (22)$$

If the exact exchange-correlation functional was known, these equations would lead to the exact ground state electron density. However, the exact exchange-correlation is not known, leading to the development of a variety of approximations for this term, such as the local density approximation[31] (LDA) and the generalized gradient approximation (GGA) [32, 33, 34, 35]. LDA was introduced along with the Kohn-Sham equations by assuming that the exchange-correlation functional could be approximated by using the exact exchange-correlation of a uniform electron gas with the same density as the local region [31]. GGA functionals improved upon this by adding in the local gradient of the electron density in order to more accurately depict the non-uniformity of the electron density [32, 33, 34, 35]. In current practice, the GGA functional known as PBE (Perdew, Burke, Ernzerhof) is one of the most commonly used approximations for the exchange-correlation functional [35], due to its effectiveness at describing certain materials and it being relatively computationally inexpensive.

3.1.4 The Band Gap and DFT+U

Despite the success of DFT's over a large range of problems, it has some weaknesses. For example, LDA functionals often underestimate bond lengths, and, of note here, it underestimates band gaps of semiconducting and insulating materials [36, 37, 38, 39, 40, 41, 42, 43, 44]. One reason for this is due to the so called self interaction error (SIE), which arises from the classical Hartree potential (V_{Hartree}) due to an included energy contribution from an electron interacting with itself [36, 37, 38, 39, 40, 41, 42, 43, 44]. The SIE would be cancelled if the exact exchange correlation functional was known, but this is not the case, so other methods have been proposed to reduce the SIE. Hybrid functionals, such as HSE proposed by [45],

partially negate the SIE by using a linear combination of Hartree-Fock and GGA exchange. The Hartree-Fock is included only for the short-range part of the electron-electron interaction, significantly reducing the cost of evaluating the non local Hartree-Fock part while providing the desired accuracy [46]. This functional has been known to make very accurate band gap predictions for inorganic crystals, especially those with smaller band gaps [47]. The main limitation of hybrid functionals is they are computationally expensive, due to the calculation of the Hartree-Fock exchange, ultimately limiting it's applications to smaller systems.

An alternative approach, known as DFT+U attempts to correct the SIE error by applying a Hubbard-U correction to specific orbitals [48, 49]. The motivation for this correction stems from the fact that the SIE is essentially an electron-electron repulsion term, meaning that it tends to over-delocalize states [50, 51]. To correct for this, states that should be localized, such as d orbitals in transition metals, can be modeled by the Hubbard model, while the rest of the states can be described by a standard exchange-correlation functional. Any orbital that receives a positive U value is then further localized by increasing the intraband repulsive Coulomb interaction. Since the Hubbard model is effective at describing localized states, it can be efficiently used to correct for the SIE using the following expression:

$$E_{DFT+U} = E_{DFT} + \frac{U - J}{2} \sum_{\sigma} n_{m,\sigma} - n_{m,\sigma}^2 \tag{23}$$

where n is the atomic-orbital occupation number, m is the orbital momentum, σ is a spin index, U represents the on-site Coulomb repulsion, and J represents the exchange interaction. A popular implementation of DFT+U by Dudarev *et. al.* [49] uses a single effective U-parameter, $U_{eff} = U - J$, for each element in a given system and can be determined using various first-principles approaches. One such approach is the linear response method proposed by Cococcioni and de Gironcoli [52]. Due to this method requiring an increasing in size supercell to converge the U value, this can result in a significant computational cost. To combat the computationally expensive nature of the first-principles method, Yu *et. al* [53] proposed a method known as DFT+U(BO) to empirically fit the effective U-values using Bayesian optimization (BO) to match the band structure and band gap of a more accurate DFT functional, such as a hybrid functional or higher level theory such as GW.

DFT+U(BO) has been demonstrated to achieve comparable accuracy to a hybrid functional at the computational cost of a semi-local functional for transition metal monoxides, europium chalcogenides, and narrow-gap semiconductors. It has enabled conducting unprecedented simulations of large surface and interface models, involving materials such as InAs, InSb, α-Sn, CdTe, ZnTe, and CdSe which are not properly described by semi-local functionals [54, 55, 56].

BO [57] is a global optimization algorithm that can optimize unknown functions by performing iterative updates to an initial assumption (prior) of the function's form by strategically sampling points within the search space. A common statistical model used for the BO prior is a Gaussian process [58] because it allows for quantifying the uncertainty with each prediction. To intelligently select the next point to sample, BO utilizes an acquisition function [59], which helps minimize the amount of objective-function evaluations (in our case, DFT calculations). This is achieved by balancing the exploration of regions of high uncertainty, which have high information content, with the exploitation of the region(s) where the objective function optimum is predicted to be found.

The choice of the objective function being optimized is essential to the success of BO. An objective function was developed, $f(\vec{U})$, whose maximum corresponds to the U_{eff} values that best reproduces the shape of the band structure and band gap, E_{g}, obtained from HSE:

$$f(\vec{U}) = -\alpha_1(\mathrm{E_g^{HSE}} - \mathrm{E_g^{PBE+U}})^2 - \alpha_2(\Delta\mathrm{Band})^2 \tag{24}$$

Here, $\vec{U} = [U^1, U^2,...,U^n]$ is the vector of U_{eff} values applied to different atomic species. ΔBand is defined similarly to Ref. [60] as the mean squared error of the PBE+U band structure with respect to HSE:

$$\Delta\mathrm{Band} = \sqrt{\frac{1}{N_{\mathrm{E}}}\sum_{i=1}^{N_{\mathrm{k}}}\sum_{j=1}^{N_{\mathrm{b}}}(\epsilon^j_{\mathrm{HSE}}[k_i] - \epsilon^j_{\mathrm{PBE+U}}[k_i])^2} \tag{25}$$

N_{E} is the total number of eigenvalues, ϵ is the eigenvalue at a given k-point, N_{k} is the number of k-points, and N_{b} is the number of bands. To make ΔBand independent of the band gap, the conduction band minimum (CBM) and valence band maximum (VBM) are shifted to zero for both the HSE and PBE+U calculations, ensuring that ΔBand is only

comparing qualitative features of the band structures. The coefficients α_1 and α_2 may be used to weight the importance of the band gap vs. the band structure, and in cases where there is no band gap (e.g. α-Sn,) α_1 is set to 0. Additionally, it is possible to control a trade-off between exploration and exploitation via the κ, not given in this equation. With a larger value of κ, the algorithm favors more exploration of points where the variance is large, as opposed to exploitation of points that are predicted to be close to the optimum. A DFT calculation is performed in each iteration to evaluate $f(\vec{U_n})$. The function estimate (posterior) is updated and the acquisition function is re-calculated after each iteration until the maximum number of iterations, N, is reached. The code [53] then outputs the U_{eff} value, $\vec{U}$, that maximizes $f(\vec{U})$. The total computational cost of this method [53] is relatively low because all calculations are for a primitive bulk unit cell and thus have a minimal number of atoms. The HSE calculation is only performed once and the PBE+U calculations are inexpensive. The number of iterations to convergence is typically low, under 100, thanks to the efficiency of BO.

We note that we have chosen to use the PBE and HSE functionals, however the method may be applied in a similar manner using any local or semi-local functional for DFT+U and any hybrid functional or GW as the reference method.

3.1.5 VASP

The chosen software to perform DFT calculations in this project is the Vienna Ab Initio Simulation Package (VASP) [61]. This software encompasses the standard selection of DFT techniques and functional implementations, with the functionals such as LDA, GGAs, metaGGAs, Hybrid functionals and Green's functions methods all available. In VASP, central quantities, like the one-electron orbitals, the electronic charge density, and the local potential are expressed in plane wave basis sets. The interactions between the electrons and ions are described using norm-conserving or ultrasoft pseudopotentials, or the projector-augmented-wave (PAW) method. The fundamental mathematical problem that VASP solves is a non-linear eigenvalue problem, which is solved iteratively via self-consistent cycles until the desired accuracy is achieved. To determine the electronic groundstate, VASP makes use

of efficient iterative matrix diagonalisation techniques.

4.0 First Principles Assessment of CdTe as a Tunnel Barrier at the α-Sn/InSb Interface

4.1 Introduction

The first project to consider is that of simulating a tri-layer system with CdTe as a Tunnel Barrier at the α-Sn/InSb interface, within DFT. This is motivated by the promising route toward the realization of fault-tolerant quantum computing schemes is developing materials systems that can host topologically protected Majorana zero modes (MZMs) [14, 62, 17]. MZMs may appear in one-dimensional topological superconductors [18, 19, 63, 22], which can be effectively realized by proximity coupling a conventional superconductor and a semiconductor nanowire that possesses strong spin-orbit coupling (SOC). Adding in a magnetic field enables this system to behave as an effective spinless p-wave topological superconductor, which allows for MZM states. Recently, there have been new developments in material choices and experimental methods to identify MZMs in semiconductor nanowire-superconductor systems, designed to overcome challenges identified during the first wave of experiments [64, 65, 66]. These include trying new combinations of semiconductors and epitaxial superconductors, e.g. Pb, Sn, Nb, to maximize the electron mobility and utilize larger superconducting gaps and higher critical magnetic fields [67, 68, 69, 70, 71]. Additionally, new proposed architectures include creating nanowire networks and inducing the field via micromagnets [72, 73].

One of the challenges presented by the superconductor/semiconductor nanowire construct, is that excessive coupling between the superconducting metal and semiconductor may "metallize" the semiconductor, thus rendering the topological phase out of reach. Theoretical studies that treated the semiconducting and superconducting properties via the Poisson-Schrödinger equation, have shown that excessive coupling between the materials may lead to the semiconductor's requisite properties, such as the Landeé g-factor and spin-orbit-coupling (SOC), being renormalized to a value closer to the metal's. In addition, large unwanted band shifts may be induced [74, 75, 68, 76, 77, 78, 79, 80, 81]. Having a tunnel

barrier could modulate the superconductor-semiconductor coupling strength and thus the induced proximity effect, which is critical for controlling experiments. It is currently unknown what the required width range of a tunnel barrier is.

InSb and Sn are among the materials used to fabricate devices for Majorana search [82]. InSb is the backbone of such systems because it has the highest electron mobility, strongest spin-orbit coupling (SOC) and a large Landé g-factor in the conduction band compared to other III-V semiconductors. $\beta-$Sn has a bulk critical field of 30 mT and a superconducting critical temperature of 3.7 K, higher than the 10 mT and 1 K, respectively, of Al. Recently, β-Sn shells have been grown on InSb nanowires, inducing a hard superconducting gap [68]. The large band gap semiconductor CdTe is a promising candidate to serve as a tunnel barrier. Thanks to its relative inertness, it may simultaneously act as a passivation layer protecting the InSb from environmental effects and potentially minimizing disorder [83, 84]. Advantageously, CdTe is lattice matched to InSb [85]. Sn has two allotropes. The β form, with a BCT crystal structure, is of direct relevance to MZM experiments thanks to its superconducting properties. However, the semi-metallic α form has a diamond structure, which is lattice matched to InSb and CdTe, making it an ideal model system for investigating, both theoretically and experimentally, the electronic structure of Sn/InSb heterostructures.

Much experimental work, such as growth and angle-resolved photoemission spectroscopy (ARPES) studies, has been undertaken on α-Sn. Previously, α-Sn has been found to possess a topologically trivial band inversion, with SOC inducing a second band inversion and a topological surface state (TSS) [86, 87]. The effect of strain on the topological properties of α-Sn has also been studied [88, 89, 76, 90, 91, 92, 93, 94, 95, 96, 97]. In-plane compressive strain has been reported to make α-Sn a topological Dirac-semi-metal and induce a second TSS to appear [86]. Conversely, tensile strain has been reported to induce a transition to a topological insulator. CdTe [84] and α-Sn [68, 87] have been epitaxially grown on InSb. Depositing Sn on InSb often leads to growth of epitaxially matched α-Sn, although β-Sn may appear under some conditions [98]. In addition, α-Sn can transition to β-Sn if the Sn layer is above a critical thickness or if heat is applied during fabrication processes [99, 100]. Studying the interface with the lattice matched α-Sn may provide insight, which is also pertinent to β-Sn as both could be present in hybrid systems. Therefore, these are promising materials

to investigate for future device construction.

MZM experiments rely on finely tuned proximity coupling between a superconducting metal and a semiconductor. By adding a tunnel barrier at the interface between the two materials and varying its width, one could potentially modulate the proximity coupling strength to achieve precise control over the interface transparency. To the best of our knowledge, this idea has not yet been tested in experiments and it is presently unknown which material(s) would be the best choice for a barrier and what would be the optimal thickness. Simulations of a tri-layer system with a tunnel barrier are therefore needed to inform MZM experiments. Here, we use density functional theory (DFT) to study a tri-layer system, in which InSb is separated from α-Sn by a CdTe tunnel barrier. Despite recent progress towards treating superconductivity within the framework of DFT [101, 102] the description of proximity-induced superconductivity at an interface with a semiconductor is still outside the reach of present-day methods. However, DFT can provide useful information on properties, such as the band alignment at the interface. Conduction band offsets are of particular importance because the proximity effect in most experiments on InSb primarily concerns the conduction band. In addition, DFT can provide information on the penetration depth of metal induced gap states (MIGS) into the semiconductor. [84, 103, 75, 104]

Within DFT, computationally efficient (semi-)local exchange-correlation functionals severely underestimate the band gap of semiconductors to the extent that some narrow-gap semiconductors, such as InSb, are erroneously predicted to be metallic [105]. This is attributed to the self-interaction error (SIE), a spurious repulsion of an electron from its own charge density [106]. Hybrid functionals, which include a fraction of exact (Fock) exchange, mitigate the SIE and yield band gaps in better agreement with experiment. However, their computational cost is too high for simulations of large interface systems, such as the α-Sn/CdTe/InSb tri-layer system studied here. The DFT+U approach, whereby a Hubbard U correction is added to certain atomic orbitals, provides a good balance between accuracy and computational cost[105, 46]. Recently, some of us have proposed a method of machine learning the U parameter for a given material by Bayesian optimization (BO) [107]. The DFT+U(BO) method has been employed successfully for InSb and CdTe [108].

It has been shown that (semi-)local functionals fail to describe the bulk band structure

of α-Sn correctly, specifically the band ordering and the orbital composition of the valence bands at the Γ point. DFT+U, hybrid functionals, or many-body perturbation theory within the GW approximation are necessary to obtain a correct description of the band structure [109, 110, 94, 88, 111]. DFT+U simulations have required slab models of more than 30 monolayers of Sn to converge towards a bulk regime, where quantum confinement is no longer dominant. Quantum confinement is the change of electronic and optical properties when the system is of sufficiently small size, typically 10 nanometers or less. The band gap increases as the size of the nanostructure decreases. With a small number of layers α-Sn may exhibit topological properties [112, 85, 113]. Some DFT studies have considered slab models of bi-axially strained α-Sn. DFT simulations of strained α-Sn on InSb have been conducted with a small number of layers of both materials [114, 85]. The DFT+U approach has reproduced the effects of strain and compared well with experimental data [87, 112, 114].

Here, we perform first principles calculations using DFT+U(BO) for a (110) tri-layer semiconductor/tunnel barrier/metal interface composed of the materials InSb/CdTe/α-Sn, owing to their relevance to current Majorana search experiments [84, 68]. To date, DFT studies of large interface slab models with a vacuum region have not been conducted for these interfaces. Previously, the results of DFT+U(BO) for InSb(110) have been shown to be in good agreement with angle-resolved photoemission spectroscopy (ARPES) experiments [115]. Here, we also compare the results of DFT+U(BO) to ARPES for α-Sn (Section 4.3.1) and CdTe (Section 4.3.2). Excellent agreement with experiment is obtained. In particular, for CdTe the z-unfolding scheme (Section 4.2.1) helps resolve the contributions of different k_z values and modelling the 2×2 surface reconstruction reproduces the spectral signatures of surface states. We then proceed to study the bi-layer interfaces of InSb/CdTe, CdTe/α-Sn, and InSb/α-Sn (Section 4.3.3). Finally, to assess the effectiveness of the tunnel barrier, we study tri-layer interfaces with 2 to 16 monolayers (0.5 nm to 3.5 nm) of CdTe inserted between the InSb substrate and the α-Sn (Section 4.3.4). This thickness is within the thickness range of CdTe shells grown on InSb nanowires. For all interfaces, our simulations provide information on the band alignment and the presence of MIGS. See Sec.4.5.3 for more details on MIGS.

We find that 16 layers of CdTe (about 3.5 nm) form an effective tunnel barrier, insulating

the InSb from the α-Sn. However, this may be detrimental for transport at the interface. Based on this, we estimate that the relevant thickness regime for tuning the coupling between InSb and Sn may be in the range of 6-10 layers of CdTe.

4.2 Methods

4.2.1 Band Unfolding

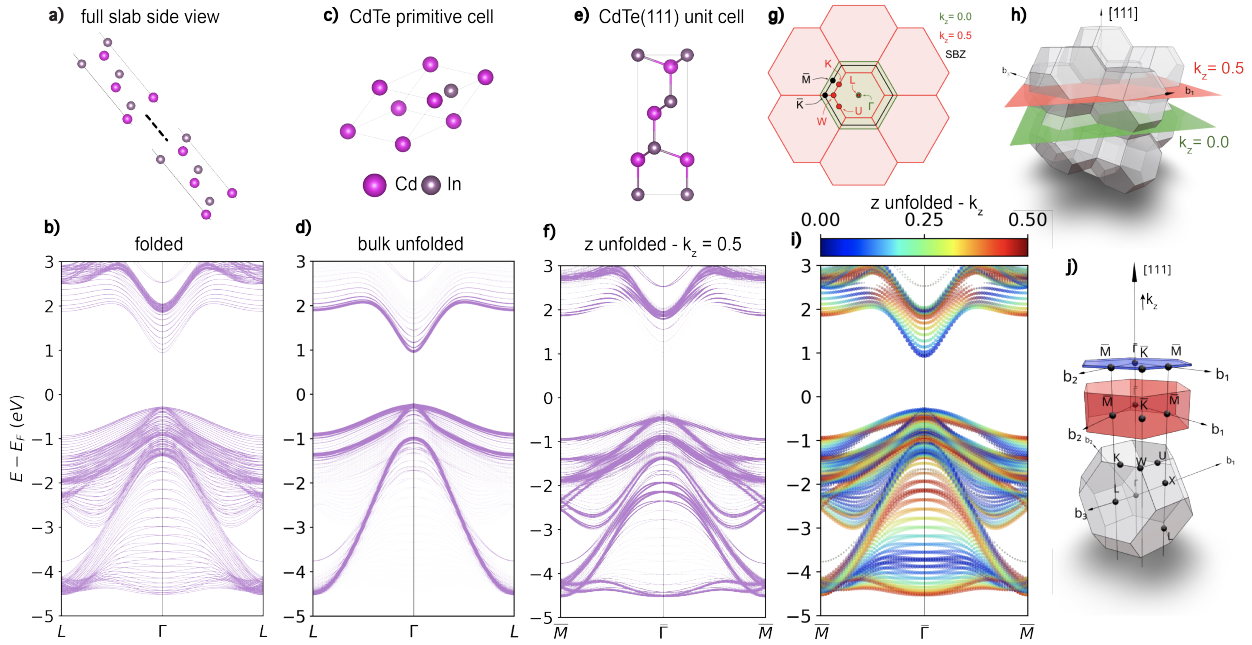

Figure 4.1: (a) Side view of the CdTe(111) slab (b) Folded band structure of CdTe(111) 25 monolayer slab. (c) Primitive unit cell of CdTe (d) bulk-unfolded band structure (e) unit cell of CdTe(111) slab used in z-unfolding. (f) Z-unfolded band structure along k-path $\overline{M}-\overline{\Gamma}-\overline{M}$ for $k_z = 0.5$, and (g) as a function of k_z. (h) FCC bulk BZ (grey), (111) unit-cell BZ (red) and (111) surface BZ (blue). (i) Intersecting planes slice through the bulk BZ for $k_z = 0$ (green) and $k_z = 0.5$ (red) with the SBZ indicated. (j) tessellated bulk BZs showing (111) orientated intersecting planes for given k_z values. Figure taken from [1]

Simulations of large supercell models produce complex band structures with a large

number of bands, as shown in Figure 4.1a,b for a CdTe(111) slab with 25 atomic layers, whose band structure was calculated using PBE+U(BO), as described in the Supporting Information (SI). Band structure unfolding is a method of projecting the band structure of a supercell model onto the appropriate smaller cell ([116, 115]. This can help resolve the contributions of states emerging from of *e.g.,* defects and surface reconstructions vs. the bulk bands of the material. In addition, it can facilitate the comparison to angle-resolved photoemission spectroscopy (ARPES) experiments.

The "bulk band unfolding" scheme [115] projects the supercell band structure onto the primitive unit cell, illustrated in Figure 4.1c. The resulting band structure, shown in Figure 4.1d, appears bulk-like. Bulk-unfolded band structures have been shown to compare well with ARPES experiments using high photon energies, which are not surface sensitive owing to the large penetration depth.

The "z-unfolding" scheme [115] projects the band structure of a slab model with a finite thickness onto the Brillouin zone (BZ) of a single layer of the slab supercell with the same orientation, illustrated in Figure 4.1e. The resulting band structure, shown in Figure 4.1f, contains extra bands that are not present in the bulk-unfolded band structure. The extra bands originate from different k_z values in the 3D primitive Brillouin zone projecting onto the surface Brillouin zone (SBZ), creating overlapping paths. For example, panel Figure 4.1g shows cross sections through the BZ at values of $k_z = 0$ and $k_z = 0.5$. The bulk-paths of $\Gamma - L$, $\Gamma - K$ and $\Gamma - X$ all overlap with the surface k-path $\overline{\Gamma} - \overline{M}$, possibly with contributions from additional paths, such as $X - U$. The plane cuts at different k_z values are derived from the tessellated bulk BZ structure, shown in Figure 4.1h. When z-unfolding is performed, the value of k_z may be treated as a free parameter. The dependence on k_z manifests as a smooth change in the spectral function over the possible range of k_z which varies the mixture of different constituent bulk-paths that overlap the SBZ-path, as shown in Figure 4.1i for $\overline{\Gamma} - \overline{M}$. The BZ for z-unfolding is a surface BZ with a finite thickness, shown in red in Figure 4.1j. The simulation cell for the DFT calculations is set up to be the corresponding real-space unit cell. The z-unfolded k-paths are parallel to the (111) surface at a constant value of k_z.

In ARPES experiments, the relation of the experimental spectra to k_z may be less

straightforward. First, the dependence of the inelastic mean free path of the electrons on their kinetic energy is given by the universal curve [117, 118]. Using photon energies that correspond to a small mean free path is advantageous for probing surface states. However, it can produce prominent k_z broadening due to the Heisenberg uncertainty principle [119, 120, 121, 122] that implies integration of the ARPES signal over k_z through the broadening interval. Second, deviations of the photoemission final states from the free electron approximation can cause contributions from different values of k_z to appear in the ARPES spectra. The photoelectrons are often treated as free electrons, based on the assumption that the photoelectron kinetic energy is much larger than the modulations of the crystal potential. In this case, k_z for a given photoelectron kinetic energy, E_k, and the in-plane momentum, $\mathbf{K}_{//}$, is one single value, which is determined by:

$$k_z = \frac{\sqrt{2m_0}}{\hbar}\sqrt{E_k - \frac{\hbar^2}{2m_0}K_{//}^2 - V_0} \tag{26}$$

where m_0 is the free-electron mass and V_0 the inner potential in the crystal. However, a considerable body of evidence has accumulated that the final states even in metals [123, 124] and to a greater extent in complex materials such as transition metal dichalcogenides [125, 126] can significantly deviate from the free electron approximation. Such deviations can appear, first, as non-parabolic dispersions of the final states and, second, as their multiband composition. The latter means that for given E_k and $\mathbf{K}_{//}$ the final-state wavefunction Φ_f incorporates a few Bloch waves ϕ_{k_z} with different k_z values, $\Phi_f = \sum_{k_z} A_{k_z}\phi_{k_z}$, which give comparable contributions to the total photocurrent determined by the A_{k_z} amplitudes [123]. A detailed theoretical description of the multiband final states, treated as the time-reversed low-energy electron diffraction (LEED) states [120] within the wavefunction matching approach, as well as further examples for various materials can be found in Refs. [125, 126] and the references therein. An insightful analysis of the multiband final states extending into the soft-X-ray photon energies can be found in Ref. [124]. A rigorous analysis of final state effects in ARPES is beyond the scope of this work. Here, we will only mention that all these effects trace back to hybridization of free-electron plane waves through the higher Fourier components of the crystal potential. In cases where significant k_z broadening and/or final states effects are present, z-unfolding, rather than bulk unfolding, should be used in

order to resolve the contributions of different k_z values to the measured spectrum. This is demonstrated for CdTe in Section 4.3.2, where the final states appear to incorporate two Bloch waves with $k_z = 0$ and $k_z = 0.5$.

4.2.2 Interface Model Construction

DFT calculations were conducted with the Vienna Ab Initio Simulation Package (VASP) [61] using the Perdew, Burke, and Ernzerhof (PBE) [127, 128] functional with Hubbard U corrections, [129] whose values were machine learned using Bayesian optimization (BO) [107]. These calculations necessitated the use of high performance computing resources at the computing cluster at the University of Pittsburgh (CRC) and the cluster at NERSC. Additional computational details are provided in the SI. All interface models were constructed using the experimental InSb lattice constant value of 6.479 Å [130], assuming that the epitaxial films of CdTe and α-Sn would conform to the substrate. The length of two monolayers of a (110) slab was 4.5815 Åin the z-direction. A vacuum region of around 40 Å was added to each slab model in the z-direction to avoid spurious interactions between periodic replicas. The surfaces of all slab models were passivated by pseudo-hydrogen atoms such that there were no surface states from dangling bonds [131]. Despite α-Sn being a semi-metal passivation is required to remove spurious surface states, as shown in the SI. The InSb/CdTe interface structure has In-Te and Sb-Cd bonds with each In interface atom connected to 3 Sb and 1 Te. The configuration with In-Cd and Sb-Te bonds was also considered but this was found to be less stable by 1.33 eV. Ideal interfaces were considered with no intermixing and no relaxation of the interface atoms was performed.

When constructing such slab models, it is necessary to converge the number of layers to avoid quantum size effects and approach the bulk properties [111]. For InSb it has previously been shown that 42 monolayers are sufficiently converged [115]. Plots of the band gap vs. the number of atomic layers for CdTe(110) and α-Sn (110) slabs are provided in the SI. CdTe was deemed converged with 42 monolayers with a gap value of 1.23 eV, which is only slightly larger than the bulk PBE+U(BO) value. The z-unfolded band structures of CdTe(111) were calculated for a 40 monolayer slab. A 26 monolayer slab model was used to simulate the 2

$\times$ 2 reconstruction, due to the higher computational cost of the 2 $\times$ 2 supercell. Structural relaxation was performed for the top two monolayers of the 2 $\times$ 2 reconstruction. For the slab of unstrained (110) α-Sn, 70 monolayers were needed to close the gap at the zero-gap point of the semi-metal, which corresponds to around 16 nm. The tri-layer slab models comprised 42 layers of InSb, 70 layers of α-Sn and between 0 and 16 layers of CdTe in two-layer increments, amounting to a total slab thickness of around 300 nm (not including vacuum). The (110) bi-layer slab models comprised 42 layers of CdTe and InSb, and 70 layers of α-Sn as these were deemed converged.

4.3 Results and Discussion

4.3.1 α-Sn

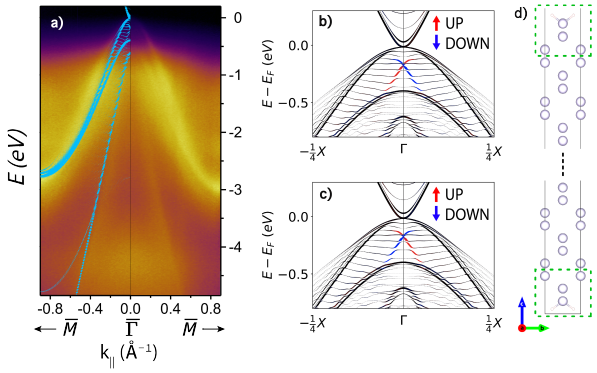

Figure 4.2: Electronic structure of α-Sn: (a) Bulk-unfolded band structure of an α-Sn (001) slab with 51 atomic layers (light blue) compared with ARPES data for a sample of the same thickness. The point $\overline{M}$ is at 0.9298 Å^{-1}. The ARPES data is cutoff at 0.9 Å^{-1} due to experimental artifacts at the edges. Spin-polarized band structures projected onto (b) the top surface atoms and (c) the bottom surface atoms, indicated by the green boxes on the slab structure illustrated in (d). Figure taken from [1]

ARPES experiments were conducted for a 51 monolayer thick α-Sn(001) film, using a photon energy of 63 eV, as described in the SI. Figure 4.2a shows the bulk unfolded

PBE+U(BO) band structure for a 51 monolayer thick α-Sn (001) slab, compared to the ARPES data. The point $\overline{M}$ is at 0.9298 Å^{-1}. The ARPES data is cutoff at 0.9 Å^{-1} due to experimental artifacts at the edges. The PBE+U (BO) band structure is in excellent agreement with ARPES. The top of the valence band in the ARPES and the simulated band structure lines up and the bulk bands are reproduced well. The bandwidth of the heavy hole band, Γ_8, is slightly underestimated, consistent with Ref. [115]. This is corrected by the HSE functional, as shown in the SI for a bulk unit cell of α-Sn with a (001) orientation. However, it is not feasible to use HSE for the large interface models studied here, owing to its high computational cost.

The previously reported topological properties of α-Sn slabs are also observed here [86, 87, 88, 89, 94, 95, 90, 114]. The spin-polarized topological surface state (TSS) is shown in panels (b) and (c) of Figure 4.2 for a (001) 51 monolayer slab along the $X - \Gamma - X$ k-path. As expected, the TSS is characterized by a linear dispersion with the top and bottom surfaces having opposite spin polarization. The associated Rashba-like surface states are also observed along the $K - \Gamma - K$ k-path, as shown in the SI. This linear surface state is also observed in the (110) slabs used to construct the bilayer and tri-layer models. Notably there is an energy gap between the top and bottom TSSs, which closes at 70 layers, the same thickness at which the band gap closes. This gap is possibly induced by the hybridization of the top and bottom surface states in under-converged slabs. We note that the effect of strain on the electronic structure of α-Sn is not studied here.

4.3.2 CdTe

Figure 4.3 shows a comparison of band structures obtained using PBE+U(BO) to the ARPES experiments of Ren *et al.* [2] for CdTe(111). Ren *et al.* collected ARPES data at photon energies of 19, 25 and 30 eV. Here, we compare our results with the second-derivative maps of the ARPES data taken at 25 eV along the k-paths $\overline{\Gamma} - \overline{M}$ (panels (a) and (b)) and $\overline{\Gamma} - \overline{K} - \overline{M}$ (panels (c) and (d)). The original data has been converted to gray scale and reflected around $k_x = 0$. To facilitate the qualitative comparison of the DFT band structure features with the ARPES experiment, we apply a Fermi energy shift of

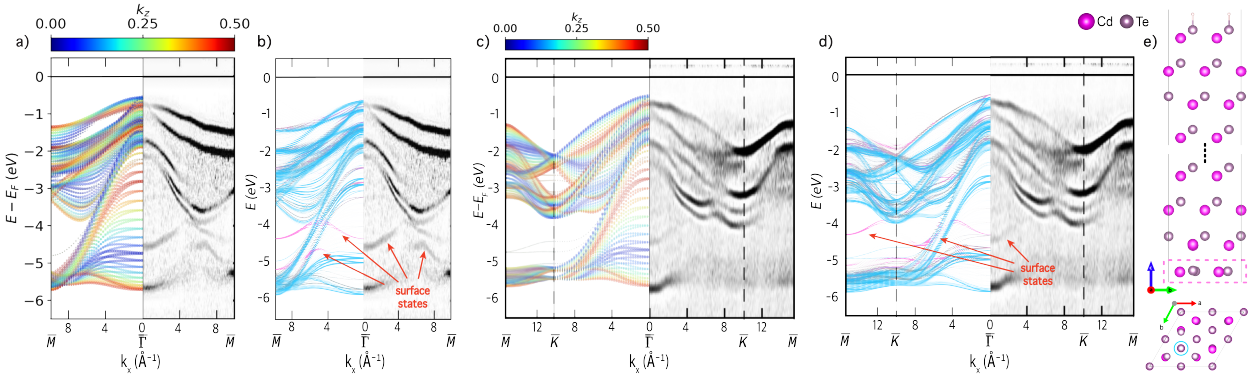

Figure 4.3: Electronic structure of CdTe: Z-unfolded band structures of CdTe(111) compared with second-derivative map of ARPES data (black and white), adapted with permission from "Spectroscopic studies of CdTe(111) bulk and surface electronic structure" by J. Ren *et al.*, Phys. Rev. B, 91, 235303 (2015); Copyright (2015) by the American Physical Society [2]. Z-unfolded band structures compared to ARPES data along (a), (b) $\overline{\Gamma} - \overline{M}$ and (c), (d) $\overline{\Gamma} - \overline{K} - \overline{M}$. (a), (c) Dependence of the band structure on k_z. (b), (d) Mixture of $k_z = 0.0$ and $k_z = 0.5$ (cyan) for a model with a 2×2 surface reconstruction with the contributions of the surface atoms shown in pink. The DFT band structures are shifted by -0.25 eV and stretched by a factor of 1.22 for comparison. (e) Illustration of the 2×2 surface reconstruction with the Cd atom removed indicated by a blue circle. The atoms used for the surface projection are indicated by a pink dashed box. Figure taken from [1]

0.25 eV to line up the VBM and a stretch factor of 1.22 to compensate for the bandwidth underestimation of PBE+U(BO), particularly for bands deep below the Fermi energy [132]. Bandwidth underestimation by PBE+U(BO) compared with HSE and ARPES has also been reported for InAs and InSb in [115, 133]. The original computed band structure without the shift and stretch is provided in the SI.

Owing to the low mean free path at this photon energy, the spectrum appears integrated over a certain k_z interval and surface contributions are readily visible in the ARPES [117, 118]. To account for the different k_z contributions, the z-unfolding method was employed, as described in Section 4.2.1. Panels (a) and (c) show the z-unfolded band structures as a

function of k_z for slab models without a surface reconstruction (figures with single values of k_z are provided in the SI). This is used determine which k_z values are likely present in the experiment. A mixture of $k_z = 0$ and $k = 0.5$ provides the best agreement with the ARPES data. This combination of k_z values is used for the DFT data shown in cyan in panels (b) and (d). This is consistent with the k_z broadening with contributions centered around $k_z = 0$ and $k = 0.5$ often present in ARPES data taken at low mean field path energies in gapped materials [119, 134, 120].

To account for the presence of surface states, we modeled the CdTe(111)A-(2×2) surface reconstruction [135], illustrated in panel (e). A comparison to the unreconstructed surface is provided in the SI. The atom-projected band structures of the bottom layer (indicated by pink dashed box) are plotted in pink in panels (b) and (d). The additional bands arising from the surface reconstruction are in close agreement with the bands in the ARPES labeled as surface states by Ren *et al.*, indicated by red arrows. These surface states are unaffected by the choice of k_z. By accounting for the contributions of different k_z values and for the presence of surface states excellent agreement with experiment is achieved, as the DFT band structures reproduce all the features of the ARPES.

4.3.3 Bilayer Interfaces

We begin by probing the local electronic structure at the the InSb/α-Sn bi-layer interface. Figure 4.4a shows the DOS as a function of position across the interface, indicated by the atomic layer number. Figure 4.4b shows the local DOS at select positions. The Fermi level is positioned at the semi-metal point of the α-Sn and in the gap of the InSb. We note that the α-Sn appears as if it has a small gap due to an artifact of the 10^{-4} cutoff applied in the log plot in panels (a) and (d). The local DOS plots shown in panels (b) and (e) and the band structure plots shown in panels (c) and (f) clearly show the semi-metal point. No significant band bending is found for InSb, as expected from branching point theory [136, 137]. See sec.4.5.3 for more details.

Based on the element-projected band structure, shown in panel (c), the InSb conduction band minimum (CBM) lies 0.09 eV above the α-Sn semi-metal point and the InSb valence

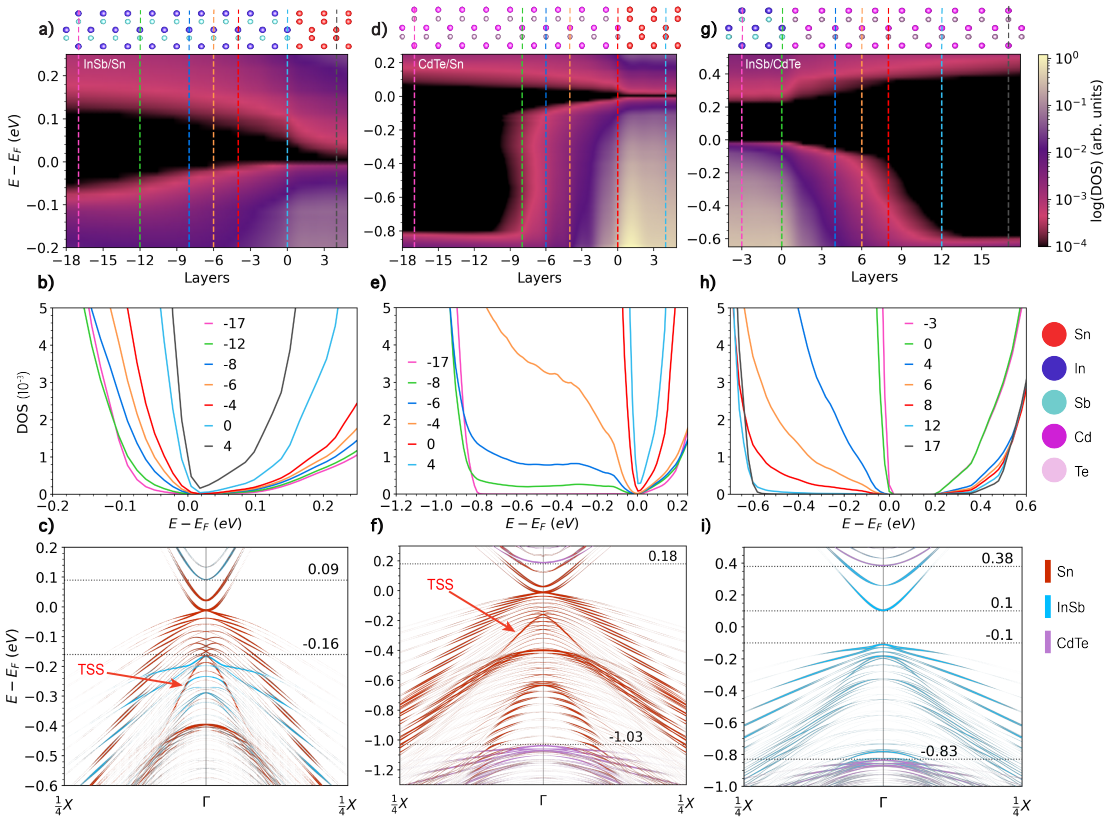

Figure 4.4: Electronic structure of bilayer interfaces: Density of states in the (a) InSb/α-Sn, (d) CdTe/α-Sn and (g) InSb/CdTe interfaces as a function of position. The atomic layers are numbered based on distance from the interface, which is located at zero. The structure of each interface is illustrated on top. (b Local density of states for selected layers in the (b) InSb/α-Sn, (e) CdTe/α-Sn and (h) InSb/CdTe interfaces, indicated by dashed lines in the same colors in panels (a), (d), and (g), respectively. Element projected band structures of the (c) InSb/α-Sn, (f) CdTe/α-Sn and (i) InSb/CdTe interfaces, with bands originating from α-Sn colored in red, bands originating from InSb colored in light blue, and bands originating from CdTe colored in purple. Figure taken from [1]

band maximum (VBM) lies 0.16 eV below it. A linear TSS is present in the α-Sn. Based on an atom projected band structure, shown in the SI, the origin of this state is the top surface of α-Sn, adjacent to the vacuum region. A TSS is no longer present in the α-Sn

layers at the interface with InSb, possibly owing to hybridization between the α-Sn and InSb [114]. Metal-induced gap states (MIGS) are an inherent property of a metal/semiconductor interface, produced by the penetration of exponentially decaying metallic Bloch states into the gap of the semiconductor [138, 139, 140], see Sec.4.5.3 for more details. The presence of MIGS manifests in Figure Figure 4.4a as a gradually decaying non-zero DOS in the band gap of the InSb in the vicinity of the interface. Figure 4.4b shows that the MIGS are prominent in the first few atomic layers and become negligible beyond 8 layers from the interface.

Figure 4.4d shows the DOS as a function of position across the CdTe/α-Sn interface, indicated by the atomic layer number. Figure 4.4e shows the local DOS at select positions. The Fermi level is positioned at the semi-metal point of the α-Sn and in the gap of the CdTe. Based on the projected band structure, shown in panel (f), the CdTe CBM is positioned 0.18 eV above the Fermi level and the CdTe VBM is located 1.03 eV below the Fermi level. This agrees with previous reports that interfacing with Sn brings the conduction band of the CdTe closer to the Fermi energy, with downward band-bending of 0.25 eV [141] and 0.1 eV [142]. We find a valence band offset of around 1 eV, similar to the (110) and (111) interfaces reported in [143, 144, 142, 145, 92, 146]. Close to the interface there is a significant density of MIGS, which decay within about 10 layers (3-4 nm) into the CdTe. This suggests that this number of CdTe layers may be required for an effective tunnel barrier.

Figure 4.4g shows the DOS as a function of position across the InSb/CdTe interface, indicated by the atomic layer number. Figure 4.4h shows the local DOS at select positions. The band alignment is type-I with the CdTe band gap straddling the InSb band-edges. The Fermi level is close to the InSb VBM and around the middle of the gap of the CdTe. No band bending is found in either material. Based on the projected band structure, shown in panel (i), the CdTe CBM lies 0.28 eV above the InSb CBM and the CdTe VBM lies 0.75 eV below the InSb VBM. These values are similar to the band offsets reported in references [84, 147, 148]. Because the band gap of InSb is significantly smaller than that of CdTe, states from the InSb penetrate into the gap of the CdTe, similar to MIGS. These states decay gradually and vanish at a distance greater than 12 layers from the interface.

4.3.4 Tri-layer Interfaces

Figure 4.5 shows the DOS as a function of position across InSb/CdTe/α-Sn tri-layer interfaces with varying thickness of the CdTe tunnel barrier. Interfaces with 6, 10, and 16 layers of CdTe are shown here and additional results for interfaces with 2, 4, and 8 layers are provided in the SI. The position is indicated by the atomic layer number, with the layer of InSb closest to the CdTe considered as zero. Panels (a) and (b) show that with 6 atomic layers of CdTe, the MIGS from the α-Sn penetrate through the tunnel barrier into the first 12 layers of the InSb. For a thin layer of CdTe, the band gap is expected to be significantly larger than the bulk value because of the quantum size effect (see the gap convergence plot in the SI). However, owing to the presence of MIGS, the gap of the CdTe remains considerably smaller than its bulk value. With 10 layers of CdTe, shown in panels (c) and (d), there is still a significant presence of MIGS throughout the CdTe, which decay by 6 layers into the InSb. Panels (e) and (f) show that with 16 layers of CdTe the InSb is completely insulated from MIGS coming from the α-Sn. The gap of the CdTe reaches a maximum of around 0.3 eV at a distance of 5 layers from the InSb. This is because MIGS from the α-Sn penetrate into the CdTe from one side, whereas states from the InSb penetrate from the other side, such that the band gap of the CdTe never reaches its expected value.

Figure 4.6 summarizes the band alignment at the bilayer and tri-layer interfaces studied here. For the tri-layer interfaces, the band alignment between the InSb and the α-Sn is not significantly affected by the presence of CdTe, as shown in the element-projected band structures in the SI. The α-Sn semi-metal point remains pinned at the Fermi level, as in the bilayer InSb/α-Sn (see also Figure 4.4c). The InSb VBM remains at 0.17 eV below the Fermi level, similar to its position in the bilayer interface, regardless of the CdTe thickness. The InSb CBM position shifts slightly with the thickness of the CdTe from 0.09 eV above the Fermi level without CdTe, to 0.054 eV with 6 layers of CdTe, 0.04 eV with 10 layers, and 0.037 eV with 16 layers. This may be attributed to the quantum size effect, which causes a slight narrowing of the InSb gap because of the increase in the overall size of the system. Based on the element-projected band structures provided in the SI, the band edge positions of the CdTe are dominated by the interface with the α-Sn, rather than the interface with the

InSb. The CdTe CBM remains at 0.18 eV above the Fermi level, as in the bilayer CdTe/α-Sn interface (see also Figure 4.4f), regardless of the number of layers. As the band gap of the CdTe narrows with increasing thickness, the CdTe VBM shifts from 1.24 eV below the Fermi level with 6 layers to 1.105 eV with 10 layers, and 1.05 eV with 16 layers, approaching the bilayer VBM position of 1.03 eV below the Fermi level with 42 layers. Although the band gap of the CdTe is significantly reduced due to MIGS, a type I band alignment with the InSb is maintained, similar to the bilayer InSb/CdTe interface (Figure 4.4g,i), as shown in Figure 4.5 panels (a), (c), and (e).

Figure 4.7 show the LDOS in the second layer of InSb from the interface as a function of the number of CdTe layers. Without CdTe and with two layers of CdTe, there is no band gap in the InSb close to the interface, owing to the significant density of MIGS. With 4 layers of CdTe a gap starts to appear. With 6 layers of CdTe the gap of the InSb close to the interface is still considerably narrower than its bulk value. The band gap in the second layer of InSb from the interface approaches its bulk value with 10 layers of CdTe and finally reaches it with 16 layers of CdTe. This suggests that 16 CdTe layers provide an effective barrier to electronically insulate the InSb from the α-Sn. With present-day methods, we are unable to calculate the current across the interface from first principles. It is reasonable to assume that a barrier of 16 layers or more (over 3.5 nm thick) would all but eliminate transport through the interface into the InSb. We surmise that the barrier thickness range where there is still some overlap between the wave functions of the α-Sn and the InSb, as indicated by the presence of MIGS, is the relevant regime to modulate the coupling strength between the two materials. This calls for experimental studies of the proximity effect at a semiconductor/ superconductor interface with a tunnel barrier in the range of 6-10 layers, where MIGS still exist. We note, however, that the interface with β-Sn may have somewhat different characteristics in terms of the band alignment and the penetration depth of MIGS.

4.4 Conclusion

In summary, we have used DFT with a Hubbard U correction machine-learned by Bayesian optimization to study CdTe as a prospective tunnel barrier at the InSb/α-Sn interface. The results of PBE+U(BO) were validated by comparing the band structures of slab models of α-Sn(001) and CdTe(111) with ARPES experiments (the PBE+U(BO) band structure of InSb(110) had been compared to ARPES experiments previously [115]). Excellent agreement with experiment is obtained for both materials. In particular, for the low-mean-free-path ARPES of CdTe, the z-unfolding scheme successfully reproduces the contributions of different k_z values and modelling the 2×2 surface reconstruction successfully reproduces the contributions of surface states.

We then proceeded to use PBE+U(BO) to calculate the electronic structure of bilayer InSb/α-Sn, CdTe/α-Sn, and InSb/CdTe, as well as tri-layer InSb/CdTe/α-Sn interfaces with varying thickness of CdTe. Simulations of these very large interface models were possible thanks to the balance between accuracy and computational cost provided by PBE+U(BO). We find that the most stable configuration of the InSb/CdTe interface is with In-Te and Sb-Cd bonding. MIGS penetrate from the α-Sn into the InSn and CdTe. Similarly, states from the band edges of InSb penetrate into the larger gap of the CdTe. No interface states are found in any of the interfaces studied here, in contrast to the EuS/InAs interface, for example, in which a quantum well interface state emerges [149].

For all interfaces comprising α-Sn, the semi-metal point is pinned at the Fermi level. For the tri-layer interface, the band alignment between the InSb and the α-Sn remains the same as in the bilayer interface regardless of the thickness of the CdTe barrier, with the Fermi level closer to the conduction band edge of the InSb. The band edge positions of the CdTe are dominated by the interface with the α-Sn rather than the interface with InSb, with the conduction band edge being closer to the Fermi level. A type-I band alignment is maintained between CdTe and InSb with the gap of the former straddling the latter. The CBM of the CdTe is pinned whereas the VBM shifts upwards towards the Fermi level as the gap narrows with the increase in thickness.

We find that 16 layers of CdTe (about 3.5 nm) serve as an effective barrier, preventing

the penetration of MIGS from the α-Sn into the InSb. However, in the context of Majorana experiments, it is possible that a barrier thick enough to completely insulate the semiconductor from the superconductor would also all but eliminate transport. Therefore, we estimate that the relevant regime for tuning the coupling at the interface would be in the thickness range where some MIGS are still present. Thicker CdTe layers could be used to passivate exposed InSb surfaces. We note that the interface with the superconducting β-Sn, which is not lattice matched to InSb and CdTe, may have different characteristics than the interface with α-Sn. Careful experimentation is needed to establish a connection between proximity-induced superconductivity or other physical factors that affect the emergence of MZMs and the parameters of the interface, including the band alignment and the presence or absence of interface states and MIGS. Such experiments could be pursued, for example, by varying the CdTe barrier thickness within the range indicated by our simulations and measuring the induced superconducting gap in an InSb nanowire. This would help determine the optimal interface configuration for MZM devices.

We have thus demonstrated that DFT simulations can provide useful insight into the electronic properties of semiconductor/tunnel barrier/metal interfaces. This includes the interface bonding configuration, the band alignment, and the presence of MIGS (and, possibly, of interface states). Such simulations may be conducted for additional interfaces to explore other prospective material combinations. This may inform the choice of interface systems and the design of future Majorana experiments. More broadly, similar DFT simulations of interfaces may be performed to evaluate prospective tunnel barriers *e.g.,* for semiconductor devices.

4.4.1 acknowledgement

We thank Guang Bian from the University of Missouri, Li Fu from Northwestern Polytechnical University, China, and Tai C. Chiang from the University of Illinois at Urbana-Champaign for sharing their ARPES data for CdTe. Work at the University of Pittsburgh was supported by the Department of Energy through grant DE-SC-0019274. Work at CMU and UCSB was funded by the National Science Foundation (NSF) through grant OISE-

1743717. Work in Grenoble is supported by the ANR-NSF PIRE:HYBRID, Transatlantic Research Partnership and IRP-CNRS HYNATOQ. This research used computing resources of the University of Pittsburgh Center for Research Computing, which is supported by NIH award number S10OD028483 and of the National Energy Research Scientific Computing Center (NERSC), a U.S. Department of Energy Office of Science User Facility operated under Contract No. DE-AC02-05CH11231.

4.4.2 suppinfo

Computational details of DFT simulations; Experimental details of ARPES of α-Sn; Comparison of the HSE and PBE+U(BO) band structures of α-Sn and CdTe; Effect of lattice parameter on the band structures of α-Sn and CdTe; Topological properties of α-Sn; Surface passivation of α-Sn; Thickness convergence of α-Sn and CdTe; The 2×2 surface reconstruction of CdTe(111); Additional results for the z-unfolded band structure of CdTe(111); Contribution of the α-Sn surface to the band structure of bilayer InSb/α-Sn; Band alignment of the tri-layer InSb/CdTe/α-Sn interface; Additional results for the tri-layer InSb/CdTe/α-Sn interface with 2,4, and 8 layers of CdTe.

4.5 Additional Methodological Details

4.5.1 Computational Details

DFT calculations were conducted using the Vienna Ab Initio Simulation Package (VASP) [61] with the projector augmented wave method (PAW) [150, 151]. The generalized gradient approximation (GGA) of Perdew, Burke, and Ernzerhof (PBE) [127] was employed to describe the exchange-correlation interactions among electrons with a Hubbard U correction [129]. The U values were machine learned using Bayesian optimization (BO) [107]. Briefly, the BO objective function is formulated to reproduce as closely as possible the band structure obtained from the Heyd-Scuseria-Ernzerhof (HSE) [152] hybrid functional. The reference HSE calculations were conducted for bulk CdTe with a lattice parameter of 6.482 Å and α-Sn with a lattice parameter of 6.489 Å and compared to the results with the lattice constant of InSb, 6.479 Å, which was used for interface models. It was verified that using the lattice constant of InSb does not have an appreciable effect on the electronic properties of CdTe and α-Sn, as shown below.

The hyperparameters of our BO implementation are the coefficients α_1 and α_2, which assign different weights to the band gap vs. the band structure in the objective function, the number of valence and conduction bands used for the calculation of the objective function, N_b, and the parameter κ that controls the balance between exploration and exploitation in the upper confidence bound acquisition function. For InSb the values of $U_{eff}^{In,p} = -0.2$ and $U_{eff}^{Sb,p} = -6.1$ were used, following Ref. [115, 107]. It has been shown that PBE+U(BO) produces a band structure in good agreement with ARPES for InSb [115].

Because α-Sn is a semi-metal, only the band shape was considered in the optimization, *i.e.* α_1 was set to 0 and $\alpha_2 = 1$ [111].The other BO hyperparameters used for Sn were $\kappa = 7.5$ and $N_b = (5, 5)$. This resulted in a value of $U_{eff}^{Sn,p} = -3.04$ eV, slightly different than in Refs. [113, 88, 94], which used empirical methods to choose a U value that yields a correct band ordering. As shown in Ref. [111], PBE+U(BO) reproduces the correct band ordering of α-Sn with the band inversion at the Γ point, in agreement with other studies using DFT+U [87, 86].

For CdTe, we applied a U correction to both the Cd-d orbitals and Te-p orbitals, unlike earlier studies [108, 153]. The hyperparameters used for CdTe were $\kappa = 7.5$, $N_b = (5, 5)$, $\alpha_1 = 0.5$ and $\alpha_2 = 0.5$. The latter two parameters were chosen to assign equal weights to the band gap and the band shape. This led to U values of $U_{eff}^{Cd,d} = 7.381$ and $U_{eff}^{Te,p} = -7.912$. The Cd-d U value obtained here is similar to the 7 eV used in Ref. [153] and somewhat lower than $U_{eff}^{Cd,d} = 8.3$ eV in Ref. [108]. The gap of 1.21 eV, obtained here by applying the Hubbard U correction to both the Te-p states and the Cd-d states is closer to experimental values of around 1.5 eV [154, 147] and the HSE value of 1.31 eV than previous calculations [108].

Spin-orbit coupling (SOC) was used in all calculations and dipole corrections were applied to slab models [155]. The tags used for convergence of calculations were BMIX = 3, AMIN = 0.01, ALGO = Fast, and EDIFF = $1{\cdot}10^{-5}$. The kinetic energy cutoff was set to 400 eV for all bulk calculations and 350 eV for surface and interface slab models. A $9 \times 9 \times 9$ k-point mesh was used for bulk calculations and a k-point mesh of $7 \times 7 \times 1$ was used for surface and interface calculations. All interface density of states (DOS) calculations used a k-point mesh of $13 \times 13 \times 1$.

The pseudo-hydrogen fractional charges utilized to passivate each atom were 1.25 for In and 0.75 for Sb in InSb, 1.5 for Cd and 0.5 for Te in CdTe, and 1 for Sn. Structural relaxation of the pseudo-hydrogen atoms was performed until the maximal force was below 0.001 eV/Å.

All band structure and density of states plots were generated using the open-source Python package, VaspVis [111], which is freely available from The Python Package Index (PyPI) via the command: *pip install vaspvis*, or on GitHub at: `https://github.com/DerekDardzinski/vaspvis`

4.5.2 ARPES Experimental details

Angle resolved photo emission spectroscopy (ARPES) is an experimental technique that can map the electronic band structure below the Fermi level of crystalline materials, based on measuring the emitted photoelectrons from materials [117, 119]. It can be applied using a

range of photon energies, usually 20–100 eV, where the photoelectron mean free path, which defines the probing depth of the electrons, is of the order of 5 Å. Using this, the effective electronic density of states is measured, i.e. the spectral function. And, via resolving the angle which accesses the momentum dependency of the state, this can mapped to properties such as the band structure

The α-Sn samples were grown by molecular beam epitaxy on an In-terminated c(8 $\times$ 2) InSb(001) surface prepared by atomic hydrogen cleaning. 51 monolayers (16.5 nm) of α-Sn were deposited as calibrated via Rutherford backscattering spectrometry. Growth was performed at a substrate temperature of -20 °C and a base pressure better than $1{\cdot}10^{-10}$ Torr. The ARPES measurements were taken at Beamline 10.0.1.2 at the Advanced Light Source in Berkeley. The base pressure was better than $5{\cdot}10^{-11}$ Torr while the sample temperature was held at 68 K. The sample was illuminated with 63 eV p-polarized light and spectra were collected using a Scienta R4000 detector with energy resolution better than 40 meV and angular resolution better than 0.1°. The sample was transferred via vacuum suitcase with a base pressure better than $\cdot 10^{-11}$ Torr between the growth chamber and beamline. A photon energy of 63 eV corresponds to a $\mathbf{k}_z$ approximately 0.15 Å^{-1} above the $\mathbf{\Gamma}_{002}$ point.

4.5.3 Interfacing affects

Metal-induced gap states (MIGS) are an inherent property of a metal/semiconductor interface, produced by the penetration of exponentially decaying metallic Bloch states into the gap of the semiconductor [138, 139]. The metallic wavefunctions that penetrate into the semiconductor are imaginary block states with complex k-vector, and therefore they decay when in the semiconductor. Where the Fermi level is in the semiconductor band gap is also important. For example, if the Fermi level is close to the bottom of the conduction band, the wavefunctions of the metal tail into the semiconductor all over the gap. Collectively they are then negatively charged since, above their charge-neutrality-level, the tailing states are mainly derived from the conduction band and they are thus of acceptor type [140]. Additionally, MIGS can lead to Fermi level pinning at the interface, where a high-density of states can pin Fermi level at the charge-neutrality-level [156] The (MIGS) model has also

been successfully used to explain Schottky barrier heights and their variation with the metal work function in many different semiconductors and insulators. This states that the Schottky barrier height is determined by the consistently induced electronic charge accumulated at a metal-semiconductor interface. One benefit of in DFT is that MIGS can be readily seen as these calculations are done at T=0 and, usually, for defect free systems. In experimental defects and finite temperatures affects can often reduce the prevalence of MIGS making it difficult to measure such quantities.

Band bending is a common affect at the interface of a semiconductor and metal. For example, if there is downward band bending of the semiconductor, such as at an InAs/Al interface, this indicates that electrons are transferred from the metal to the semiconductor. This happens due to the equilibrating chemical potentials (Fermi energies) of two surfaces that have come into contact, which is done by transferring charge carriers across the interface. If the semiconductor has a larger work function than the metal then an accumulation layer could form. This leads to the surface of the semiconductor becoming negative, lowering the semiconductor band at the interface, i.e. band bending down, due to the lowering of the potential energy the electrons need to cross the interface into the positively charged metal surface [157]. In metals, the electric field is quickly screened due to the large concentration of free charge carriers, leading to virtually no band bending. In semiconductors, due to the lower charge carrier concentration, leads to a larger screening length of the electric field.

4.6 Additional Results

4.6.1 Pseudo-hydrogen Passivation

To create a surface, such as the ones made in the used finite slab models, bonds must be broken. In materials exhibiting covalent and ionic bonding, the presence of dangling bonds can lead to undesired surface states and charge transfer between surfaces, particularly for polar surfaces [158]. Experimental approaches employ various passivating agents to address this issue. Group IV semiconductors like Si or Ge are commonly passivated with hydrogen to

eliminate dangling bonds. Conversely, for more intricate heteropolar surfaces such as III-V and II-VI semiconductors, large organic ligands are employed [159, 160]. To circumvent the need for explicit modeling of the passivating agent, Shiraishi [158] proposed the utilization of pseudo-potentials for fractionally charged hydrogen ($^{\alpha}$H) to terminate surface dangling bonds by forming perfect covalent bonds. The value of fractional charge, α, can generally be determined using the following equations, initially proposed by Wang and Li [161], and later generalized by [162]. For an anion or uncharged surface atom, α is

$$\alpha = \frac{8 - Z}{X}. \tag{27}$$

Where Z is the number of valence electrons of the surface atom, and X is the coordination number of the surface atom. If the surface atom is a cation then α is

$$\alpha = \frac{2X - Z}{X}. \tag{28}$$

For example, for an As-terminated InAs(111) surface, $Z_{\mathrm{As}} = 5$ and $X_{\mathrm{As}} = 4$ due to the tetrahedral bonding in the zinc-blende structure, meaning $^{0.75}$H atoms should be used to passivate the As-terminated surface.

The presence of unpassivated dangling bonds can significantly affect the electronic structure of the surface.

Figure 4.12 provides a comparison between the band structures of unpassivated and passivated InSb (111) α-Sn with 41 atomic layers and a 60 Åvacuum. In the band structure of the unpassivated slab, shown in panel (b) several spurious surface states, originating from both surfaces, appear in the band gap region. Once the surfaces are passivated with pseudo-hydrogens, these surface states disappear, shown in panel (a). When working with interface models that contain a vacuum region, it is essential to passivate the ends of the slab model that are exposed to the vacuum in order to remove unwanted surface states from the electronic structure and focus on the interface states, as well as reducing the dipole moment of the slab.

Note that the surface isn't passivated when there is interest in the surface states so the effect of the dangling bonds on the surface can be discerned, as is the case for the 2×2 CdTe, shown in Figure 4.13. Relaxation of the surface atoms is still undertaken. In experiments

surface reconstructions form to minimize dangling bond energies. One effect of passivating is circumnavigating the need for reconstructions because this removes dangling bonds. Additionally, passivation is comparatively cheaper way to deal with surfaces compared to surface reconstructions.

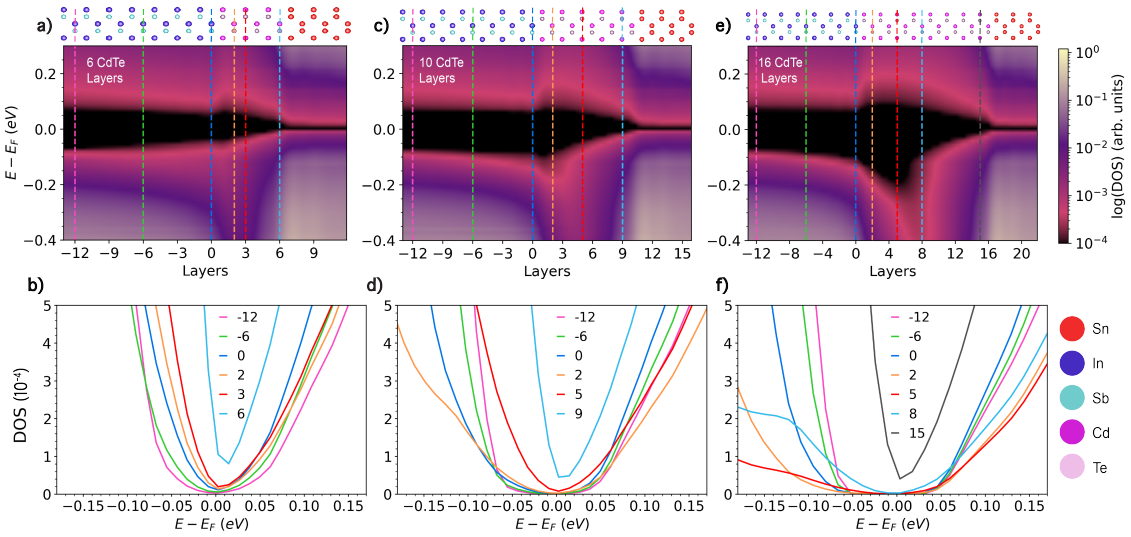

Figure 4.5: Electronic structure of InSb/CdTe/α-Sn tri-layer interfaces: Density of states as a function of distance from the interface for (a) 6, (c) 10 and (e) 16 CdTe barrier layers. The atomic layers are numbered based on distance from the interface, which is located at zero. Interface structures are illustrated on top. (b), (d), (f) Local density of states for selected layers, indicated by dashed lines in the same colors in panels (a), (c), and (e), respectively. Figure taken from [1]

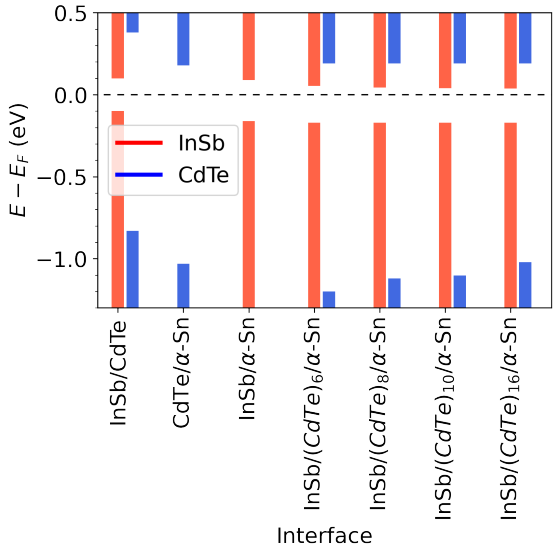

Figure 4.6: Valence and conduction band edge positions for InSb and CdTe in the bilayer and tri-layer interfaces. The Fermi level is at the semi-metal point of the α-Sn. Figure taken from [1]

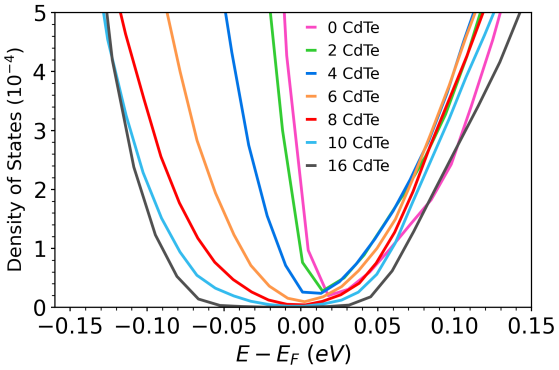

Figure 4.7: Density of states in the second InSb layer from the interface (layer -2 in Figure 4.5) as a function of the number of CdTe barrier layers. Figure taken from [1]

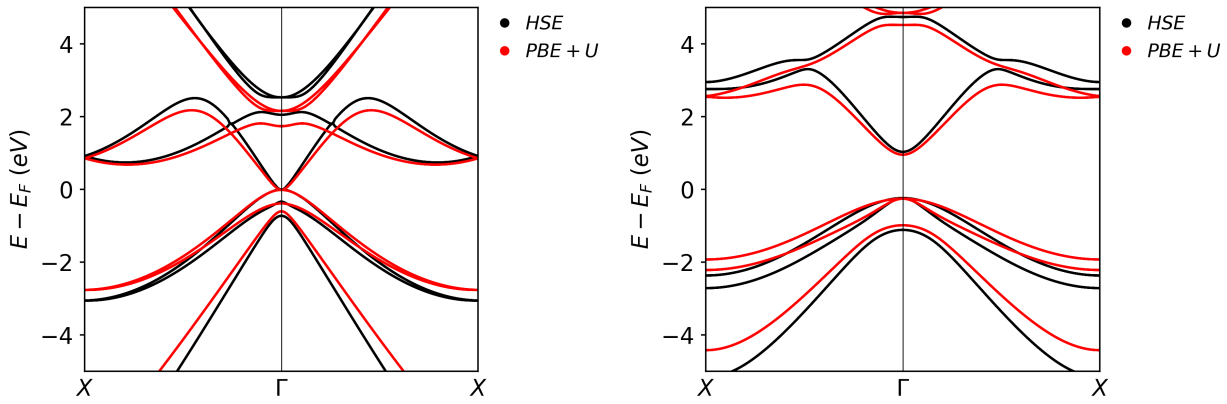

Figure 4.8: Comparison of the HSE and PBE+U(BO) band structures of (a) α-Sn and (b) CdTe. The band width is slightly underestimated by PBE+U(BO). This is the reason for the stretch factor applied in the comparison to ARPES for CdTe. Figure taken from [1]

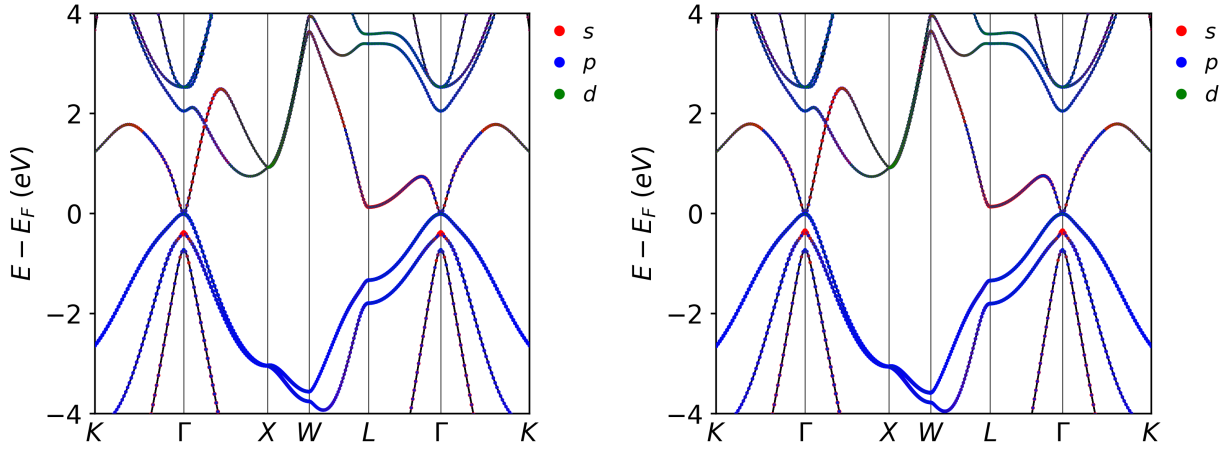

Figure 4.9: Comparison of the HSE band structures of α-Sn obtained with the lattice constant of (a) 6.489 Å of α-Sn and (b) 6.479 Å of InSb. The small difference in the lattice constant has no appreciable effect on the electronic properties. Figure taken from [1]

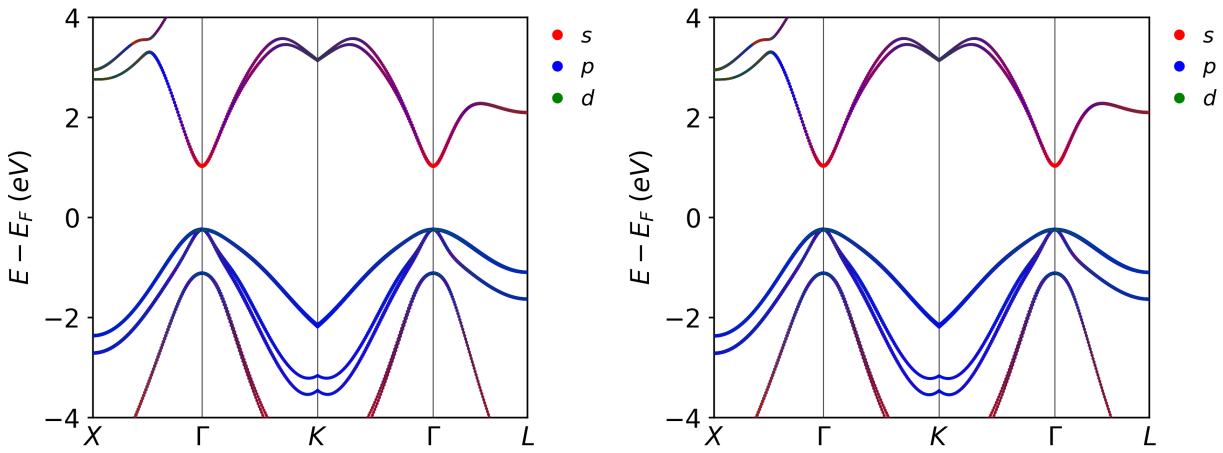

Figure 4.10: Comparison of the HSE band structures of CdTe obtained with the lattice constant of (a) 6.482 Å of CdTe and (b) 6.479 Å of InSb. The band gaps are 1.266718 eV and 1.270622 eV respectively. The small difference in the lattice constant has no appreciable effect on the electronic properties. Figure taken from [1]

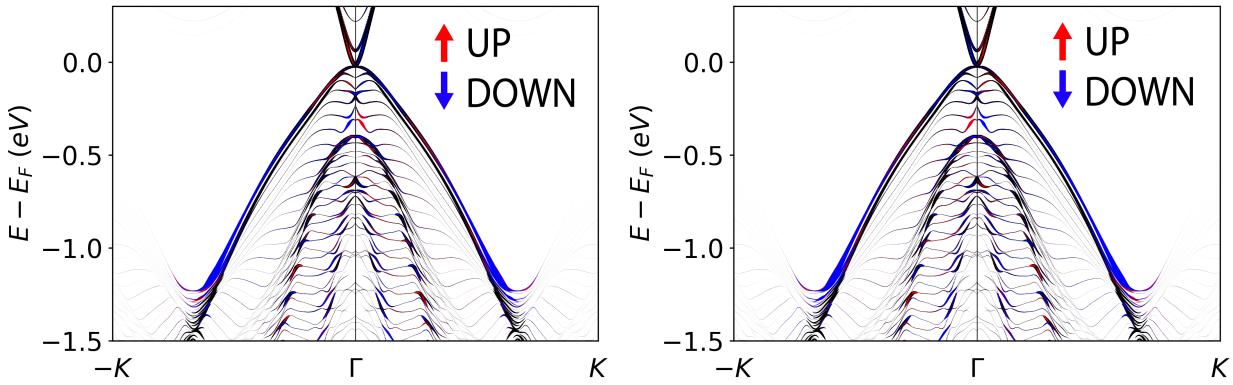

Figure 4.11: Topological properties of α-Sn: Band structure along the $K - \Gamma - K$ k-path obtained with PBE+U(BO) for an unstrained α-Sn(001) slab with 51 atomic layers. The spin decomposed output has been projected onto the (a) top and (b) bottom two monolayars of the slab, highlighting the TSS1 state and the RSS state on the surface of the slab. The RSS up and down spin polarized surface states are mostly degenerate. Figure taken from [1]

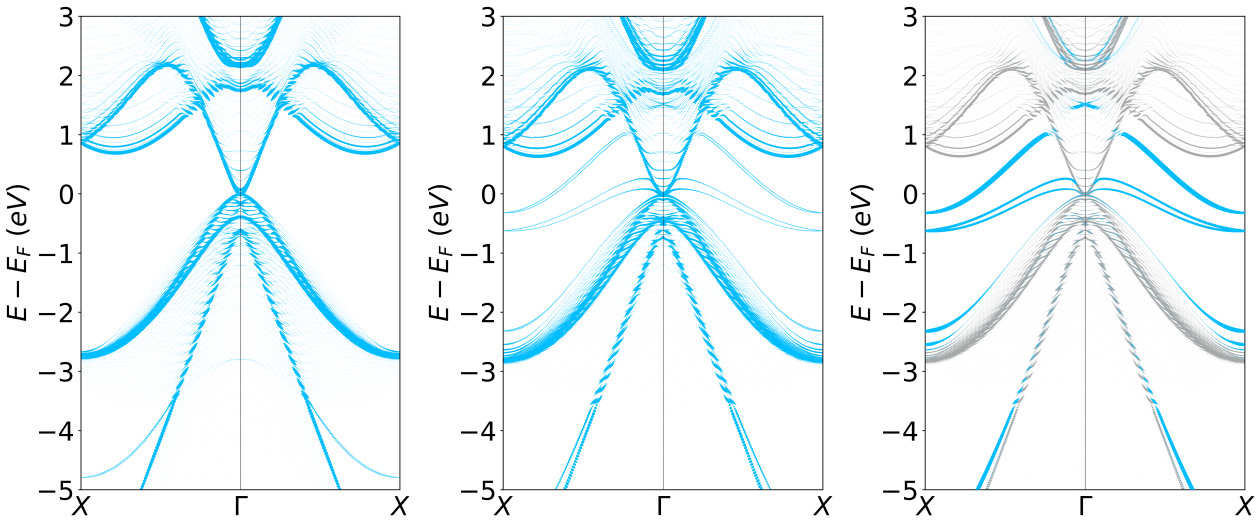

(a) (b) (c)

Figure 4.12: Surface passivation of α-Sn: Band structures of an α-Sn slab with 41 monolayers (a) with surface passivation and (b) without surface passivation, showing the spurious states due to dangling bonds. (c) Projected band structure with the contributions of the top two monolayers of a slab with no passivation colored in blue. This shows that the additional states surface states, which disappear when the dangling bonds are passivated. Figure taken from [1]

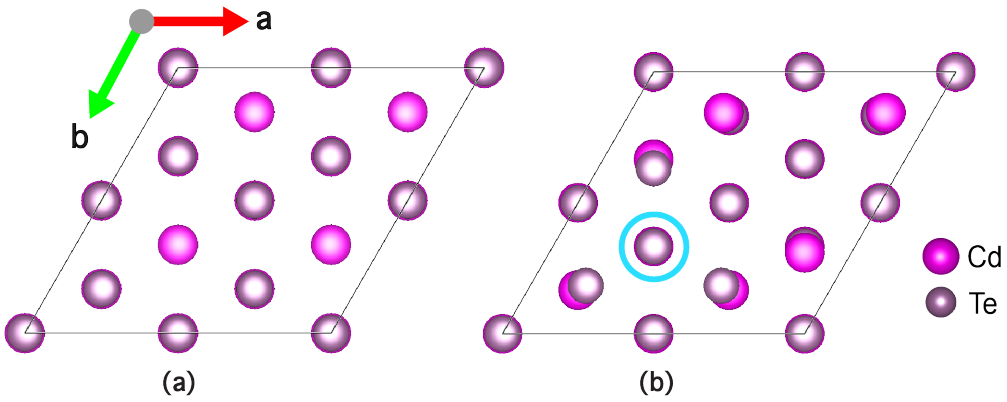

Figure 4.13: The 2 × 2 surface reconstruction of CdTe(111): Top view of (a) unreconstructed surface and (b) reconstructed and relaxed surface with the removed Cd atom indicated by a blue circle. Figure taken from [1]

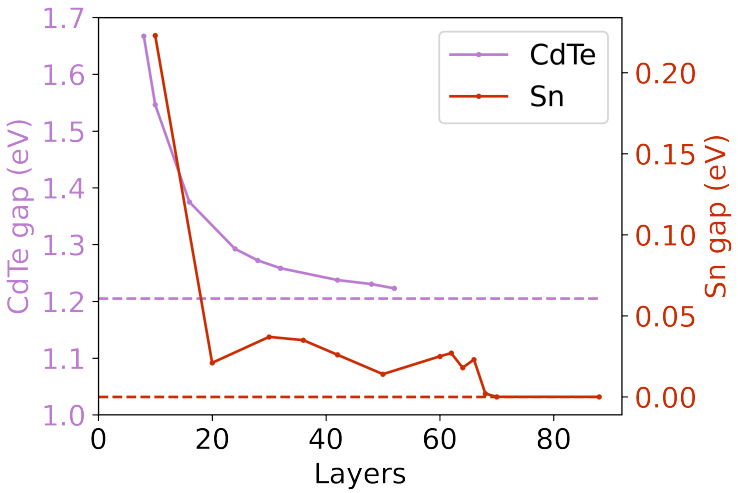

Figure 4.14: Thickness convergence of α-Sn and CdTe: The Γ-point band gap of CdTe(110) and α-Sn(110) as a function of number of atomic layers. Dashed lines denote the PBE+U(BO) bulk limit of 1.205 eV for CdTe and 0 eV (zero-gap) for Sn. Oscillatory behavior is observed for α-Sn(110). Similar behavior has been reported in other materials with a TSS [3]. This behavior could arise from hybridization of the top and bottom surface states, which may cause finite size effects such as band gap oscillations with layer number in topological crystalline insulators [4, 5]. Figure taken from [1]

4.6.2 CdTe

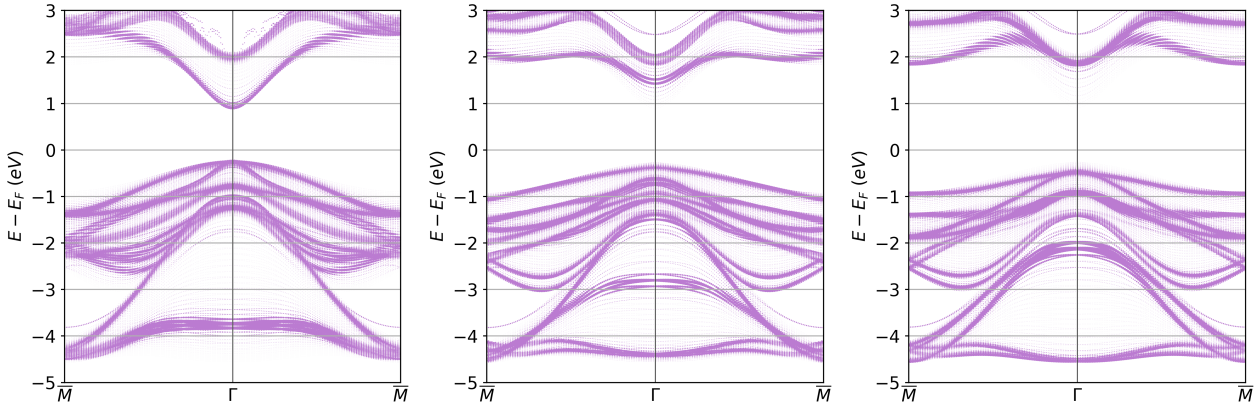

(a) (b) (c)

Figure 4.15: Dependence on the z-unfolded band structure of CdTe(111) on the choice of k_z: (a) $k_z = 0$ (b) $k_z = 0.3$ and (c) $k_z = 0.5$. Figure taken from [1]

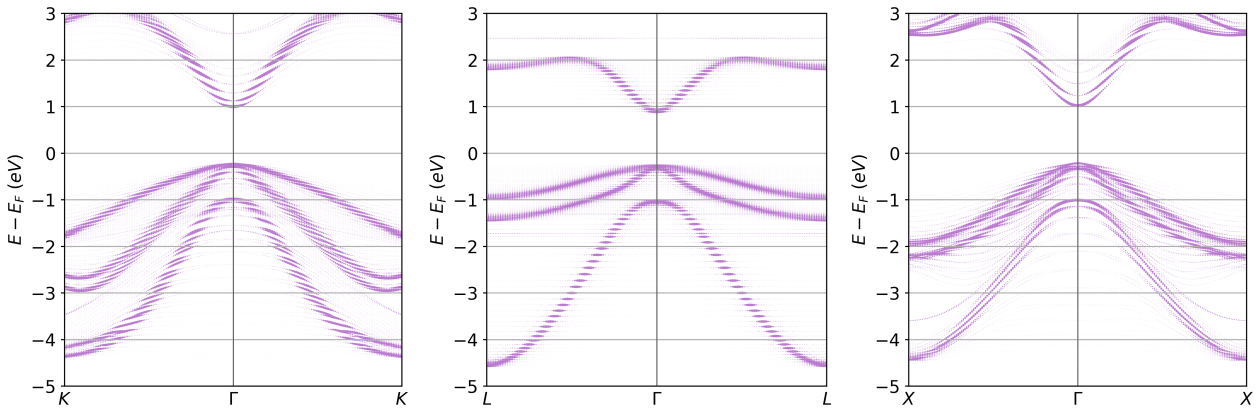

(a) (b) (c)

Figure 4.16: Some bulk paths with contributions to the z-unfolded band structures of CdTe(111) (shown in Figure 4.15): (a) $K - \Gamma - K$, (b) $L - \Gamma - L$, and (c) $X - \Gamma - X$. Figure taken from [1]

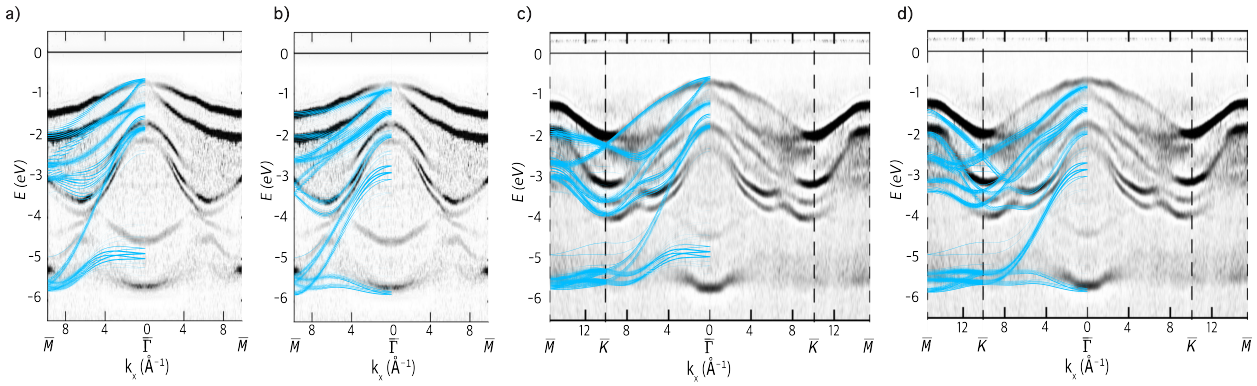

Figure 4.17: Electronic structure of CdTe: Z-unfolded PBE+U(BO) band structures of CdTe(111) compared with second-derivative map of ARPES data (black and white), adapted with permission from "Spectroscopic studies of CdTe(111) bulk and surface electronic structure" by J. Ren *et al.*, Phys. Rev. B, 91, 235303 (2015); Copyright (2015) by the American Physical Society [2]. Z-unfolded band structures compared to ARPES data along (a), (b) $\overline{\Gamma} - \overline{M}$ and (c), (d) $\overline{\Gamma} - \overline{K} - \overline{M}$. The computed band structures are shown for (a), (c) for $k_z = 0.0$ and (b), (d) $k_z = 0.5$. A shift of -0.25 eV and a stretch factor of 1.22 were applied to the DFT band structures for comparison. This shows that a mix of both k_z values is needed to best reproduce the experimental data. Figure taken from [1].

4.6.3 Bilayers and trilayers

4.6.4 Trilayer wavefunction and avoided energy crossing

The effect on the InSb conduction band from the α-Sn was investigated via plotting the the wavefunction of the InSb conduction band as a function of position on the slab for different numbers of CdTe layers, shown in Figure 4.23. This shows the planar averaged (XY planes) positional charge density (electron wavefunction) of four k-points from the conduction around the Γ point . The conduction band was chosen as experimentally MZM physics utilizes this band, a bias voltage is used to tune Fermi energy to the conduction band in experiments. With less than 16 tunnel barrier layers the InSb conduction band wavefunction has significant weight in the Sn section of the slab. This could imply a strong

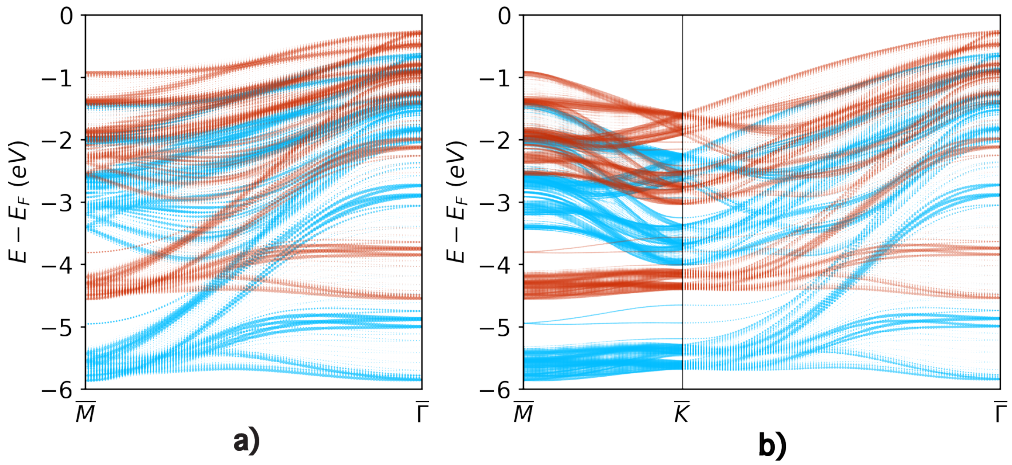

Figure 4.18: Original z-unfolded band structures (red) compared with the band structures shifted by -0.25 eV and stretched by a factor of 1.22 (light blue). This is shown for CdTe(111) with a mixture of $k_z = 0.0$ and $k_z = 0.5$ for k-paths (a) $\overline{\Gamma} - \overline{M}$ and (b) $\overline{\Gamma} - \overline{K} - \overline{M}$. Figure taken from [1].

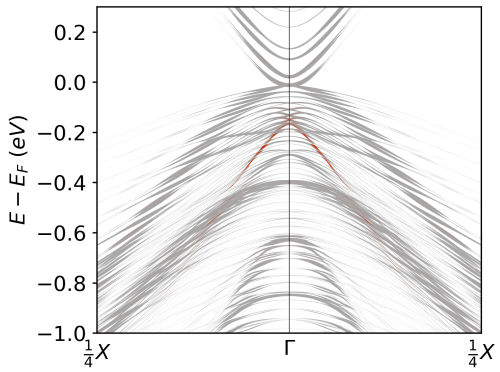

Figure 4.19: Bulk unfolded band structure of the bilayer InSb/α-Sn interface. The contributions of the top two surface monolayers of α-Sn, which are not in contact with InSb, are colored in red. This shows that the TSS originates from the α-Sn surface on the top of the slab. Figure taken from [1].

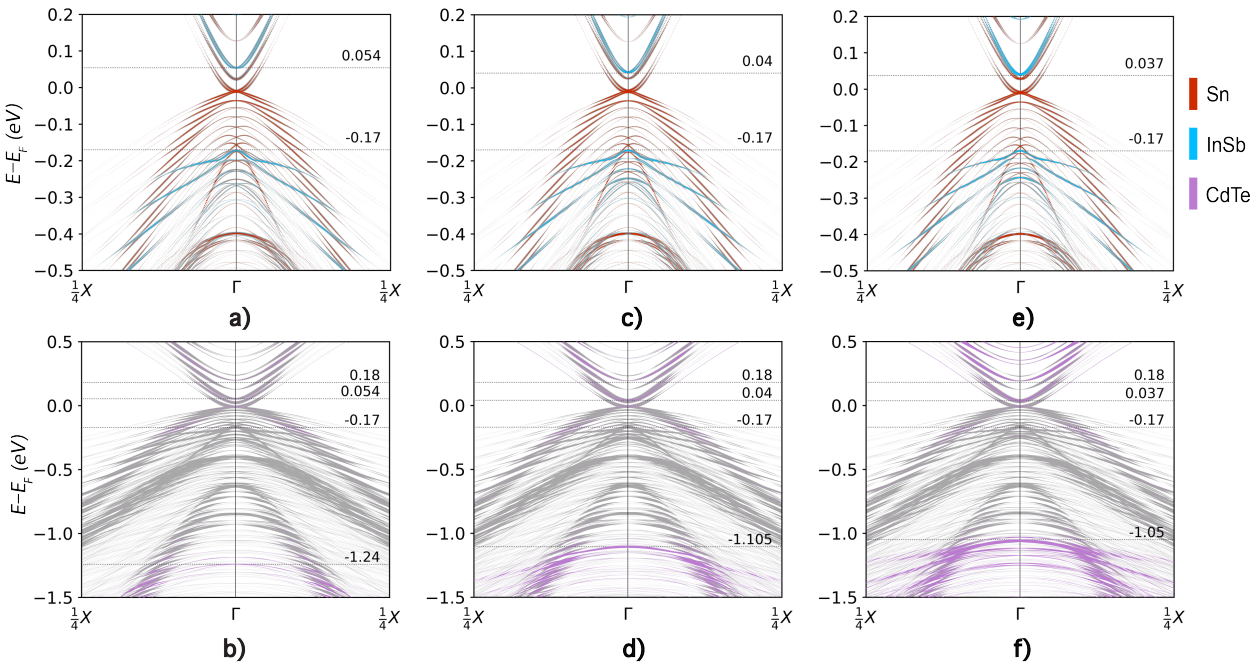

Figure 4.20: Band alignment of the tri-layer InSb/CdTe/α-Sn interface: Element projected band structures of with (a,b) 6 atomic layers, (c,d) 10 layers, and (e,f) 16 layers of CdTe. The bands originating from α-Sn, InSb, and CdTe are colored in red, light blue, and purple, respectively. Panels (b), (d) and (f) only show the CdTe contributions, due to the different energy scale and to emphasise the CdTe contributions. Figure taken from [1].

electronic interaction or bonding across the interface, similar to [112] where their stanene conduction band is delocalized throughout the slab.

Additionally, there is a potential induced avoided band crossing (AVB) between the α-Sn bands and the InSb valence band. This appears around -0.25 eV, however it is on the small scale of $\sim 1meV$. This is shown as function of layers in Figure 4.24. The explicit band crossing and data acquisition plots are shown in Figure 4.25. While the band crossing energy range is small, this could be an indication of the coupling strength between the two materials. However, further research would need to be undertaken to explore the relevance and validity of this, and this is also true of the wavefunction data.

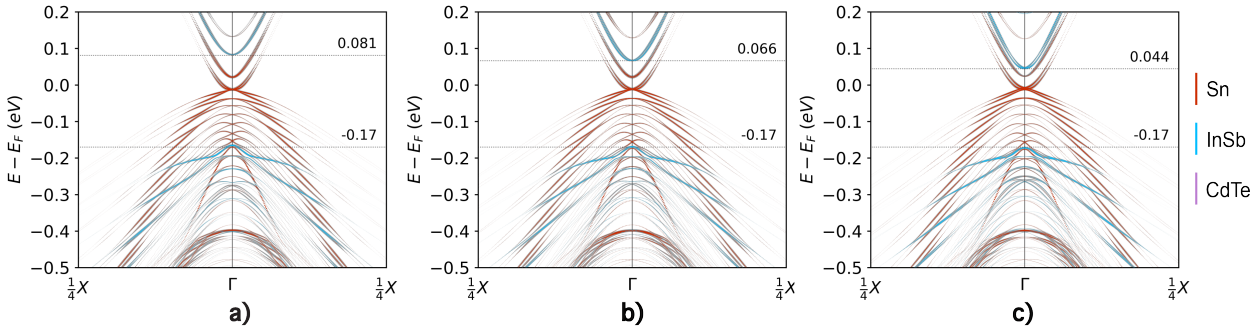

Figure 4.21: Band alignment of the tri-layer InSb/CdTe/α-Sn interface: Element projected band structures of with (a) 2 atomic layers, (b) 4 layers, and (e) 8 layers of CdTe. The bands originating from α-Sn, InSb, and CdTe are colored in red, light blue, and purple, respectively. Figure taken from [1].

4.7 New materials: InAs/CdSe,ZnTe/Al trilayers

This presents the introduction and the preliminary results of the ongoing work for next steps of the trilayer project. The goal is to investigate two different wide band gap semiconductors as barriers in the InAs/Al interface. InAs and Al are among the materials used to fabricate devices for Majorana search [82], where InAs is used as the the nanowire material and Al supplies the s-wave superconductivity. Here, we study a tri-layer system, in which InAs is separated from Al by a ZnTe or CdSe tunnel barrier. DFT can provide useful information on properties, such as the band offsets and the penetration depth of metal induced gap states (MIGS) into the semiconductor. The DFT+U approach, whereby a Hubbard U correction is added to certain atomic orbitals, provides a good balance between accuracy and computational cost for these materials. Previously, the results of DFT+U(BO) for InAs(001) and InAs(111) have been shown to be in good agreement with angle-resolved photoemission spectroscopy (ARPES) experiments [115].

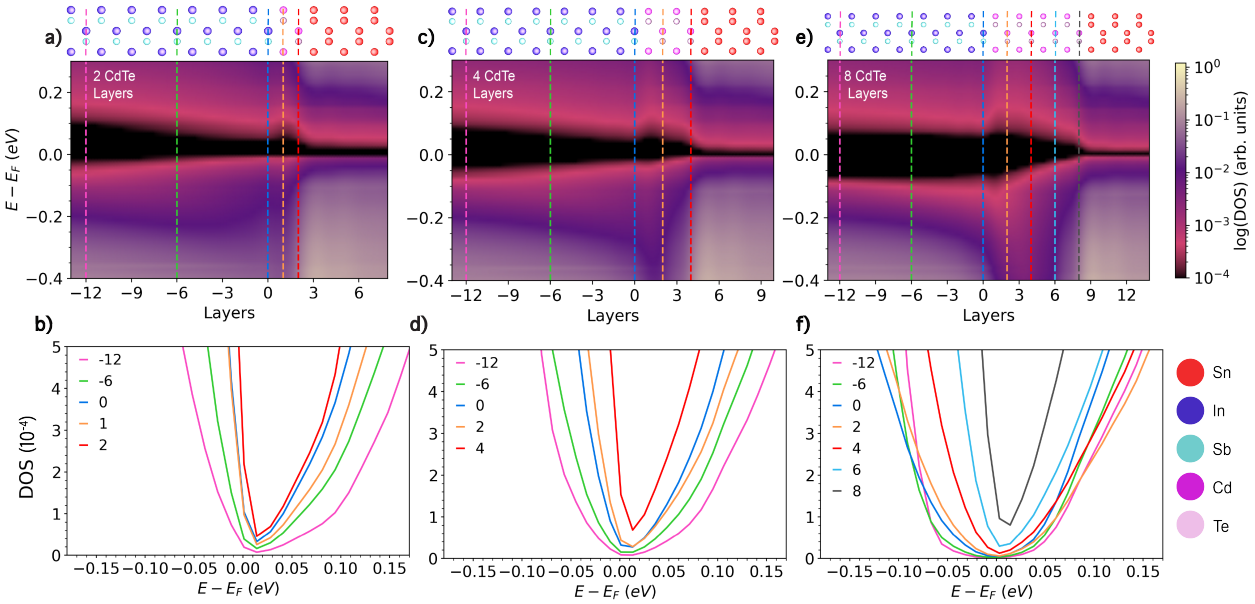

Figure 4.22: Electronic structure of InSb/CdTe/α-Sn tri-layer interfaces: Density of states as a function of distance from the interface for (a) 2, (c) 4 and (e) 8 CdTe barrier layers. The atomic layers are numbered based on distance from the interface, which is located at zero. Interface structures are illustrated on top. (b), (d), (f) Local density of states for selected layers, indicated by dashed lines in the same colors in panels (a), (c), and (e), respectively. Figure taken from [1].

4.7.1 Interface Model Construction

All semiconductor models were constructed with a (110) orientation using the experimental InAs lattice constant value of 6.0584 Å [163], assuming that the epitaxial films of Al, ZnTe and CdSe would conform to the substrate. Structural relaxation was performed at the interface for 4 layers of each of the substrate and film in each semiconductor/metal interface. Tri-layer slab models have structural relaxation only for the barrier-semiconductor/metal interface materials as it was not required to relax the semiconductor-semiconductor interfaces with the same lattice constant. The length of two monolayers of a (110) slab was 4.2840

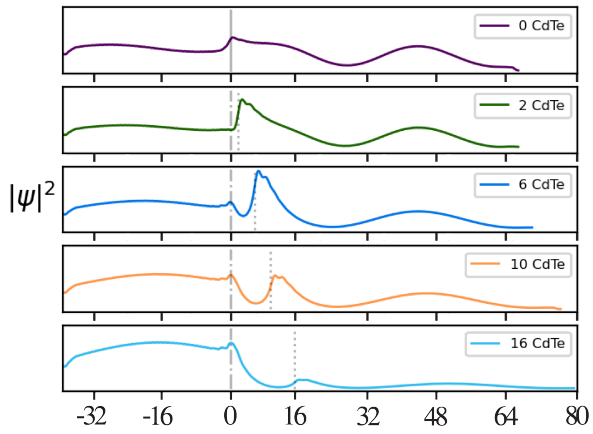

Figure 4.23: The 1D planar average (XY) along the slab of the band-decomposed positional charge (electron wavefunction) is shown. This is taken for a number of k-points from the InSb conduction band for different number of CdTe layers.

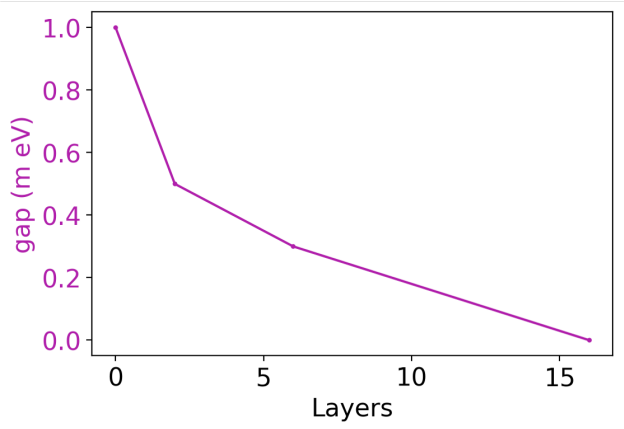

Figure 4.24: The magnitude of the avoided band crossing between the InSb valence band and α-Sn bands.

Å in the z-direction. A vacuum region of around 60 Å was added to each slab model in the z-direction to avoid spurious interactions between periodic replicas. The surfaces of all slab models were passivated by pseudo-hydrogen atoms such that there were no surface states from dangling bonds [131]. Passivation was not required for Al due its metallic properties.

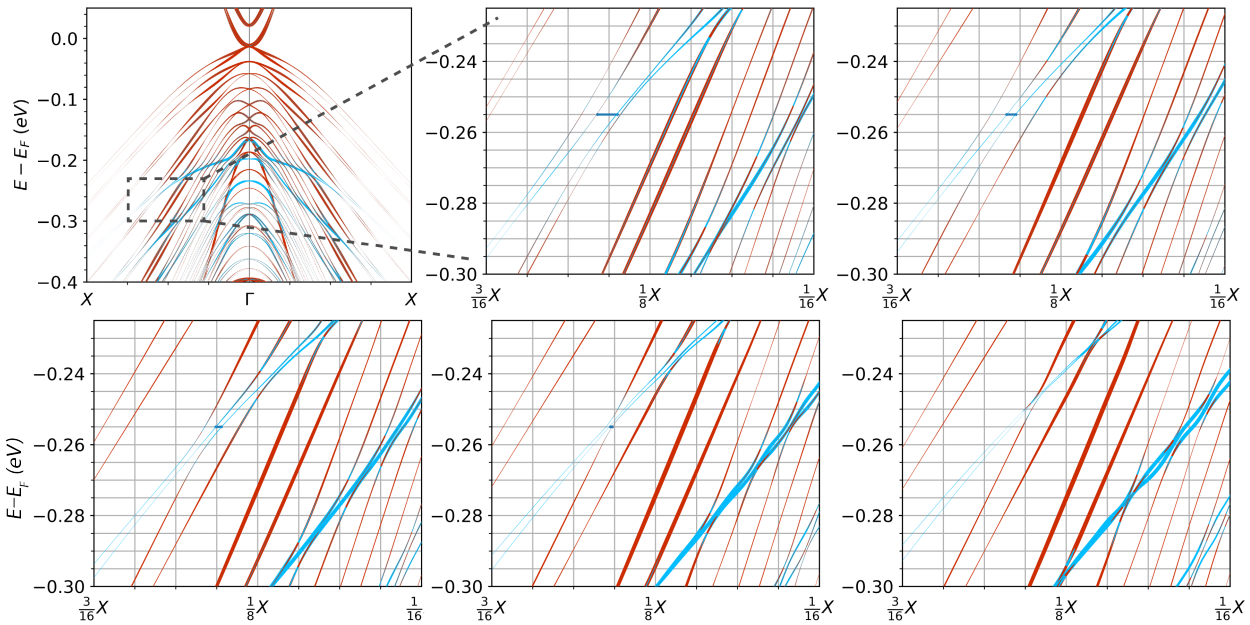

Figure 4.25: Electronic structure of InSb/CdTe/α-Sn tri-layer interfaces: Band structures zoomed in on the avoided band crossing with line indicating value. (a) and (b) are InSb/aSn interface. (c - top left) 2 CdTe layers. (d- bottom left) 6 CdTe layers/ (e) 10 CdTe layers (f) 16 CdTe layers

The InAs/(ZnTe,CdSe) interface structure has the metal of the III-V semiconductor bonded with the non-metal of the II-VI semiconductor, leading to In-Te,Se and As-Zn,Cd bonding, with each In interface atom connected to 3 As and 1 Te, Se.

When constructing such slab models, it is necessary to converge the number of layers to avoid quantum size effects and approach the bulk properties [111]. For InAs it has previously been shown that 50 monolayers are sufficiently converged [115]. Plots of the band gap vs. the number of atomic layers for CdSe(110) and ZnTe(110) slabs are provided. For metals, such as Al, there is no band gap and convergence can be found by plotting the density of states as a function of slab size. This is provided for Al.

4.8 Results and Discussion

4.8.1 Bayesian optimization of CdSe, ZnTe

The U values were machine learned using Bayesian optimization (BO) [107]. The reference HSE calculations were conducted for bulk ZnTe with a lattice parameter of 6.101 Å and compared to the results with the lattice constant of InAs, 6.0584 Å, which was used for interface models. It was verified that using the lattice constant of InAs does not have an appreciable effect on the electronic properties of ZnTe, as shown in Figure 4.26. The CdSe lattice constant is close enough to the InAs lattice constant, at 6.05 [164], such that 6.0584 Åwas used for CdSe throughout with no tests necessary. Additionally, no BO tests were conducted for Al as it is a metal.

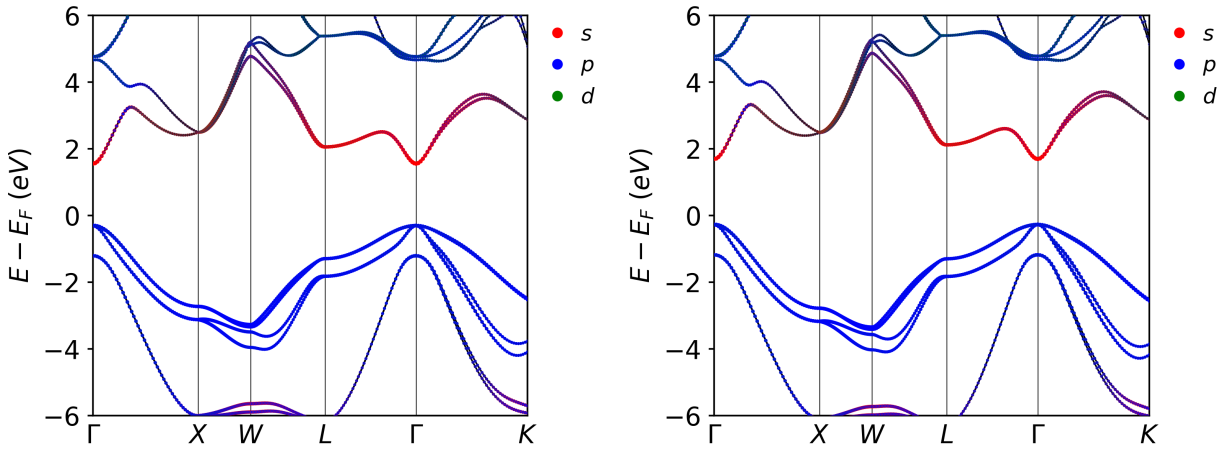

Figure 4.26: Comparison of the HSE band structures of ZnTe obtained with the lattice constant of (a) 6.101 Å of ZnTe and (b) 6.0584 Å of InAs. The band gaps are 1.86 eV and 1.96 eV respectively. The small difference in the lattice constant has no appreciable effect on the electronic properties.

The hyperparameters of our BO implementation are the coefficients α_1 and α_2, which assign different weights to the band gap vs. the band structure in the objective function, the number of valence and conduction bands used for the calculation of the objective function, N_b, and the parameter κ that controls the balance between exploration and exploitation

in the upper confidence bound acquisition function. For ZnTe and CdSe, a U correction was only applied to the Zn-d and Cd-d orbital. The hyperparameters used were $\kappa = 5$, $N_b = (5, 5)$, $\alpha_1 = 0.25$ and $\alpha_2 = 0.75$. The latter two parameters were chosen to assign more weight to the band shape rather than the band gap. This was because of over fitting when equal weight was given to α_1 and α_2, leading to the Zn and Cd value being outside the [-10,10] range. The Te-p and Se-p orbital U value always fell outside the range for any chosen hyperparameter set, thus no U value was applied to Te or Se. This is likely due to the large discrepancy of the HSE and PBE band gap for these materials.

For ZnTe this led to a U value of $U_{eff}^{Zn,d} = 9.4$. The gap of 1.48 eV is closer to experimental values of around 2.26 eV [164, 147] and the HSE value of 1.86 eV than previous calculations [147] and the PBE value of 1.07 eV. For CdSe this led to a U value of $U_{eff}^{Cd,d} = 8.3$. The gap of 0.95 eV is closer to experimental values of around 1.75 eV [164, 147] and the HSE value of 1.46 eV than previous calculations [147] and the PBE value of 0.51 eV. We note that there is still large discrepancies in PBE+U band gap values. For InAs the values of $U_{eff}^{In,p} = -0.5$ and $U_{eff}^{As,p} = -7.5$ were used, following Ref. [115, 107]. It has been shown that PBE+U(BO) produces a band structure in good agreement with ARPES for InAs [115].

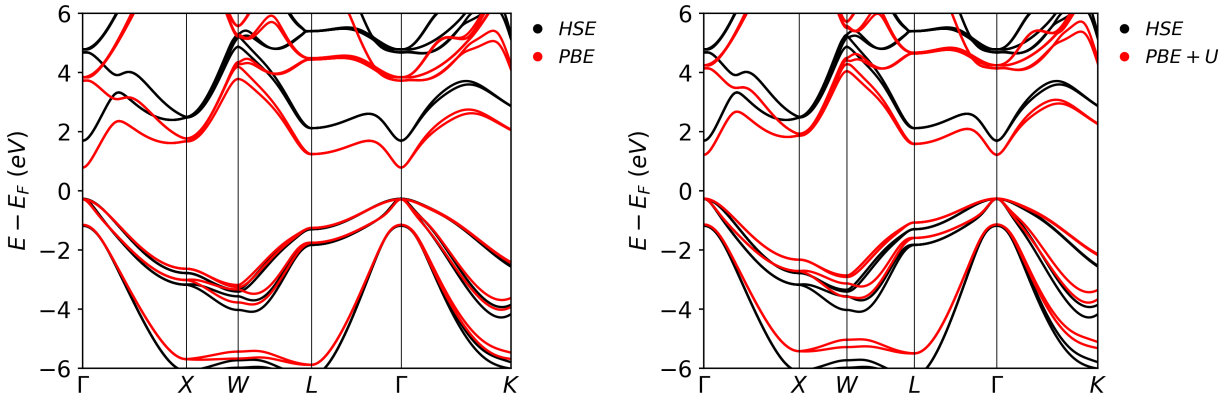

(a) (b)

Figure 4.27: Comparison of the HSE band structures of ZnTe obtained with the (a) PBE functional and (b) PBE+U functional. The band gaps of the PBE functionals are 1.07 eV and 1.48 eV respectively.

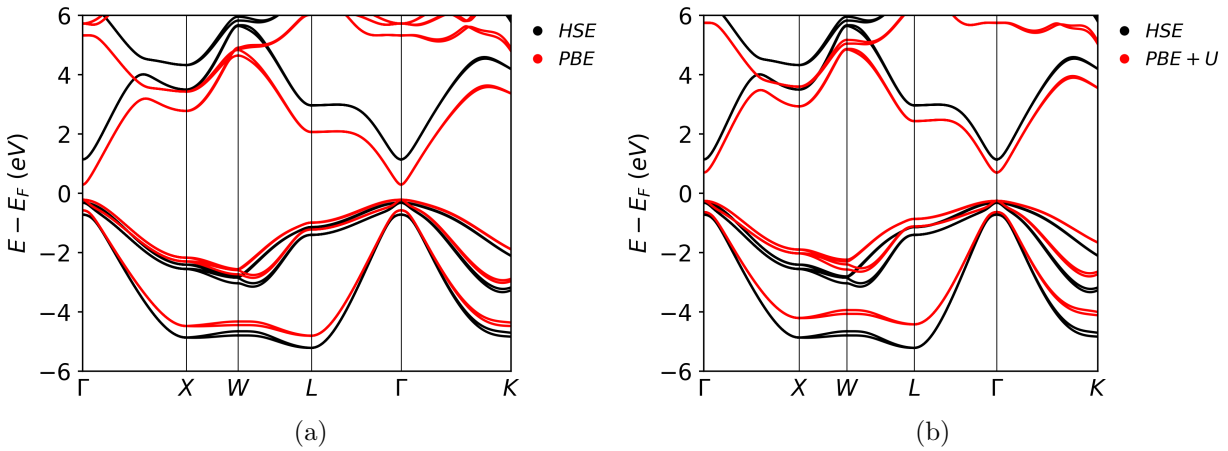

(a) (b)

Figure 4.28: Comparison of the HSE band structures of CdSe obtained with the (a) PBE functional and (b) PBE+U functional. The band gaps of the PBE functionals are 0.51 eV and 0.96 eV respectively.

4.8.2 Convergence of CdSe, ZnTe, Al

Plots of the Γ-point band gap vs. the number of monolayers for ZnTe(110) and CdSe(110) slabs, and density of states vs. the number of atomic layers for Al(110), are provided in Figs. 4.14 and 4.30 respectively. Following the convergence convention of [115], ZnTe and CdSe convergence is met for a given set of layers when the band-gap difference between the current iteration and the previous iteration is within 5×10^{-2} eV. For ZnTe(110), X layers are required to converge the band gap. For CdSe(110), (between 30 and 40, might need another calculations) layers are required. A PBE+U functional is used to demonstrate this convergence. For Al the qualitative shape of the middle layer of the local DOS in a slab is compared with the bulk DOS. For this, 10 was deemed appropriately converged for use in the trilayer setups. The bulk oriented structure was used for the unit cell in the bulk calculation because it's BZ is equivalent to the slab in the k_x and k_y directions and a single layer of the slab. Note that if the same number of layers is used in an interface model the gap value can change. The quantum size effect increases band gaps in smaller quantum systems which likely explains why many of the finite slab's band gaps, while deemed converged, will

be larger than the bulk system.

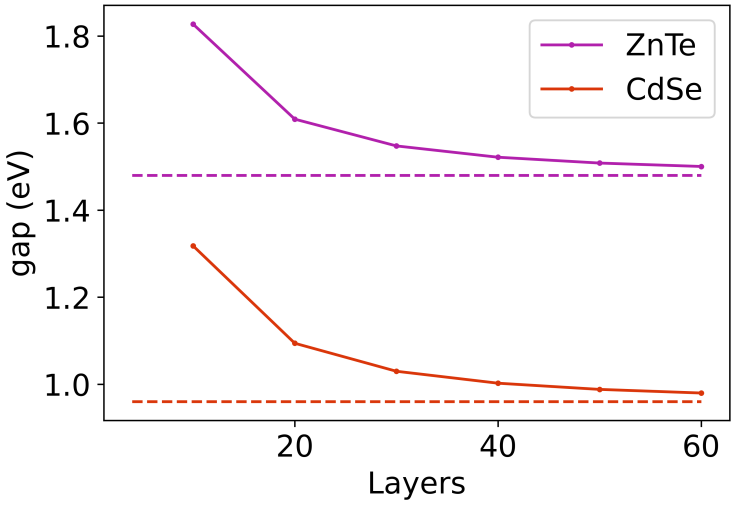

Figure 4.29: Slab convergence of ZnTe and CdTe: The Γ-point band gap of ZnTe(110) and CdTe(110), using the InAs lattice constant, as a function of number of mono-layers. Dashed lines denote the PBE+U(BO) bulk limit of 1.484 eV for ZnTe and 0.967 eV for CdSe.

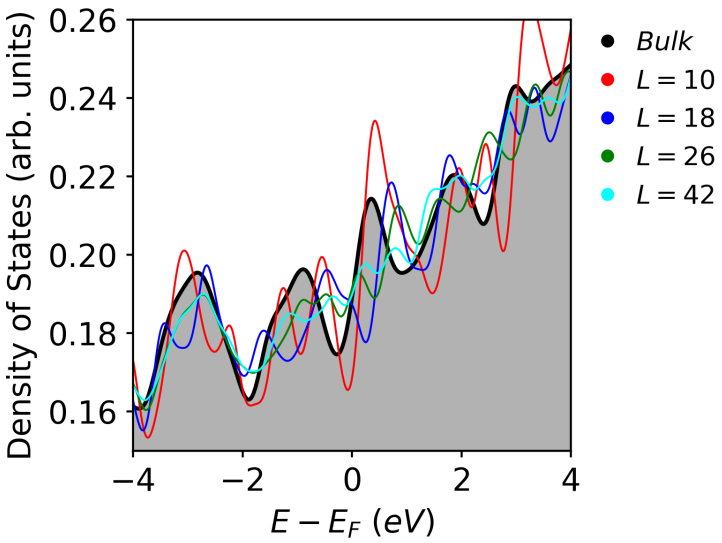

Figure 4.30: Thickness convergence of Al(110): The local density of states for the middle layer of the slab is given as a function of number of atomic layers. The thick black line denotes PBE+U(BO) bulk limit density of states. A Gaussian filter with $\sigma = 0.15$ was applied to the data to smooth out the density of states.

5.0 Integrating micromagnets and a hybrid nanowire model

5.1 Introduction

This project considered integrating micromagnetic simulations of nano to nano-scale magnets with a finite model of a semiconductor/ superconductor hybrid device model. The motivation is that one-dimensional topological superconductors host Majorana zero modes (MZMs) [18, 19]. They are promising for fault-tolerant quantum computing because of the predicted topological protection that they facilitate [62, 14]). While there has been considerable effort applied to identify MZMs in semiconductor nanowires [63, 165, 166], the evidence to date is not conclusive due to plausible alternative explanations such as non-topological Andreev Bound States [167, 64]. With new developments in materials research and experimental methods it is reasonable to expect that the present day challenges can be overcome [22]. We look beyond to explore how generating local magnetic fields using micromagnets can aid in the design of Majorana devices.

There have been several studies on incorporating magnetic materials to induce MZM in hybrid systems, though the questions asked were different. One class of ideas has focused on generating synthetic spin-orbit coupling in weak spin-orbit materials through nanomagnet patterning [168, 169, 170, 171, 172, 173, 174, 175]. Another class imagines shells of magnetic insulators on nanowires as a path to topological superconductivity through using exchange interactions [176, 177]. These results have sparked a debate about the feasibility and true origin of the observed signals [178, 179, 180, 149].

In this work we propose how stray magnetic fields can be used to realize basic two-Majorana building blocks, as well as four-Majorana fusion and six-Majorana T-junction braiding devices. Locally inducing magnetic fields avoids the reliance on a global magnetic field, and therefore fields can be oriented differently in the nanowire set-up opening up possibilities in measuring of complicated structures like T-junctions braiding devices and the ability to address and manipulate individual MZMs. In the basic building block (Dragonfly, Figure 5.1), four micromagnets are arranged around the nanowire such that field lines flow

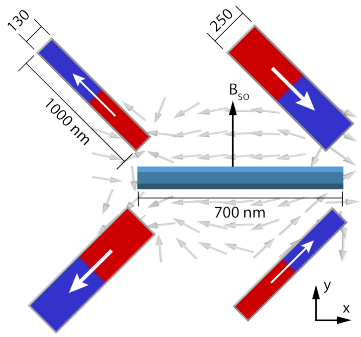

Figure 5.1: The Dragonfly setup with four micromagnets (blue/red) and an overlay of the magnetic field calculated with MuMax3 (gray arrows). The nanowire runs horizontally with the spin-orbit axis vertical, indicated by B_{so}. Figure taken from [6].

along the wire for 700 nm. Positions of the micromagnets are given in the SI. We find through modular micromagnetics and Schrödinger calculations that it should be possible to enter the topologically superconducting state and achieve partial Majorana separation. Higher stray fields, e.g. from stronger or thicker magnets, would make the regime more robust. We perform magnetic force microscopy on prototype micromagnet patterns and find that it is possible to realize the building block Dragonfly configurations, though arranging all micromagnets in a T-junction to the desired orientations will require very accurate control of switching fields.

The micromagnetic simulation software MuMax3 [181] is used to simulate realistic single domain-sized micromagnets, including hysteretic magnetization and stray fields. Hysteresis simulations are performed to obtain the required magnetization state. The parameters for cobalt were used, details can be found in section 5.4.2. The stray magnetic fields are integrated over an imagined hexagonal nanowire cross-section to obtain a one-dimensional field profile which can in principle extend to infinity. A hexagonal cross-section is chosen as that is how nanowires of the relevant materials, such as for InSb wires, grow. The field profile is used as input into a basic one-dimensional Majorana nanowire model [182] to obtain the energy spectrum and calculate Majorana wavefunctions γ_1 and γ_2. For this step a finite nanowire length is chosen over which the field profile can be utilized for a given set-up.

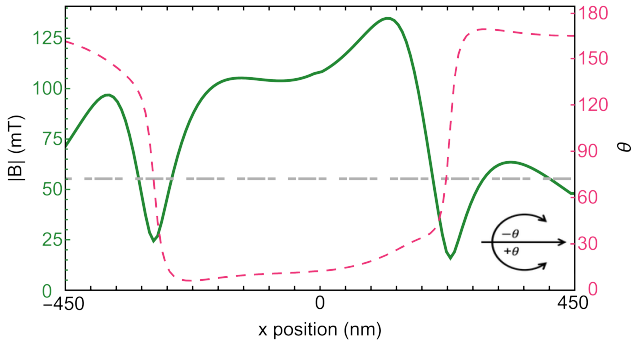

Figure 5.2: Magnetic field profile, as a function of position, of the four magnet Dragonfly setup shown in Fig 5.1. Solid line is field amplitude and dashed line is field angle θ relative to negative x-axis (inset). The field is averaged over a hexagonal cross-section of the nanowire with a characteristic dimension of 100 nm. In this Figure only, the reader is invited to imagine an infinitely long nanowire without ends and consider what field profile would be created along such a nanowire. The horizontal dashed gray line indicates a uniform field for entering the topological regime in an infinite nanowire. Figure taken from [6].

5.1.1 Majorana Model Used

The implemented one-dimensional semiconductor-superconductor hybrid model is given by a discretized Hamiltonian,

$$\begin{aligned}\hat{H} = \; & \textstyle\sum_n \left[(-\mu_n + \varepsilon_0)\left|n\right\rangle\left\langle n\right| \tau_z \otimes \sigma_0\right. \\ & +t\,(a)\left(\left|n+1\right\rangle\left\langle n\right| + H.c.\right)\tau_z \otimes \sigma_0 \\ & +i\alpha\,(a)\left(\left|n+1\right\rangle\left\langle n\right| - H.c.\right)\tau_z \otimes (\boldsymbol{\sigma} \times \mathbf{x}) \cdot \hat{\mathbf{z}} \\ & +\tau_z \otimes V_{z,n}\left(\cos\theta_n \sigma_x + \sin\theta_n \sigma_y\right)\left|n\right\rangle\left\langle n\right| \\ & \left. -\Delta_s \tau_x \otimes \sigma_x \left|n\right\rangle\left\langle n\right|\right],\end{aligned} \tag{29}$$

where

$$t\,(a) = \tfrac{\hbar^2}{2m^* a^2} \qquad \alpha\,(a) = \tfrac{\alpha_R}{2a} \ . \tag{30}$$

The meaning and values used for the parameters are as follows: n labels the lattice site, a is the lattice constant and $\varepsilon_0 = \cos(ka)$ with k the crystal momentum and this is an offset to bring the Fermi energy to the bottom of the band. To deal with nanowires in different directions $\mathbf{x}$ is a unit vector pointing along a particular section of nanowire. The s-wave superconducting pairing term is $\Delta_s = 0.08$ meV, the Rashba spin orbit coupling term $\alpha_R = 0.2$ eVÅ, effective electron mass $m^* = 0.04 m_e$, and $g_{eff} = 50$ such as in InSb wires. Lastly, the Zeeman energy is $V_{z,n} = \frac{1}{2} g_{eff} \mu_B B_n$, with the magnetic field, B_n, and relative angle of the field to the x-axis, θ_n, being both site dependent and in general have a complicated structure due to the use of the micromagnets, a notable difference to many other works. The simulated magnetic field from MuMax3 is inputted into the 1D nanowire-superconductor model via $V_{z,n}$, and the spectrum and eigenstates calculated via exact diagonalization. The effects of the non-uniform structure of the Zeeman energy were utilized and investigated by constructing longer devices with many micromagnets, and a T-junction set-up where perpendicular wires had different field directions.

5.1.2 Interpreting Majorana results

To investigate viability of the proposed devices, the MZMs signatures of state polarization and zero-energy pinning are required. A single electronic Majorana state, with energy E_0, can be written in terms of the two Majorana wavefunctions via $\gamma_1 = c + c^\dagger$ and $\gamma_2 = -i\left(c - c^\dagger\right)$ and, due to the topological nature of MZMs, polarization of the two MZM will be apparent, seen as the localisation of two Majoranas at opposite ends of a single topological region of nanowire. In short length systems the MZMs can be overlapping, and also could have a complicated structure due to the variation of the magnetic field or nanowire length. The lowest eigenstates of the system are single quantum states that are pairs of MZMs. The first energy/excited state, denoted E_1 if there is a single pair of MZMs present, should have weight predominately in the bulk, with little overlap with the MZMs. The second signature is the near-zero energy of the MZM state, with good energy separation from the first energy

state.

5.2 Numerical Results

The setup presented in Figure 5.1 is our basic configuration. The four micromagnets, that resemble a dragonfly, induce field lines along the nanowire, coming in at the right end, and flowing out of the left end. The field does not deviate by more than 30° over a 700 nm long nanowire segment, see Figure 5.2, and maintains a relatively uniform amplitude. Furthermore, for a given hexagonal cross-section the standard deviation is of order 5% of the mean which justifies the procedure of producing a one-dimensional field profile by averaging over the cross-section, at least for the central segment of the nanowire length, see Figure 5.17. The nearly parallel field is required for MZMs formation, since such field is mostly orthogonal to the effective spin-orbit field, B_{so} [19, 18, 183, 184], hence why we use angle relative to the nanowire when presenting the stray field profile. Four, rather than two, magnets are required to cancel y-fields and enhance x-fields, with no external field required. Micromagnets placed parallel to the nanowire, e.g. as a shell around the nanowire, produce largely y-fields that are highly non-uniform, concentrated outside the poles of the magnets (see Figure 5.15 [176]).

The micromagnet widths are different to ensure different switching fields and to aid in the preparation of a desired mutual magnetization pattern [185], which has the goal of supplying a strong , uniform field that points in the desired direction to achieve the topological state in the nanowrie. The magnets are rotated at 45 degrees to aid magnetization through the hysteresis simulation. Magnets on opposite sides of the nanowire are perpendicular, and therefore the external field used for magnetization is also perpendicular for the pairs of magnets. The out of plane direction (z-component) of the simulated field is insignificant due to the symmetry of the micromagnet arrangement (see supplementary information 5.13).

Given the simulated magnetic field profile along the 700 nm long nanowire, there is clear Majorana polarization of the two MZMs, γ_1 and γ_2, shown in Figure 5.3. Though we assume a relatively low magnetic field for the topological transition, 50 mT. The two

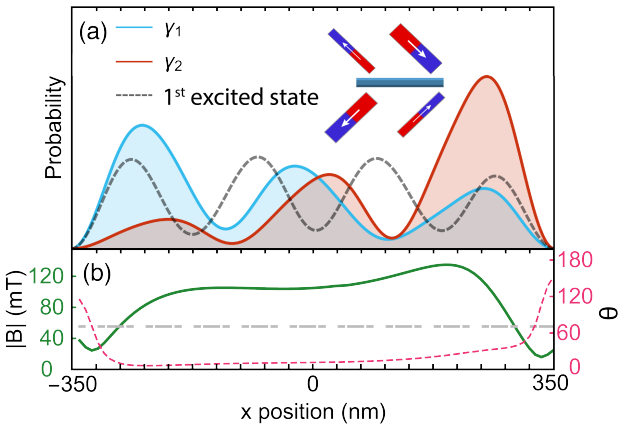

Figure 5.3: (a) Probability distributions for two Majorana wavefunctions γ_1 and γ_2. The first excited state (dashed line) is a bulk nanowire state. (b) Magnetic field profile reproduced from Figure 5.2 over a smaller range. Hard boundaries are introduced at ± 350 nm to calculate the wavefunctions. There is no applied external field. Figure taken from [6].

Majorana wavefunctions are highly overlapping. The lowest (partially separated Majorana) and the first excited energy levels have energies $E_0/\Delta = 0.28$ and $E_1/\Delta = 0.82$, where Δ is the superconducting gap. We note that a small global external field can be applied to boost Zeeman energy.

The next device (inset Figure 5.4) combines two Dragonfly set-ups and an additional vertical magnet (dashed border), elongating the topological nanowire region. The concept can be repeated multiple times to further extend Majorana separation or create multiple pairs of MZM, for instance in Majorana fusion experiments [14]. The right Dragonfly unit is reflected: this means magnetic fields point opposite in the left and right nanowire segments. Naively, MZM generated by opposite magnetic fields cannot couple as they possess opposite spin [186]. Nevertheless, left and right MZM form a pair due to field rotation provided by the central magnet. Using the same topological criterion we now find a more substantial MZM polarization of the ground state E_0 (red/blue) with more noticeable tailing off of the wavefunctions. This is because the total length of the device is increased and two MZMs in the middle (dashed line in Figure 5.4a) hybridize and reduce their overlap with end MZMs.

Application of an external field (10's of mT) in the positive y-direction in this case aligns the total field closer with the nanowire. Supplementary information presents other versions of the double Dragonfly.

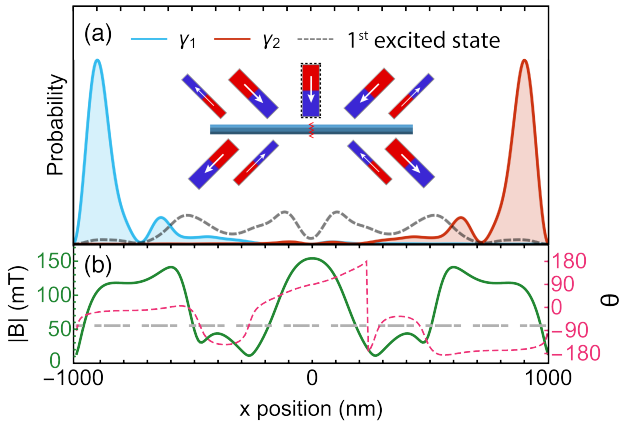

Figure 5.4: (a) Probability distributions of two lowest energy states for double Dragonfly setup with gate open (shown in inset). MZM (red/blue) with $E_0/\Delta = 5.1 \times 10^{-4}$. The first excited state (grey dashed) with $E_1/\Delta = 1.6 \times 10^{-1}$. External field of 40mT is applied in positive y-direction. Inset: two dragonfly configurations, with zigzag indicating an electrostatic gate capable of dividing the nanowire in two parts. (b) Magnetic field profile along the wire, showing amplitude (solid) and angle (dashed). Figure taken from [6].

The T-junction set-up, shown in Figure 5.5, explores how micromagnets could be used to realize a MZM braiding setup. The horizontal left and right arm sections are made by chaining together Dragonflies, and a perpendicular leg section in the middle has a micromagnetic configuration similar to a single Dragonfly. Adding a second dragonfly to the leg does not substantially improve MZM separation due to an external field in the y-direction (see supplementary information). This allows the field to be parallel to the nanowire in perpendicular sections of the wire, something that is not possible in a uniform external field.

The simulated stray field (supplementary Figure 5.14a), with an additional y-direction external magnetic field of 40 mT, allowed MZMs to separate or couple across any two sections of the T-junction nanowire, seen in Figure 5.6, where each arm of the junction has an electrostatic gate, G_1, G_2 and G_3, to control which sections are connected and disconnected.

With all three gates pinching-off the nanowire we see that the three lowest energy ground states are pairs of MZMs (red, green and blue) confined to separate wire segments (Figure 5.6a). Small differences in energy of the MZM state can be attributed to the magnets not being perfectly magnetized and that the magnet configurations at the ends of the two arms are not the same to keep the field pointing the same direction along each arm. With gate G_3 cutting off the perpendicular leg section, Figure 5.6b, the lowest energy state (red) is localized at the ends of the top wire, demonstrating that the micromagnets allow this to act as a single, long topological superconductor. The second lowest energy state of the entire system is MZMs isolated in the perpendicular nanowire (blue), and the third lowest state (green) has weight mostly at the junction, representing two nearby MZM. We note that the fourth energy state is larger in energy with more weight in the bulk of the nanowire, suggesting it is not a partially hybridized MZM pair.

By pinching off gates G_1 or G_2, Figs. 5.6c and 5.6d, we cut off either the left or the right section of nanowire. MZM states couple and decouple across the T-junction, In panel (d) the blue wavefunction extends over entire left and leg segments of the T-junction, making the red wavefunction appear purple. These results suggest that a repeated Dragonfly setup could be used to realize a braiding setup, in principle, although with relatively complex micromagnet configurations.

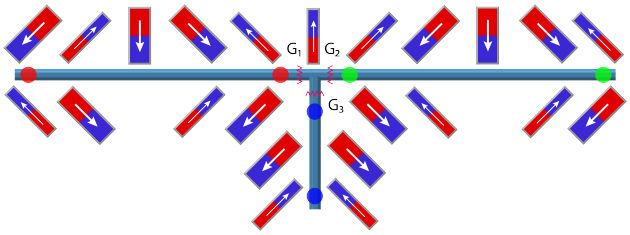

Figure 5.5: T-Junction setup. The top two sections of nanowire are 5000 nm in length in total and the perpendicular section is 1100 nm. Zigzag lines indicate electrostatic gates (voltage gates in an experimental setup). Circles indicate desired positions of 6 MZM with all gates on. Figure taken from [6].

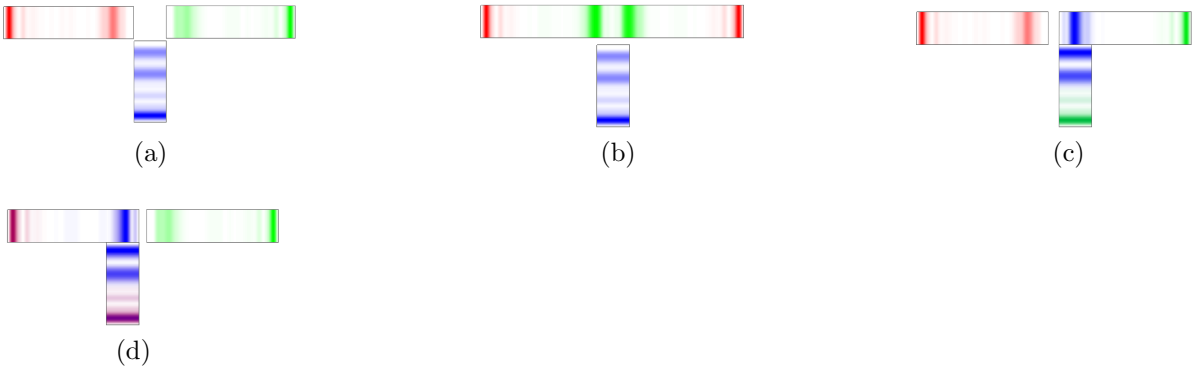

Figure 5.6: Probability distributions (color) of the ground, second and third lowest energy with (a) all gates (b) gate G_3, (b) gate G_1, (c) gate G_2 activated. Colors chosen so that red wavefunction always has a weight on the left end. The energies for the pairs of Majorana states are given in the table below. Figure taken from [6].

Energies of setup $/\Delta$	(a)	(b)	(c)	(d)
E_0	1.6×10^{-3}	1.6×10^{-5}	3.5×10^{-4}	7.2×10^{-4}
E_1	2.3×10^{-3}	9.4×10^{-3}	1.6×10^{-3}	2.3×10^{-3}
E_2	9.4×10^{-3}	4.2×10^{-2}	4.3×10^{-3}	3.1×10^{-3}
E_3 (not shown)	1.5×10^{-1}	1.1×10^{-1}	1.3×10^{-1}	1.2×10^{-1}

5.3 Magnetic Force Microscopy

We take the first step to evaluate these device concepts experimentally, by studying magnetization patterns of micromagnets. Ferromagnetic micro-strips are fabricated in a design that represents a simplified version of the braiding T-junction setup (Figure 5.7). The design features three Dragonflies arranged in a T with the same dimensions as Figure 5.1 but a shorter distance between magnets, and an extra vertical magnet. The strips are written by electron beam lithography (EBL) and the metal is deposited by electron beam evaporation from a CoFeB source (atomic ratio 30/55/15 before deposition) to a thickness

of 20 nm. This is thinner than typical nanowires, and was done to reduce magnetic signal and permit higher resolution imaging. It is believed that the final strips are mostly CoFe without boron [187].

Magnetic force microscopy (MFM) and atomic force microscopy (AFM) are performed on triple Dragonflies (Figure 5.7). An attempt is made to take advantage of hysteretic magnetization and prepare magnets preferentially in the desired Dragonfly configuration so that stray magnetic fields are along the imaginary nanowire in between the micromagnets. The range of field where wide and narrow micromagnets are antiparallel is determined from separate SQUID measurements to be between 15 and 20 mT, in agreement with Ref. [185], when reduced CoFe thickness is accounted for.

Twenty-four T-junctions with three Dragonflies each are imaged, and six of 72 total Dragonflies are magnetized as required for MZM generation. Figure 5.7(b) shows one such section with the magnetization marked by arrows (supplementary Figure 5.18 shows all data). The occurrence of four micromagnets in the right orientation is consistent with random magnetization. While in our MuMax3 simulations it is possible to run through the hysteretic magnetization cycle and prepare micromagnets in the desired configuration, experimental variations in switching fields highlight a challenge. Optimized micromagnet fabrication will yield sharper switching and more reproducible switching fields in the future.

5.4 Conclusions, limitations

We consider device concepts in which micromagnets generate stray field patterns suitable for the generation of Majorana zero modes. Our approach assumes micromagnets placed next to semiconductor nanowires that possess strong spin-orbit coupling, and are coated with superconducting shells. The requirements on the stray magnetic fields are that they are of sufficient strength to drive a topological transition, and should be oriented as much as possible along the nanowire. The building block of our magnetic design is a Dragonfly configuration in which four micromagnets are magnetized such that the magnetic field lines flow out of one pair of micromagnets, along the nanowire, and into the other pair (Figure

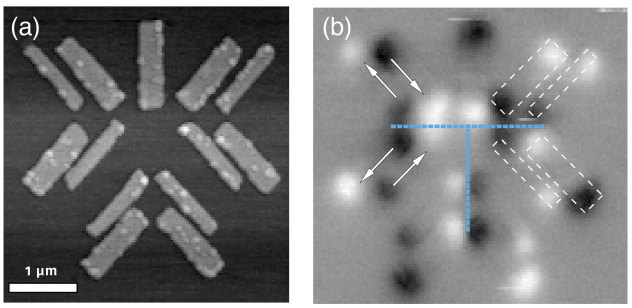

Figure 5.7: (a) Atomic force microscopy (AFM) of a T-junction setup with three Dragonfly magnet configurations. Magnetic film thickness is 20 nm. (b) Magnetic force microscopy (MFM) data on a different T-Junction of the same design. Arrows indicate magnetization direction, white dashed lines are example of magnet dimensions. Blue dashed line is where the Majorana nanowire is envisioned. The magnetic history was a magnetizing field from 100 mT to -16 mT to 0 mT applied at 45 degree direction, then 100 mT to -16 mT to 0 mT at 135 degrees. Figure taken from [6].

5.1). By repeating the Dragonfly pattern along the nanowire, we can extend the length of the topological segment with addition of coupling magnets. The approach can also be applied to T-junctions required for Majorana braiding experiments, in which case magnetic field turns into the T-junction leg that is perpendicular to the junction top.

Among the limitations is the still limited strength of stray fields from micromagnets. In previous experiments the typical stray fields are in the range of tens of milliTesla [185]. This is in principle sufficient to enter the topological regime in large g-factor semiconductor such as InSb nanowires, but it limits the parameter space for Majorana separation and manipulation. Stronger magnetic materials, or thicker micromagnets can help. Additionally, the Meissner effect from the superconducting layer on top of the nanowires was not taken into account, however the effect on the magnetic field is assumed to be small as magnetic fields penetrate through such thin superconducting films. Disorder in real nanowire devices will put limitations on the achievable MZM separation distance.

A challenge that became apparent from magnetic imaging of prototype structures is how to prepare all micromagnets in the appropriate relative magnetic orientation. This becomes

harder when the configurations increase in complexity such as for T-junctions. Though basic two-Majorana experiments should be possible already now, in the future better control over coercive fields, further pattern optimization, and direct magnetic writing can be deployed.

Among future ideas, a promising path is using a Y-junction instead of a T-junction [72], an approach that may require fewer micromagnets as some can be shared between the branches. Rather than gate-controlled MZM coupling, magnetic field mediated coupling can be investigated, by flipping micromagnets at the junctions. The implementation of the Poisson-Schrödinger equation to model MZM in the 3D geometry of a single nanowire could be integrated with 3D stray field profiles rather than simplified one-dimensional profiles integrated over the nanowire cross-section, which will provide information on the effect of the non-uniformity of the field combined with the effect of electrostatic confinement and disorder.

To summarize, nanoscale control over the field magnitude and direction is advantageous, particularly for advanced geometries where some nanowire segments may run perpendicular to others. Micromagnets could offer novel ways to control Majorana-based devices, for instance by switching magnetization in order to reposition or couple MZMs.

Acknowledgements and funding. We thank S. Meynell and D. Yang for helpful discussions. Work in Pittsburgh (numerics and nanofabrication) supported by the Department of Energy DE-SC-0019274. A.B.J. acknowledges the support of the NSF Quantum Foundry through Q-AMASE-i program award DMR-1906325.

Code and data availability. Example MuMax3 scripts, numerical results data, Majorana simulation Mathematica notebooks are available on Zenodo [7], or available on GitHub via https://github.com/frolovgroup.

Author Contributions. M.J. and E.J. performed MuMax3 simulations. M.J., E.J. and J.S. performed Majorana simulations. Y.J. fabricated micromagnet devices. W.W. and A.B.J. performed MFM/AFM imaging. M.J. and S.F. wrote the manuscript with input from co-authors.

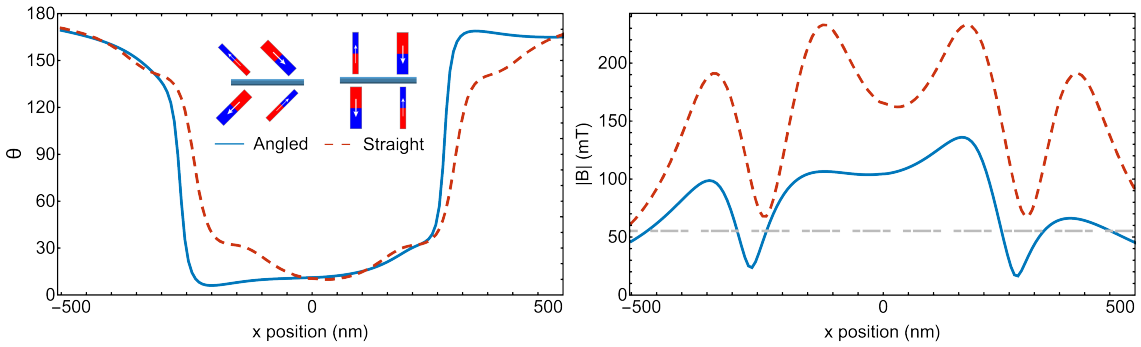

(a) (b)

Figure 5.8: This compares the a rotated and un-rotated Dragonfly configuration. The solid line is the rotated set-up and the dashed line is the straight set-up. Rotating the magnets makes them easier to magnetize through hysteresis. This figure is for a 1000 nm nanowire segment. Figure taken from [6].

5.4.1 Further Reading

For basic introductory review of Majorana nanowire topic consider reading [21]. A perspective giving an explanation on Rashba spin-orbit coupling one can read [25]. Other relevant work on nanowires that deal with areas such as surface effects, effects of the contacts, electric field considerations, and try to comprehensively implement the model [188, 182]. For work that utilizes the Poisson Schrödinger equation to model MZMs in the 3D geometry of a single nanowire [182, 188, 80], where the use of 3D field profiles could give a batter picture of systems in future studies. Further work on implementing micromagnets for use in Majorana based devices [185]. There are several different proposed braiding schemes using nanowire-network junction devices [182, 16], with options such as using local chemical potential changes [72] or flux gates [189].

5.4.2 Micromagnetic Simulation Details

[181] is a GPU-accelerated micromagnetic simulation program that uses finite difference discretization methods, accurate sized magnetic domains within a single magnet for micro-

to nano- scale system simulations, and was implemented to obtain the magnetic field used in the hybrid nanowire model. The micromagnetic structure is first constructed for each set-up in MuMax3, the requisite magnetization states achieved through hysteresis, if possible, and then the stray field is averaged over the hexagonal nanowire cross-section (such as for InSb wires) with diagonal width of 100 nm, typical of experiments. Upon averaging, an effective one-dimensional magnetic field profile is obtained. Note that the magnetic field can be in principle calculated for an arbitrary coordinate, meaning that the MuMax calculation does not need to encode a fixed nanowire length. This one-dimensional field profile is then used in the Majorana model to calculate several lowest energy energies and wavefunctions. At this step a finite nanowire length is chosen. The code used for the calculations can be found on Zenodo [7].

To obtain the required magnetization state through hysteresis the micromagnets start with many randomly orientated domains and then an external magnetizing field is applied and the system was relaxed at regular time intervals while ramping up and down the field. It was found that angling the micromagnets at 45 degrees made obtaining the desired magnetization directions easier, as magnets on the opposite side of the nanowires were then perpendicular to each other. This allows the micromagnets to be closer together, however angling the magnets reduces the magnetic field, see Figure 5.8, so these effects have to be balanced to obtain the strongest magnetic field possible. The hysteresis process takes into account the material of magnets, which include saturation magnetization, anisotropy constants and exchange stiffness. One limitation present is the material of the nanowire, leads and other components were not taken into account in the simulation, but the main magnetic effects are presumed to come from the magnets themselves.

of Cobalt are used due to several factors, first is that the constructed micromagnet devices are thought to be mainly composed of CoFe. Additionally, Cobalt is a common material used in the fabrication of micromagnets, and it allows for a relatively high saturation magnetization, and thus a stronger stray field, while also allowing for a reasonable coercive field due to Cobalt's exchange stiffness and cubic anisotropy constant. This allows for an appropriate demagnetization/stray field in the nanowire region, while also reliably obtaining the magnetization direction required for the setup, and additionally allowing for a small

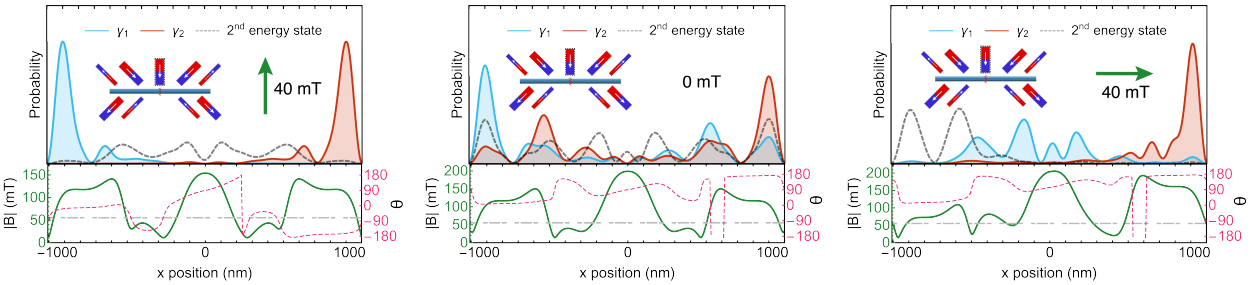

Figure 5.9: Comparing the double Dragonfly with different external fields. (a) 40 mT in the positive y direction (b) no field and (c) 40 mT in the positive x direction. Figure taken from [6].

external field to be applied without accidentally flipping the magnets. The parameters used are a saturation magnetisation of 1.44×10^6 A/m, exchange stiffness 3.0×10^{-11} J/m, anisotropy constant K_1 4.5×10^5, anisotropy constant K_2 1.5×10^5 and a Landau-Lifshitz damping constant of 0.01.

Micromagnets of two different widths are reliable and sufficient enough for hysteresis and field production purposes, the dimensions of all magnets in this work are either that of the thin magnet, with dimensions $130 \times 1000 \times 100$ nm, or the thick magnet with dimensions $250 \times 1000 \times 100$ nm, as the different sized magnets flip at different coercive fields. The nanowire used in the MuMax simulations has a hexagonal cross-section with a long diagonal length of 100 nm.

5.4.3 Supplementary Results

5.4.3.1 Dragonfly

For the Dragonfly setup, the positions and dimensions of the set-up are as follows. The micromagnets used were two different widths, with thin magnet dimensions $130 \times 1000 \times 100$ nm or thick magnet with dimensions $250 \times 1000 \times 100$ nm, so the different sized magnets flip at different coercive fields. The magnets are rotated at 45 degrees to aid the reliability of

magnetization directions. The nanowire has a hexagonal cross-section, with a long diagonal length of 100 nm, and length of 700 nm so it spanned the region of parallel field from the magnets. The centers of the micromagnets are displaced from the middle of the nanowire to the left and right by 250 nm, with magnets of the different widths opposite each other. The y-displacement of the micromagnets from the nanowire is chosen such that the nearest corner of each magnet is 40 nm from the nanowire. These positions are one workable configuration, and changing the positions, dimensions or magnet material parameters will change the magnetic field profile, but this is the optimal set-up found.

Due to the magnetic field being calculated through simulated hysteresis the magnets are not perfect single domains, in particular at the edges of the micromagnets the boundary causes non-uniformities. However, the net effect of this is small, but it explains why some of the state's energies and positions are not perfectly symmetric. Lastly, we note the difficulty to obtain a field larger than ~ 150 mT in the current set-up, additionally the superconducting gap is not necessarily fixed experimentally, which will change the field requirements.

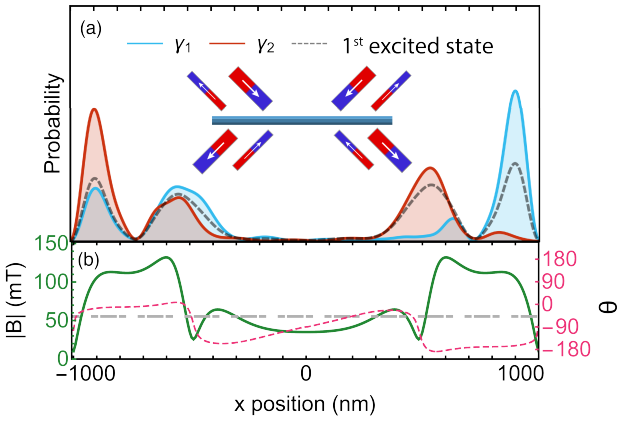

Figure 5.10: (a) Probability distributions for two lowest energy states, this system shows two overlapping and degenerate states with no clear Majorana polarization and no higher energy state being gapped out. The energies of both states $E_1/\Delta = 3.9 \times 10^{-2}$ and $E_2/\Delta = 4.6 \times 10^{-2}$. (b) Field profile along wire. External field is 40mT in positive y-direction. Figure taken from [6].

5.4.3.2 Double Dragonfly without extra magnet

This double Dragonfly device (inset Figure 5.10(a)), is different from the one shown in the main text as it only combines two individual Dragonfly set-ups (without the middle 9th magnet). The magnetic field has a large region of low magnitude field in the middle section, see bottom panel of Figure 5.10(b), and there is an external field of 40mT applied in positive y-direction. The eigenstate profiles and energy spectrum suggest there are two pairs of uncoupled MZM on each side of the wire.

5.4.3.3 Double Dragonfly with extra Magnet

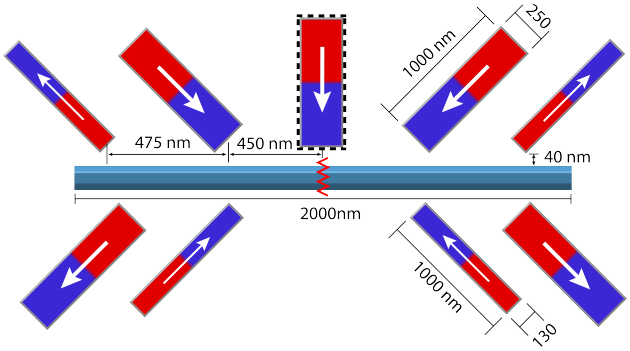

Figure 5.11: The double Dragonfly setup with the magnet in the middle and a potential gate, dimensions given. Toggling this gate allows the left and right side of the wire to be coupled or uncoupled. Figure taken from [6].

Full dimensions of the double Dragonfly with the extra magnet are given in Figure 5.11. A gate is turned on in the middle region of the nanowire (red zig-zag line), uncoupling the ends of the nanowire and causing two pairs of MZMs to appear. This is implemented as a large potential barrier spanning around 10 sites, and would be implemented experimentally by pinching off the nanowire. These two pairs of MZMs live in the parallel region of field, similar to the single Dragonfly set-up, with energies of $E_0/\Delta = 3.1 \times 10^{-2}$ and $E_1/\Delta = 3.2 \times 10^{-2}$, and the first excited state at a larger energy of $E_2/\Delta = 8.9 \times 10^{-1}$.

The states in the double Dragonfly device under different external magnetic fields are shown in 5.9. Panel (a) is the same figure in the main text with an external field in the

y-direction which aids coupling. Compare to panel (b) without the external field where the MZM states are less clear with less polarization and larger energies. Panel (c) shows how applying a Bx field with the double Dragonfly set-up gives preference to one side over the other. This is what would happen if a double Dragonfly was used in the leg section of the T-junction.

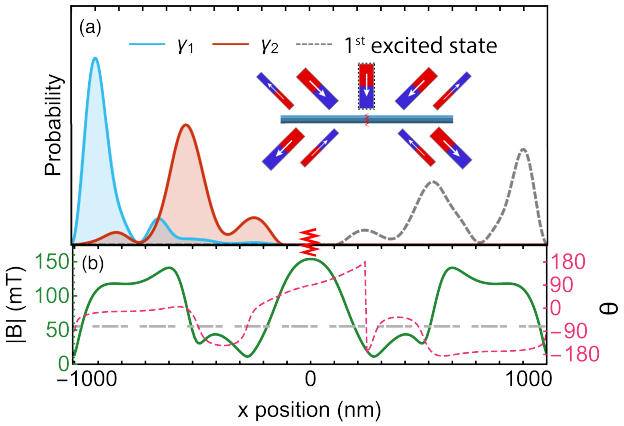

Figure 5.12: (a) Probability distributions for two lowest energy states for double Dragonfly setup with the 9th magnet and the gate closed (inset). The probability distributions shows two separate pairs of MZMs in each section of the wire, the left is shown in the Majorana basis with energy $E_1/\Delta = 3.1 \times 10^{-2}$ (red and cyan), the other pair in the right section is in the electronic state basis with energy $E_2/\Delta = 3.1 \times 10^{-2}$ (black- dashed line). The third state is well separated at $E_3/\Delta = 8.9 \times 10^{-1}$. (b) Field profile along wire. External field is 40mT in positive y-direction. Figure taken from [6].

5.4.3.4 T-junction magnetic fields

The magnetic field profile input into the nanowire model was made by taking the simulated central three single Dragonfly set-ups (with the middle magnet) from MuMax3, and then the top field profile was elongated by attaching two flipped copies of the top field profile and and connecting these on the ends. This had to done as it wasn't possible to accurately simulate all the magnets in the final T-junction set-up, however due to the modular nature of the Dragonfly set-ups this is reasonable. The magnetic field in the top nanowire rotates

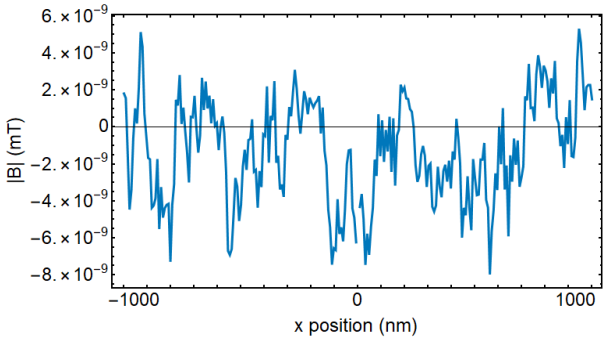

Figure 5.13: B_z field component along the wire for the double Dragonfly with the middle ninth magnet. The B_z data for other set-ups available on Zenodo [7]. Figure taken from [6].

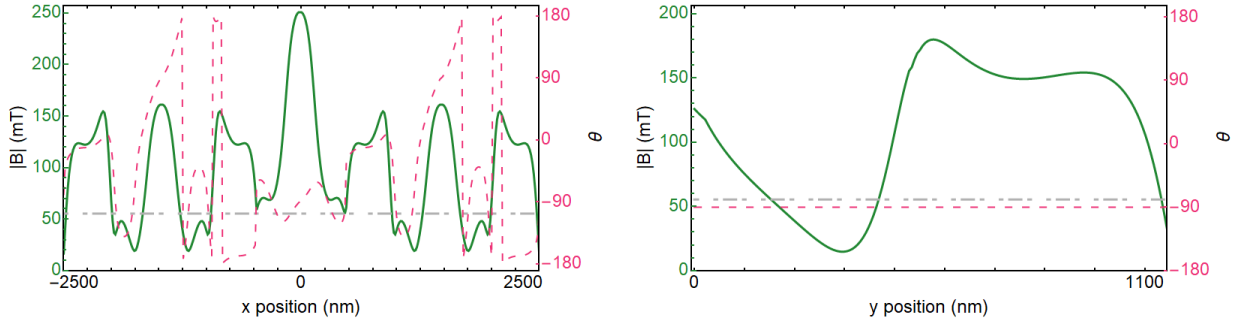

(a) (b)

Figure 5.14: (a) Magnetic field of top wire for T-Junction. (b) Magnetic field in the T-Junction leg (vertical segment of nanowire). There is an external field of 40mT applied in positive y-direction. Figure taken from [6].

smoothly across the length of the nanowire (see Figure 5.14a), and the whole nanowire is one, mostly continuous topological region. The magnetic field in the perpendicular section of nanowire is similar to that of the single Dragonfly set-up, with a parallel region of around 700 nm, note this is very uniformly pointing up (positive y) due to magnets on opposite sides of the nanowire having the same widths, see Figure 5.14b. The applied external magnetic field, of 40 mT, was added in the positive y-direction to facilitate maximum coupling.

5.4.3.5 Field uniformity

To show the uniformity of the field near and inside the nanowire the following is considered, with all data on Zenodo. The single micromagnet in Figure 5.15 shows the field is only highly non-uniform very near the micromagnet poles, and drops off rapidly away from the micromagnet. Note that the field is very weak at the magnet sides, hence why a multiple magnet design is required to obtain strong enough stray fields. The most inhomogeneous region is therefore where the magnets come closest to the nanowire Figure 5.16 which shows the field magnitude in the area between two micromagnets in a 5 nm thick layer. In the region of the nanowire (marked by red lines) the field variation is significant near the tips of the magnets, but the field is much more uniform away from the tips on the left. Figure 5.17 plots the standard deviation of the field magnitude over the nanowire cross-section, note this is for a finer resolution than Fig 5.3. The standard deviation is relatively low compared to the mean for the nanowire segment in between the four magnets, away from the magnet tips. Over the majority of the nanowire the standard deviation is less than 5% of the mean. The provided slices inside the hexagonal nanowire region show the uniformity as well. Full 3D data are available online.

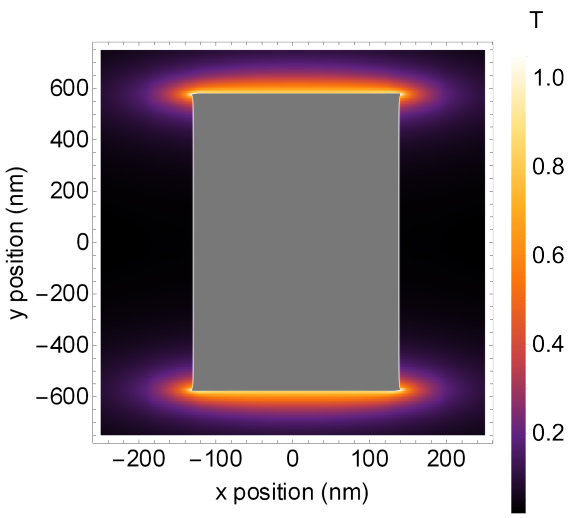

Figure 5.15: A heat map for magnetic field magnitude for a micromagnet of dimensions 230X1000X100 nm. This is shown for a 2D X-Y plane slice through the middle of the micromagnet (50nm), the magnet is shown as grey. Note the field is very weak away from the micromagnet ends. Figure taken from [6].

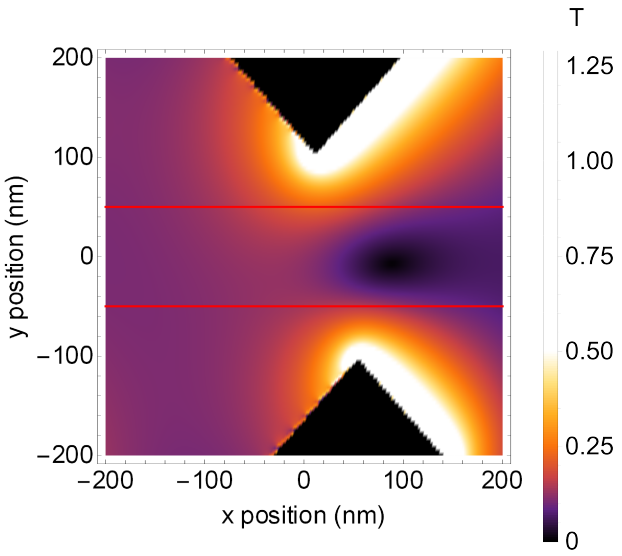

Figure 5.16: A X-Y plane heat map for magnetic field magnitude in a small region near the nanowire, the magnet areas have been set to 0 field (black triangular regions). This is for a 5 nm thick slice in the middle where the nanowire is (marked by red lines). A Mathematica script is available online to look at all the different X-Y slices at different z-positions. Figure taken from [6].

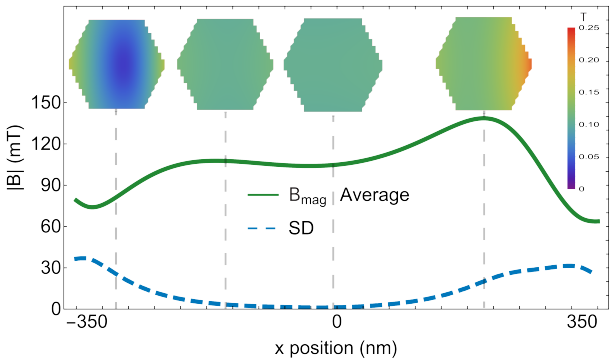

Figure 5.17: Shows the magnetic field magnitude's standard deviation (dashed) across the hexagonal cross-section and mean value over the nanowire region for the single Dragonfly set-up. The insets are field magnitude cross sections of the nanowire at different positions. Note the mean value is the same data that is plotted in Figure 5.3 (b). A Mathematica script is available on Zenodo to look at all Y-Z slices along the nanowire. Figure taken from [6].

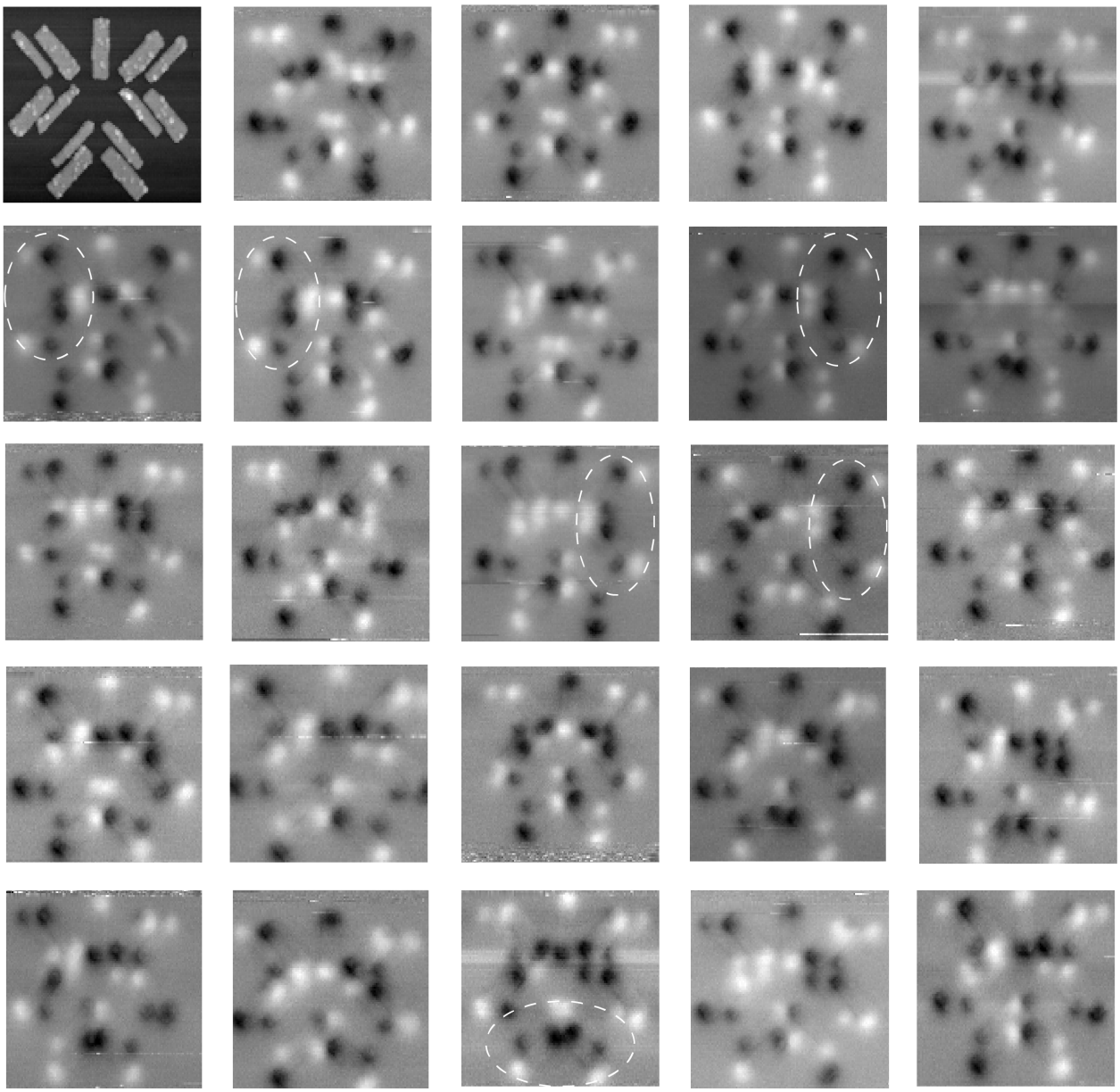

Figure 5.18: Magnetic force microscopy (MFM) data on a 24 T-junction set-ups using three Dragonfly's. The magnet dimensions are the same as in Figure 5.1 but the distance between them differs. Top left: Atomic force microscopy (AFM) of one T-junction setup with three dragonfly magnet configurations. Magnetic film height 20 nm. Dashed ovals point out magnetizations favorable for generating MZM. The magnetic history was a magnetizing field from 100 mT to -16 mT to 0 mT applied at 45 degree direction, then 100 mT to -16 mT to 0 mT at 135 degrees. Figure taken from [6].

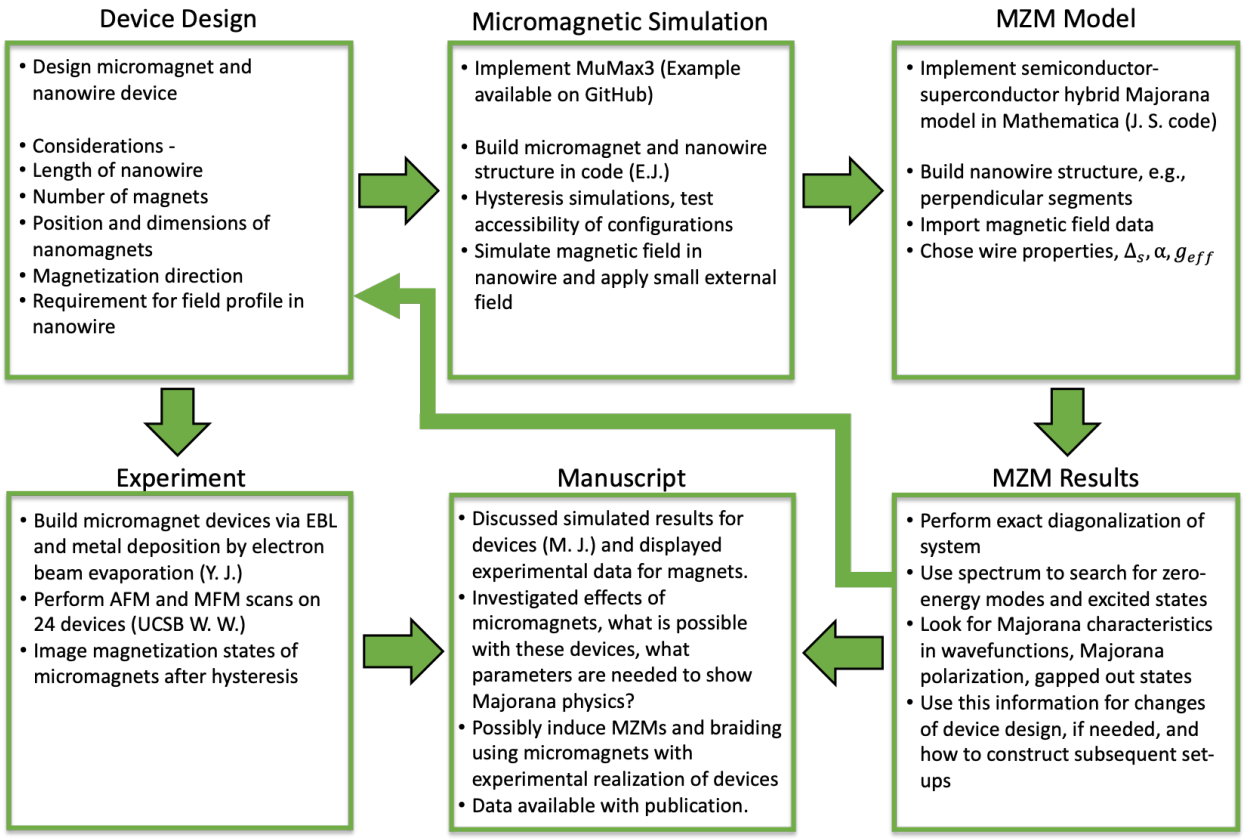

Figure 5.19: **Study design, Volume and Duration of study.** The bulk of the this work was carried out over nine months to find an appropriate micromagnet and nanowire set-up that demonstrated MZMs in the hybrid model. Approximately 5 different single Dragonfly configurations were tested and simulated, which was then used to construct the double Dragonfly and the T-junction. There were around 10 different designs tested for the double Dragonfly and T-junction. The experimental data was collected on a single chip where 24 devices had AFM and MFM measurements taken after an hysteresis cycle was applied to magnetize the configurations. Figure taken from [6].

6.0 Conclusions

This thesis tackled some of the open questions relevant to semiconductor-nanowire/ superconductor hybrid system that are hypothesized to harbour Majorana Zero Modes. It focused on the two questions of: how effective CdTe is as a barrier between the InSb/α-Sn interface, done through the use of Ab Initio DFT calculations; and if micro-scale magnets could be used to supply the magnetic field required for the semiconductor-nanowire/ superconductor system. The former project was motivated by the "metalization" that is thought to happen to the InSb from the metallic superconductor it is interfaced with. This manifests as the InSb losing the required semiconducting properties for realizing MZMs. The goal was to mediate the coupling between the two materials, with the CdTe being a candidate barrier material. The latter project was motivated by the need of local variation of the magnetic field supplied to MZM nanowire experiments, as T-junction configurations require a field parallel to all segments of the nanowire.

The DFT project concluded that a CdTe barrier of 16 layers ($\sim$ 3.5 nm) would provide an effective barrier for the InSb to the electronic effects of α-Sn. To allow the simulation of the electronic properties of the large interface models the DFT+U(BO) method was used, with Hubbard U corrections values machine-learned via a Bayesian optimization (BO) algorithm. The results of DFT+U(BO) were validated against angle resolved photoemission spectroscopy (ARPES) experiments for α-Sn and CdTe, with the z-unfolding method employed to understand the surface-sensitive CdTe ARPES data. Metal Induced Gap States (MIGS) were used to quantify the effect of the barrier.

To test these results an experiment should be done with CdTe shells of varying widths while measuring the induced superconducting gap in an InSb nanowire. With present-day methods, it is not possible to calculate the current across the interface from using these first principle methods. However, it is reasonable to assume that a barrier of 16 layers or more would all but eliminate transport through the interface into the InSb if MZM experiments are carried out using these materials. Therefore, the range of 6-10 barrier layers is the region of interest, as this would allow for some overlap between the wave functions of Sn and the

InSb, leading to the presence of MIGS, and this allows control of the coupling strength between the two materials. However, it is important to note that experiments will use β-Sn due to this phase of Sn being a superconductor. This may differ on important parameters, such the band alignment and the penetration depth of MIGS. With these methods and results the next step is to investigate other material combinations that are relevant for these experiments, with preliminary data already given for the InAs/ZnTe,CdSe/Al trilayer system. Other combinations can be explored following this, building up the knowledge on the interface effects of these material to inform the choice of materials and design of future Majorana experiments. Additionally, the tools and examples here provide understanding for surface-sensitive ARPES data, which can help scientists understand the materials they are growing if they compare the ARPES data with DFT data using these methods.

In the second project, micromagnet and nanowire designs were proposed for use in single wire and T-junction MZM experimental setups. This started with the basic four-magnet design, the Dragonfly configuration, to align magnetic field along the nanowire. This was then copied and manipulated to supply the field for the double Dragonfly setup which showed clearer MZM states at the ends of the nanowire. Following this micromagnets for a nanowire T-junction were simulated, where the micromagnets provided local variation of the stray field. Numerical simulations, using MuMax3, were done to obtain the stray magnetic fields from the different micromagnet configurations. Hysteresis simulations were performed to understand the feasibility of realizing the required micromagnet configurations, and the T-junction micromagnet design feasibility was assessed by performing magnetic imaging of prototype patterns. The stray fields were integrated with the semiconductor-nanowire/ superconductor MZM model and the Majorana wavefunctions and energies were found.

To further this project one could implement a Y-junction or tuning fork nanowire design instead of a T-junction, which could allow for a better and more attainable configuration of the micromagnets, such as having shared micromagnets between the branches. Rather than relying on gate-controlled MZM coupling, an investigation into magnetic field-mediated coupling could be pursued, which could be achieved by flipping micromagnets at the junctions and using external fields. Additionally, one could implement the Poisson-Schrödinger equation to model MZM in the 3D geometry of a single nanowire, which could then be in-

tegrated with 3D stray field data, instead of simplified one-dimensional profiles integrated over the nanowire cross-section. This could yield insights into the combined effects of the non-uniformity of the field, electrostatic confinement, and disorder on the system.

In conclusion, the findings presented in this thesis dissertation offer information to further the progress of semiconductor-nanowire/superconductor Majorana experiments. The realization of Majorana zero modes holds promise for topological quantum computation, but more work needs to be undertaken such that MZM are realized and can be manipulated in experimental setups. As we move forward, the ideas present in this work can be built upon to continue exploring new avenues for improving the stability and controllability of such systems.

Bibliography

[1] Malcolm J. A. Jardine, Derek Dardzinski, Maituo Yu, Amrita Purkayastha, An-Hsi Chen, Yu-Hao Chang, Aaron Engel, Vladimir N. Strocov, Moïra Hocevar, Chris Palmstrøm, Sergey M. Frolov, and Noa Marom. First-principles assessment of cdte as a tunnel barrier at the α-sn/insb interface. *ACS Applied Materials & Interfaces*, 15(12):16288–16298, 03 2023.

[2] Jie Ren, Li Fu, Guang Bian, Manhong Wong, Tao Wang, Gangqiang Zha, Wanqi Jie, T. Miller, M. Z. Hasan, and T.-C. Chiang. Spectroscopic studies of CdTe bulk and surface electronic structure. *Phys. Rev. B*, 91:235303, Jun 2015.

[3] Shuyang Yang, Chunzhi Wu, and Noa Marom. Topological properties of snse/eus and snte/cate interfaces. *Phys. Rev. Materials*, 4:034203, Mar 2020.

[4] S Safaei, M Galicka, P Kacman, and R Buczko. Quantum spin hall effect in IV-VI topological crystalline insulators. *New Journal of Physics*, 17(6):063041, jun 2015.

[5] Hideyuki Ozawa, Ai Yamakage, Masatoshi Sato, and Yukio Tanaka. Topological phase transition in a topological crystalline insulator induced by finite-size effects. *Phys. Rev. B*, 90:045309, Jul 2014.

[6] Malcolm J. A. Jardine, John P. T. Stenger, Yifan Jiang, Eline J. de Jong, Wenbo Wang, Ania C. Bleszynski Jayich, and Sergey M. Frolov. Integrating micromagnets and hybrid nanowires for topological quantum computing. *SciPost Phys.*, 11:90, 2021.

[7] Malcolm Jardine, John Stenger, Eline Jong, and Sergey Frolov. Data and code for "Integrating micromagnets and hybrid nanowires for topological quantum computing". *Zenodo*, July 2021.

[8] Michael Brooks. Quantum computers: What are they good for?, May 2023.

[9] Ashley Montanaro. Quantum algorithms: an overview. *npj Quantum Information*, 2(1):15023, 2016.

[10] IonQ. Improving battery chemistry with quantum computing, Mar 2023.

[11] Experimental Quantum Optics and Photonics Group. Increasing the accuracy of atomic clocks, Mar 2021.

[12] Michael Brooks. What's next for quantum computing, Jan 2023.

[13] Ville Lahtinen and Jiannis K. Pachos. A Short Introduction to Topological Quantum Computation. *SciPost Phys.*, 3:021, 2017.

[14] David Aasen, Michael Hell, Ryan V. Mishmash, Andrew Higginbotham, Jeroen Danon, Martin Leijnse, Thomas S. Jespersen, Joshua A. Folk, Charles M. Marcus, Karsten Flensberg, and Jason Alicea. Milestones toward majorana-based quantum computing. *Phys. Rev. X*, 6:031016, Aug 2016.

[15] Sankar Das Sarma, Michael Freedman, and Chetan Nayak. Majorana zero modes and topological quantum computation. *npj Quantum Information*, 1(1):15001, 2015.

[16] Jason Alicea, Yuval Oreg, Gil Refael, Felix von Oppen, and Matthew P. A. Fisher. Non-abelian statistics and topological quantum information processing in 1d wire networks. *Nature Physics*, 7(5):412–417, 2011.

[17] Chetan Nayak, Steven H. Simon, Ady Stern, Michael Freedman, and Sankar Das Sarma. Non-abelian anyons and topological quantum computation. *Rev. Mod. Phys.*, 80:1083–1159, Sep 2008.

[18] Yuval Oreg, Gil Refael, and Felix von Oppen. Helical liquids and majorana bound states in quantum wires. *Phys. Rev. Lett.*, 105:177002, Oct 2010.

[19] Roman M. Lutchyn, Jay D. Sau, and S. Das Sarma. Majorana fermions and a topological phase transition in semiconductor-superconductor heterostructures. *Phys. Rev. Lett.*, 105:077001, Aug 2010.

[20] Jason Alicea. New directions in the pursuit of majorana fermions in solid state systems. *Reports on Progress in Physics*, 75(7):076501, jun 2012.

[21] Martin Leijnse and Karsten Flensberg. Introduction to topological superconductivity and majorana fermions. *Semiconductor Science and Technology*, 27(12):124003, nov 2012.

[22] S. M. Frolov, M. J. Manfra, and J. D. Sau. Topological superconductivity in hybrid devices. *Nature Physics*, 16(7):718–724, 2020.

[23] Palash B. Pal. Dirac, Majorana, and Weyl fermions. *American Journal of Physics*, 79(5):485–498, 05 2011.

[24] A Yu Kitaev. Unpaired majorana fermions in quantum wires. *Physics-Uspekhi*, 44(10S):131–136, oct 2001.

[25] A. Manchon, H. C. Koo, J. Nitta, S. M. Frolov, and R. A. Duine. New perspectives for rashba spin–orbit coupling. *Nature Materials*, 14(9):871–882, 2015.

[26] Richard M Martin. *Electronic structure: basic theory and practical methods*. Cambridge university press, 2020.

[27] M. Born and R. Oppenheimer. Zur quantentheorie der molekeln. *Annalen der Physik*, 389(20):457–484, 1927.

[28] L. H. Thomas. The calculation of atomic fields. *Mathematical Proceedings of the Cambridge Philosophical Society*, 23(5):542–548, 1927.

[29] Enrico Fermi. Un metodo statistico per la determinazione di alcune priorieta dell'atome. *Rend. Accad. Naz. Lincei*, 6(602-607):32, 1927.

[30] P. Hohenberg and W. Kohn. Inhomogeneous electron gas. *Phys. Rev.*, 136:B864–B871, Nov 1964.

[31] W. Kohn and L. J. Sham. Self-consistent equations including exchange and correlation effects. *Phys. Rev.*, 140:A1133–A1138, Nov 1965.

[32] D.C. Langreth and J.P. Perdew. The gradient approximation to the exchange-correlation energy functional: A generalization that works. *Solid State Communications*, 31(8):567–571, 1979.

[33] David C. Langreth and M. J. Mehl. Beyond the local-density approximation in calculations of ground-state electronic properties. *Phys. Rev. B*, 28:1809–1834, Aug 1983.

[34] A. D. Becke. Density-functional exchange-energy approximation with correct asymptotic behavior. *Phys. Rev. A*, 38:3098–3100, Sep 1988.

[35] John P Perdew, Kieron Burke, and Matthias Ernzerhof. Generalized gradient approximation made simple. *Physical review letters*, 77(18):3865, 1996.

[36] Richard A. Heaton, Joseph G. Harrison, and Chun C. Lin. Self-interaction correction for density-functional theory of electronic energy bands of solids. *Phys. Rev. B*, 28:5992–6007, Nov 1983.

[37] Aron J. Cohen, Paula Mori-Sánchez, and Weitao Yang. Development of exchange-correlation functionals with minimal many-electron self-interaction error. *The Journal of Chemical Physics*, 126(19):191109, 2007.

[38] Victor Polo, Elfi Kraka, and Dieter Cremer. Electron correlation and the self-interaction error of density functional theory. *Molecular Physics*, 100(11):1771–1790, 2002.

[39] Junwei Lucas Bao, Laura Gagliardi, and Donald G. Truhlar. Self-interaction error in density functional theory: An appraisal. *The Journal of Physical Chemistry Letters*, 9(9):2353–2358, 2018. PMID: 29624392.

[40] Paula Mori-Sánchez, Aron J. Cohen, and Weitao Yang. Many-electron self-interaction error in approximate density functionals. *The Journal of Chemical Physics*, 125(20):201102, 2006.

[41] John P. Perdew. Density functional theory and the band gap problem. *International Journal of Quantum Chemistry*, 28(S19):497–523, 1985.

[42] John P. Perdew, Weitao Yang, Kieron Burke, Zenghui Yang, Eberhard K. U. Gross, Matthias Scheffler, Gustavo E. Scuseria, Thomas M. Henderson, Igor Ying Zhang, Adrienn Ruzsinszky, Haowei Peng, Jianwei Sun, Egor Trushin, and Andreas Görling. Understanding band gaps of solids in generalized kohn–sham theory. *Proceedings of the National Academy of Sciences*, 114(11):2801–2806, 2017.

[43] Paula Mori-Sánchez, Aron J Cohen, and Weitao Yang. Localization and delocalization errors in density functional theory and implications for band-gap prediction. *Physical review letters*, 100(14):146401, 2008.

[44] L. J. Sham and M. Schlüter. Density-functional theory of the band gap. *Phys. Rev. B*, 32:3883–3889, Sep 1985.

[45] Jochen Heyd, Gustavo E. Scuseria, and Matthias Ernzerhof. Hybrid functionals based on a screened coulomb potential. *The Journal of Chemical Physics*, 118(18):8207–8215, 2003.

[46] Alejandro J. Garza and Gustavo E. Scuseria. Predicting band gaps with hybrid density functionals. *The Journal of Physical Chemistry Letters*, 7(20):4165–4170, 10 2016.

[47] Jochen Heyd, Juan E Peralta, Gustavo E Scuseria, and Richard L Martin. Energy band gaps and lattice parameters evaluated with the heyd-scuseria-ernzerhof screened hybrid functional. *The Journal of chemical physics*, 123(17):174101, 2005.

[48] Vladimir I Anisimov, Jan Zaanen, and Ole K Andersen. Band theory and mott insulators: Hubbard u instead of stoner i. *Physical Review B*, 44(3):943, 1991.

[49] S. L. Dudarev, G. A. Botton, S. Y. Savrasov, C. J. Humphreys, and A. P. Sutton. Electron-energy-loss spectra and the structural stability of nickel oxide: An lsda+u study. *Phys. Rev. B*, 57:1505–1509, Jan 1998.

[50] J. Hubbard and Brian Hilton Flowers. Electron correlations in narrow energy bands v. a perturbation expansion about the atomic limit. *Proceedings of the Royal Society of London. Series A. Mathematical and Physical Sciences*, 296(1444):82–99, 1967.

[51] Heather J. Kulik. Perspective: Treating electron over-delocalization with the dft+u method. *The Journal of Chemical Physics*, 142(24):240901, 2015.

[52] Matteo Cococcioni and Stefano De Gironcoli. Linear response approach to the calculation of the effective interaction parameters in the lda+ u method. *Physical Review B*, 71(3):035105, 2005.

[53] Maituo Yu, Shuyang Yang, Chunzhi Wu, and Noa Marom. Machine learning the hubbard u parameter in dft+u using bayesian optimization. *npj Computational Materials*, 6(1):180, Nov 2020.

[54] Shuyang Yang, Niels B. M. Schröter, Sergej Schuwalow, Mohana Rajpalk, Keita Ohtani, Peter KrogstrupGeorg, W. Winkler, Jan Gukelberger, Dominik Gresch, Gabriel Aeppli, Roman M. Lutchyn, Vladimir N. Strocov, and Noa Marom. Electronic structure of inas and insb surfaces: density functional theory and angle-resolved photoemission spectroscopy, 2020.

[55] Shuyang Yang, Derek Dardzinski, Andrea Hwang, Dmitry I. Pikulin, Georg W. Winkler, and Noa Marom. First principles feasibility assessment of a topological insulator at the inas/gasb interface, 2021.

[56] Maituo Yu, Saeed Moayedpour, Shuyang Yang, Derek Dardzinski, Chunzhi Wu, Vlad S. Pribiag, and Noa Marom. Dependence of the electronic structure of the EuS/InAs interface on the bonding configuration. *Phys. Rev. Mater.*, 5:064606, Jun 2021.

[57] Peter I. Frazier. A tutorial on bayesian optimization. *arXiv*, jul 2018.

[58] Eric Brochu, Vlad M Cora, and Nando De Freitas. A tutorial on bayesian optimization of expensive cost functions, with application to active user modeling and hierarchical reinforcement learning. *arXiv preprint arXiv:1012.2599*, 2010.

[59] Jasper Snoek, Hugo Larochelle, and Ryan P Adams. Practical bayesian optimization of machine learning algorithms. In *Advances in neural information processing systems*, pages 2951–2959, 2012.

[60] William P Huhn and Volker Blum. One-hundred-three compound band-structure benchmark of post-self-consistent spin-orbit coupling treatments in density functional theory. *Physical Review Materials*, 1(3):033803, 2017.

[61] G. Kresse and J. Hafner. Ab initio molecular dynamics for liquid metals. *Phys. Rev. B*, 47:558–561, Jan 1993.

[62] Sankar Das Sarma, Michael Freedman, and Chetan Nayak. Majorana zero modes and topological quantum computation. *npj Quantum Information*, 1(1):15001, 2015.

[63] V. Mourik, K. Zuo, S. M. Frolov, S. R. Plissard, E. P. A. M. Bakkers, and L. P. Kouwenhoven. Signatures of majorana fermions in hybrid superconductor-semiconductor nanowire devices. *Science*, 336(6084):1003–1007, 2012.

[64] P. Yu, J. Chen, M. Gomanko, G. Badawy, E. P. A. M. Bakkers, K. Zuo, V. Mourik, and S. M. Frolov. Non-majorana states yield nearly quantized conductance in proximatized nanowires. *Nature Physics*, 17(4):482–488, 2021.

[65] G. Kells, D. Meidan, and P. W. Brouwer. Near-zero-energy end states in topologically trivial spin-orbit coupled superconducting nanowires with a smooth confinement. *Phys. Rev. B*, 86:100503, Sep 2012.

[66] S. M. Frolov, M. J. Manfra, and J. D. Sau. Topological superconductivity in hybrid devices. *Nature Physics*, 16(7):718–724, 2020.

[67] Sabbir A. Khan, Charalampos Lampadaris, Ajuan Cui, Lukas Stampfer, Yu Liu, Sebastian J. Pauka, Martin E. Cachaza, Elisabetta M. Fiordaliso, Jung-Hyun Kang, Svetlana Korneychuk, Timo Mutas, Joachim E. Sestoft, Filip Krizek, Rawa Tanta, Maja C. Cassidy, Thomas S. Jespersen, and Peter Krogstrup. Highly transparent gatable superconducting shadow junctions. *ACS Nano*, 14(11):14605–14615, 2020. PMID: 32396328.

[68] M. Pendharkar, B. Zhang, H. Wu, A. Zarassi, P. Zhang, C. P. Dempsey, J. S. Lee, S. D. Harrington, G. Badawy, S. Gazibegovic, R. L. M. Op het Veld, M. Rossi, J. Jung, A.-H. Chen, M. A. Verheijen, M. Hocevar, E. P. A. M. Bakkers, C. J. Palmstrøm, and S. M. Frolov. Parity-preserving and magnetic field-resilient superconductivity in InSb nanowires with Sn shells. *Science*, 372(6541):508–511, 2021.

[69] P. Krogstrup, N. L. B. Ziino, W. Chang, S. M. Albrecht, M. H. Madsen, E. Johnson, J. Nygård, C. M. Marcus, and T. S. Jespersen. Epitaxy of semiconductor–superconductor nanowires. *Nature Materials*, 14(4):400–406, 2015.

[70] Damon J. Carrad, Martin Bjergfelt, Thomas Kanne, Martin Aagesen, Filip Krizek, Elisabetta M. Fiordaliso, Erik Johnson, Jesper Nygård, and Thomas Sand Jespersen. Shadow epitaxy for in situ growth of generic semiconductor/superconductor hybrids. *Advanced Materials*, 32(23):1908411, 2020.

[71] Thomas Kanne, Mikelis Marnauza, Dags Olsteins, Damon J. Carrad, Joachim E. Sestoft, Joeri de Bruijckere, Lunjie Zeng, Erik Johnson, Eva Olsson, Kasper Grove-Rasmussen, and Jesper Nygård. Epitaxial pb on inas nanowires for quantum devices. *Nature Nanotechnology*, 16(7):776–781, 2021.

[72] Fenner Harper, Aakash Pushp, and Rahul Roy. Majorana braiding in realistic nanowire y-junctions and tuning forks. *Phys. Rev. Research*, 1:033207, Dec 2019.

[73] Malcolm J. A. Jardine, John P. T. Stenger, Yifan Jiang, Eline J. de Jong, Wenbo Wang, Ania C. Bleszynski Jayich, and Sergey M. Frolov. Integrating micromagnets and hybrid nanowires for topological quantum computing. *SciPost Phys.*, 11:90, 2021.

[74] Christopher Reeg, Daniel Loss, and Jelena Klinovaja. Metallization of a rashba wire by a superconducting layer in the strong-proximity regime. *Phys. Rev. B*, 97:165425, Apr 2018.

[75] Andrey E. Antipov, Arno Bargerbos, Georg W. Winkler, Bela Bauer, Enrico Rossi, and Roman M. Lutchyn. Effects of gate-induced electric fields on semiconductor majorana nanowires. *Phys. Rev. X*, 8:031041, Aug 2018.

[76] Owen Vail, Alex Chang, Sean Harrington, Patrick Folkes, Patrick Taylor, Barbara Nichols, Chris Palmstrøm, and George de Coster. Gated magnetotransport in α-Sn thin films on CdTe. *Journal of Electronic Materials*, 50(11):6329–6336, 2021.

[77] Christopher Reeg, Daniel Loss, and Jelena Klinovaja. Finite-size effects in a nanowire strongly coupled to a thin superconducting shell. *Phys. Rev. B*, 96:125426, Sep 2017.

[78] Benjamin D. Woods, Sankar Das Sarma, and Tudor D. Stanescu. Subband occupation in semiconductor-superconductor nanowires. *Phys. Rev. B*, 101:045405, Jan 2020.

[79] Benjamin D. Woods, Jun Chen, Sergey M. Frolov, and Tudor D. Stanescu. Zero-energy pinning of topologically trivial bound states in multiband semiconductor-superconductor nanowires. *Phys. Rev. B*, 100:125407, Sep 2019.

[80] Benjamin D. Woods, Tudor D. Stanescu, and Sankar Das Sarma. Effective theory approach to the schrödinger-poisson problem in semiconductor majorana devices. *Phys. Rev. B*, 98:035428, Jul 2018.

[81] Diego Rainis and Daniel Loss. Majorana qubit decoherence by quasiparticle poisoning. *Phys. Rev. B*, 85:174533, May 2012.

[82] Ghada Badawy, Sasa Gazibegovic, Francesco Borsoi, Sebastian Heedt, Chien-An Wang, Sebastian Koelling, Marcel A. Verheijen, Leo P. Kouwenhoven, and E. P. A. M. Bakkers. High mobility stemless InSb nanowires. *Nano Letters*, 19(6):3575–3582, 06 2019.

[83] William S. Cole, S. Das Sarma, and Tudor D. Stanescu. Effects of large induced superconducting gap on semiconductor majorana nanowires. *Phys. Rev. B*, 92:174511, Nov 2015.

[84] Ghada Badawy, Bomin Zhang, Tomáš Rauch, Jamo Momand, Sebastian Koelling, Jason Jung, Sasa Gazibegovic, Oussama Moutanabbir, Bart J. Kooi, Silvana Botti, Marcel A. Verheijen, Sergey M. Frolov, and Erik P. A. M. Bakkers. Electronic structure and epitaxy of CdTe shells on InSb nanowires. *Advanced Science*, 9(12):2105722, 2022.

[85] Ana Suarez Negreira, William G. Vandenberghe, and Massimo V. Fischetti. Ab initio study of the electronic properties and thermodynamic stability of supported and functionalized two-dimensional Sn films. *Phys. Rev. B*, 91:245103, Jun 2015.

[86] Victor A. Rogalev, Tomá š Rauch, Markus R. Scholz, Felix Reis, Lenart Dudy, Andrzej Fleszar, Marius-Adrian Husanu, Vladimir N. Strocov, Jürgen Henk, Ingrid Mertig, Jörg Schäfer, and Ralph Claessen. Double band inversion in α-Sn: Appearance of topological surface states and the role of orbital composition. *Phys. Rev. B*, 95:161117, Apr 2017.

[87] K. H. M. Chen, K. Y. Lin, S. W. Lien, S. W. Huang, C. K. Cheng, H. Y. Lin, C.-H. Hsu, T.-R. Chang, C.-M. Cheng, M. Hong, and J. Kwo. Thickness-dependent topological phase transition and rashba-like preformed topological surface states of α-Sn(001) thin films on InSb(001). *Phys. Rev. B*, 105:075109, Feb 2022.

[88] Zhibin Shi, Xiaoxiong Wang, Caizhi Xu, Peng Wang, Yang Liu, and T.-C. Chiang. First-principles study of the topological surface states ofα-Sn(111). *Physics Letters A*, 384(30):126782, 2020.

[89] Cai-Zhi Xu, Yang-Hao Chan, Yige Chen, Peng Chen, Xiaoxiong Wang, Catherine Dejoie, Man-Hong Wong, Joseph Andrew Hlevyack, Hyejin Ryu, Hae-Young Kee, Nobumichi Tamura, Mei-Yin Chou, Zahid Hussain, Sung-Kwan Mo, and Tai-Chang Chiang. Elemental topological dirac semimetal: α-Sn on InSb(111). *Phys. Rev. Lett.*, 118:146402, Apr 2017.

[90] Huaqing Huang and Feng Liu. Tensile strained gray tin: Dirac semimetal for observing negative magnetoresistance with shubnikov–de haas oscillations. *Phys. Rev. B*, 95:201101, May 2017.

[91] Owen Vail, Patrick Taylor, Patrick Folkes, Barbara Nichols, Brian Haidet, Kunal Mukherjee, and George de Coster. Growth and magnetotransport in thin-film α-Sn on CdTe. *physica status solidi (b)*, 257(1):1800513, 2020.

[92] G. J. de Coster, P. A. Folkes, P. J. Taylor, and O. A. Vail. Effects of orientation and strain on the topological characteristics of CdTe/α-Sn quantum wells. *Phys. Rev. B*, 98:115153, Sep 2018.

[93] Ivan Madarevic, Umamahesh Thupakula, Gertjan Lippertz, Niels Claessens, Pin-Cheng Lin, Harsh Bana, Sara Gonzalez, Giovanni Di Santo, Luca Petaccia, Maya Narayanan Nair, Lino M.C. Pereira, Chris Van Haesendonck, and Margriet J.

Van Bael. Structural and electronic properties of the pure and stable elemental 3d topological dirac semimetal α-Sn. *APL Materials*, 8(3):031114, 2020.

[94] A. Barfuss, L. Dudy, M. R. Scholz, H. Roth, P. Höpfner, C. Blumenstein, G. Landolt, J. H. Dil, N. C. Plumb, M. Radovic, A. Bostwick, E. Rotenberg, A. Fleszar, G. Bihlmayer, D. Wortmann, G. Li, W. Hanke, R. Claessen, and J. Schäfer. Elemental topological insulator with tunable fermi level: Strained α-sn on InSb(001). *Phys. Rev. Lett.*, 111:157205, Oct 2013.

[95] M. R. Scholz, V. A. Rogalev, L. Dudy, F. Reis, F. Adler, J. Aulbach, L. J. Collins-McIntyre, L. B. Duffy, H. F. Yang, Y. L. Chen, T. Hesjedal, Z. K. Liu, M. Hoesch, S. Muff, J. H. Dil, J. Schäfer, and R. Claessen. Topological surface state of $\alpha-$Sn on InSb(001) as studied by photoemission. *Phys. Rev. B*, 97:075101, Feb 2018.

[96] Yoshiyuki Ohtsubo, Patrick Le Fèvre, Fran çois Bertran, and Amina Taleb-Ibrahimi. Dirac cone with helical spin polarization in ultrathin α-Sn(001) films. *Phys. Rev. Lett.*, 111:216401, Nov 2013.

[97] Liang Fu and C. L. Kane. Topological insulators with inversion symmetry. *Phys. Rev. B*, 76:045302, Jul 2007.

[98] Sabbir A. Khan, Sara Martí-Sánchez, Dags Olsteins, Charalampos Lampadaris, Damon James Carrad, Yu Liu, Judith Quiñones, Maria Chiara Spadaro, Thomas S. Jespersen, Peter Krogstrup, and Jordi Arbiol. Epitaxially driven phase selectivity of sn in hybrid quantum nanowires. *arXiv*, page 2212.13314, 2022.

[99] R. F. C. Farrow, D. S. Robertson, G. M. Williams, A. G. Cullis, G. R. Jones, I. M. Young, and P. N. J. Dennis. The growth of metastable, heteroepitaxial films of α-Sn by metal beam epitaxy. *Journal of Crystal Growth*, 54(3):507–518, September 1981.

[100] Huanhuan Song, Jinshan Yao, Yuanfeng Ding, Yu Gu, Yu Deng, Ming-Hui Lu, Hong Lu, and Yan-Feng Chen. Thermal stability enhancement in epitaxial alpha tin films by strain engineering. *Advanced Engineering Materials*, 21(10):1900410, 2019.

[101] A. Davydov, A. Sanna, C. Pellegrini, J. K. Dewhurst, S. Sharma, and E. K. U. Gross. Ab initio theory of plasmonic superconductivity within the eliashberg and density-functional formalisms. *Phys. Rev. B*, 102:214508, Dec 2020.

[102] A. Sanna, C. Pellegrini, and E. K. U. Gross. Combining eliashberg theory with density functional theory for the accurate prediction of superconducting transition temperatures and gap functions. *Phys. Rev. Lett.*, 125:057001, Jul 2020.

[103] Georg W. Winkler, Andrey E. Antipov, Bernard van Heck, Alexey A. Soluyanov, Leonid I. Glazman, Michael Wimmer, and Roman M. Lutchyn. Unified numerical approach to topological semiconductor-superconductor heterostructures. *Phys. Rev. B*, 99:245408, Jun 2019.

[104] Sergej Schuwalow, Niels B. M. Schröter, Jan Gukelberger, Candice Thomas, Vladimir Strocov, John Gamble, Alla Chikina, Marco Caputo, Jonas Krieger, Geoffrey C. Gardner, Matthias Troyer, Gabriel Aeppli, Michael J. Manfra, and Peter Krogstrup. Band structure extraction at hybrid narrow-gap semiconductor-metal interfaces. *Advanced Science*, 8(4):2003087, 2021.

[105] Pedro Borlido, Thorsten Aull, Ahmad W. Huran, Fabien Tran, Miguel A. L. Marques, and Silvana Botti. Large-scale benchmark of exchange-correlation functionals for the determination of electronic band gaps of solids. *Journal of Chemical Theory and Computation*, 15(9):5069–5079, 09 2019.

[106] J. P. Perdew and Alex Zunger. Self-interaction correction to density-functional approximations for many-electron systems. *Phys. Rev. B*, 23:5048–5079, May 1981.

[107] Maituo Yu, Shuyang Yang, Chunzhi Wu, and Noa Marom. Machine learning the hubbard u parameter in dft+u using bayesian optimization. *npj Computational Materials*, 6(1):180, 2020.

[108] Shuyang Yang, Derek Dardzinski, Andrea Hwang, Dmitry I. Pikulin, Georg W. Winkler, and Noa Marom. First-principles feasibility assessment of a topological insulator at the inas/gasb interface. *Phys. Rev. Materials*, 5:084204, Aug 2021.

[109] Michael Rohlfing, Peter Krüger, and Johannes Pollmann. Role of semicore d electrons in quasiparticle band-structure calculations. *Phys. Rev. B*, 57:6485–6492, Mar 1998.

[110] Sebastian Küfner, Jürgen Furthmüller, Lars Matthes, Martin Fitzner, and Friedhelm Bechstedt. Structural and electronic properties of α-tin nanocrystals from first principles. *Phys. Rev. B*, 87:235307, Jun 2013.

[111] Derek Dardzinski, Maituo Yu, Saeed Moayedpour, and Noa Marom. Best practices for first-principles simulations of epitaxial inorganic interfaces. *Journal of Physics: Condensed Matter*, 2022.

[112] Cai-Zhi Xu, Yang-Hao Chan, Peng Chen, Xiaoxiong Wang, David Flötotto, Joseph Andrew Hlevyack, Guang Bian, Sung-Kwan Mo, Mei-Yin Chou, and Tai-Chang Chiang. Gapped electronic structure of epitaxial stanene on InSb(111). *Phys. Rev. B*, 97:035122, Jan 2018.

[113] S. Küfner, M. Fitzner, and F. Bechstedt. Topological α-Sn surface states versus film thickness and strain. *Phys. Rev. B*, 90:125312, Sep 2014.

[114] V. A. Rogalev, F. Reis, F. Adler, M. Bauernfeind, J. Erhardt, A. Kowalewski, M. R. Scholz, L. Dudy, L. B. Duffy, T. Hesjedal, M. Hoesch, G. Bihlmayer, J. Schäfer, and R. Claessen. Tailoring the topological surface state in ultrathin α-Sn(111) films. *Phys. Rev. B*, 100:245144, Dec 2019.

[115] Shuyang Yang, Niels B. M. Schröter, Vladimir N. Strocov, Sergej Schuwalow, Mohana Rajpalk, Keita Ohtani, Peter Krogstrup, Georg W. Winkler, Jan Gukelberger, Dominik Gresch, Gabriel Aeppli, Roman M. Lutchyn, and Noa Marom. Electronic structure of InAs and InSb surfaces: Density functional theory and angle-resolved photoemission spectroscopy. *Advanced Quantum Technologies*, 5(3):2100033, 2022.

[116] Voicu Popescu and Alex Zunger. Extracting $\mathbf{E}$ versus $\vec{k}$ effective band structure from supercell calculations on alloys and impurities. *Phys. Rev. B*, 85:085201, Feb 2012.

[117] Hideaki Iwasawa. High-resolution angle-resolved photoemission spectroscopy and microscopy. *Electronic Structure*, 2(4):043001, dec 2020.

[118] M. P. Seah and W. A. Dench. Quantitative electron spectroscopy of surfaces: A standard data base for electron inelastic mean free paths in solids. *Surface and Interface Analysis*, 1(1):2–11, 1979.

[119] Hongyun Zhang, Tommaso Pincelli, Chris Jozwiak, Takeshi Kondo, Ralph Ernstorfer, Takafumi Sato, and Shuyun Zhou. Angle-resolved photoemission spectroscopy. *Nature Reviews Methods Primers*, 2(1):54, 2022.

[120] Peter J. Feibelman and D. E. Eastman. Photoemission spectroscopy—correspondence between quantum theory and experimental phenomenology. *Phys. Rev. B*, 10:4932–4947, Dec 1974.

[121] V.N. Strocov. Intrinsic accuracy in 3-dimensional photoemission band mapping. *Journal of Electron Spectroscopy and Related Phenomena*, 130(1):65–78, 2003.

[122] Vladimir N. Strocov, Ming Shi, Masaki Kobayashi, Claude Monney, Xiaoqiang Wang, Juraj Krempasky, Thorsten Schmitt, Luc Patthey, Helmuth Berger, and Peter Blaha. Three-dimensional electron realm in vse_2 by soft-x-ray photoelectron spectroscopy: Origin of charge-density waves. *Phys. Rev. Lett.*, 109:086401, Aug 2012.

[123] V. N. Strocov, H. I. Starnberg, and P. O. Nilsson. Excited-state bands of cu determined by vleed band fitting and their implications for photoemission. *Phys. Rev. B*, 56:1717–1725, Jul 1997.

[124] V. N. Strocov, L. L. Lev, F. Alarab, P. Constantinou, T. Schmitt, T. J. Z. Stock, L. Nicolaï, J. Očenášek, and J. Minár. Are high-energy photoemission final states free-electron-like? *arXiv*, page 2301.00033, 2023.

[125] V. N. Strocov, E. E. Krasovskii, W. Schattke, N. Barrett, H. Berger, D. Schrupp, and R. Claessen. Three-dimensional band structure of layered tite
$_2$: Photoemission final-state effects. *Phys. Rev. B*, 74:195125, Nov 2006.

[126] E. E. Krasovskii, V. N. Strocov, N. Barrett, H. Berger, W. Schattke, and R. Claessen. Band mapping in the one-step photoemission theory: Multi-bloch-wave structure of final states and interference effects. *Phys. Rev. B*, 75:045432, Jan 2007.

[127] John P. Perdew, Kieron Burke, and Matthias Ernzerhof. Generalized gradient approximation made simple. *Phys. Rev. Lett.*, 77:3865–3868, Oct 1996.

[128] John P. Perdew, Kieron Burke, and Matthias Ernzerhof. Generalized gradient approximation made simple [phys. rev. lett. 77, 3865 (1996)]. *Phys. Rev. Lett.*, 78:1396–1396, Feb 1997.

[129] S. L. Dudarev, G. A. Botton, S. Y. Savrasov, C. J. Humphreys, and A. P. Sutton. Electron-energy-loss spectra and the structural stability of nickel oxide: An lsda+u study. *Phys. Rev. B*, 57:1505–1509, Jan 1998.

[130] I. Vurgaftman, J. R. Meyer, and L. R. Ram-Mohan. Band parameters for III-V compound semiconductors and their alloys. *Journal of Applied Physics*, 89(11):5815–5875, 2001.

[131] Xiangyang Huang, Eric Lindgren, and James R. Chelikowsky. Surface passivation method for semiconductor nanostructures. *Phys. Rev. B*, 71:165328, Apr 2005.

[132] Leeor Kronik and Stephan Kümmel. *Gas-Phase Valence-Electron Photoemission Spectroscopy Using Density Functional Theory*, pages 137–191. Springer Berlin Heidelberg, Berlin, Heidelberg, 2014.

[133] Aliaksandr V. Krukau, Oleg A. Vydrov, Artur F. Izmaylov, and Gustavo E. Scuseria. Influence of the exchange screening parameter on the performance of screened hybrid functionals. *The Journal of Chemical Physics*, 125(22):224106, 2006.

[134] H. Kumigashira, Hyeong-Do Kim, T. Ito, A. Ashihara, T. Takahashi, T. Suzuki, M. Nishimura, O. Sakai, Y. Kaneta, and H. Harima. High-resolution angle-resolved photoemission study of lasb. *Phys. Rev. B*, 58:7675–7680, Sep 1998.

[135] C. K. Egan, Q. Z. Jiang, and A. W. Brinkman. Morphology and reconstructions of polar CdTe(111)a,b surfaces by scanning tunneling microscopy. *Journal of Vacuum Science & Technology A*, 29(1):011021, 2011.

[136] J Tersoff. Calculation of schottky barrier heights from semiconductor band structures. *Surface Science*, 168:275–284, 1986.

[137] Winfried Mönch. Empirical tight-binding calculation of the branch-point energy of the continuum of interface-induced gap states. *Journal of Applied Physics*, 80(9):5076–5082, 1996.

[138] W. Mönch. Role of virtual gap states and defects in metal-semiconductor contacts. *Phys. Rev. Lett.*, 58:1260–1263, Mar 1987.

[139] Winfried Mönch. Barrier heights of real schottky contacts explained by metal-induced gap states and lateral inhomogeneities. *Journal of Vacuum Science & Technology B: Microelectronics and Nanometer Structures Processing, Measurement, and Phenomena*, 17(4):1867–1876, 1999.

[140] W Monch. On the physics of metal-semiconductor interfaces. *Reports on Progress in Physics*, 53(3):221–278, mar 1990.

[141] Ming Tang, David W. Niles, Isaac Hernández-Calderón, and Hartmut Höchst. Angle-resolved photoemission study of the α-Sn/CdTe(100) interface. *Phys. Rev. B*, 36:3336–3343, Aug 1987.

[142] S. Takatani and Y. W. Chung. Thin-film quantization studies of grey tin epitaxially grown on CdTe(111). *Phys. Rev. B*, 31:2290–2293, Feb 1985.

[143] Hartmut Höchst, David W. Niles, and Isaac Hernández-Calderón. Interface and growth studies of α-Sn/CdTe(110) superlattices. *Journal of Vacuum Science & Technology B: Microelectronics Processing and Phenomena*, 6(4):1219–1223, 1988.

[144] W. R. L. Lambrecht and B. Segall. Interface-bond-polarity model for semiconductor heterojunction band offsets. *Phys. Rev. B*, 41:2832–2848, Feb 1990.

[145] A. Continenza and A. J. Freeman. Band lineup and electric fields in (α-sn)$_m$/(cdte)$_n$ [001] and [110] superlattices. *Phys. Rev. B*, 45:5953–5960, Mar 1992.

[146] Manuel Cardona and Niels E. Christensen. Acoustic deformation potentials and heterostructure band offsets in semiconductors. *Phys. Rev. B*, 35:6182–6194, Apr 1987.

[147] Yoyo Hinuma, Andreas Grüneis, Georg Kresse, and Fumiyasu Oba. Band alignment of semiconductors from density-functional theory and many-body perturbation theory. *Phys. Rev. B*, 90:155405, Oct 2014.

[148] Xingye Wang, Calli Campbell, Yong-Hang Zhang, and Robert J. Nemanich. Band alignment at the CdTe/InSb (001) heterointerface. *Journal of Vacuum Science & Technology A*, 36(3):031101, 2018.

[149] Maituo Yu, Saeed Moayedpour, Shuyang Yang, Derek Dardzinski, Chunzhi Wu, Vlad S. Pribiag, and Noa Marom. Dependence of the electronic structure of the EuS/InAs interface on the bonding configuration. *Phys. Rev. Mater.*, 5:064606, Jun 2021.

[150] P. E. Blöchl. Projector augmented-wave method. *Phys. Rev. B*, 50:17953–17979, Dec 1994.

[151] G. Kresse and D. Joubert. From ultrasoft pseudopotentials to the projector augmented-wave method. *Phys. Rev. B*, 59:1758–1775, Jan 1999.

[152] Jochen Heyd, Gustavo E. Scuseria, and Matthias Ernzerhof. Hybrid functionals based on a screened coulomb potential. *The Journal of Chemical Physics*, 118(18):8207–8215, 2003.

[153] Yelong Wu, Guangde Chen, Youzhang Zhu, Wan-Jian Yin, Yanfa Yan, Mowafak Al-Jassim, and Stephen J. Pennycook. LDA+U/GGA+U calculations of structural and electronic properties of CdTe: Dependence on the effective u parameter. *Computational Materials Science*, 98:18–23, 2015.

[154] G. Fonthal, L. Tirado-Mejía, J.I. Marín-Hurtado, H. Ariza-Calderón, and J.G. Menddoza-Alvarez. Temperature dependence of the band gap energy of crystalline CdTe. *Journal of Physics and Chemistry of Solids*, 61(4):579–583, 2000.

[155] Jörg Neugebauer and Matthias Scheffler. Adsorbate-substrate and adsorbate-adsorbate interactions of na and k adlayers on al(111). *Phys. Rev. B*, 46:16067–16080, Dec 1992.

[156] John Robertson. Band offsets, schottky barrier heights, and their effects on electronic devices. *Journal of Vacuum Science & Technology A*, 31(5):050821, 2013.

[157] Raymond T. Tung. The physics and chemistry of the Schottky barrier height. *Applied Physics Reviews*, 1(1):011304, 01 2014.

[158] Kenji Shiraishi. A new slab model approach for electronic structure calculation of polar semiconductor surface. *Journal of the Physical Society of Japan*, 59(10):3455–3458, 1990.

[159] Xiangyang Huang, Eric Lindgren, and James R Chelikowsky. Surface passivation method for semiconductor nanostructures. *Physical Review B*, 71(16):165328, 2005.

[160] Lu Zhou, Baoxue Bo, Xingzhen Yan, Chao Wang, Yaodan Chi, and Xiaotian Yang. Brief review of surface passivation on iii-v semiconductor. *Crystals*, 8(5), 2018.

[161] Lin-Wang Wang and Jingbo Li. First-principles thousand-atom quantum dot calculations. *Physical Review B*, 69(15):153302, 2004.

[162] Hui-Xiong Deng, Shu-Shen Li, Jingbo Li, and Su-Huai Wei. Effect of hydrogen passivation on the electronic structure of ionic semiconductor nanostructures. *Physical Review B*, 85(19):195328, 2012.

[163] Dominik Kriegner, Christian Panse, Bernhard Mandl, Kimberly A. Dick, Mario Keplinger, Johan M. Persson, Philippe Caroff, Daniele Ercolani, Lucia Sorba, Friedhelm Bechstedt, Julian Stangl, and Günther Bauer. Unit cell structure of crystal polytypes in inas and insb nanowires. *Nano Letters*, 11(4):1483–1489, 04 2011.

[164] Winfried Mönch. *Semiconductor surfaces and interfaces*. Springer, 1995.

[165] S. M. Albrecht, A. P. Higginbotham, M. Madsen, F. Kuemmeth, T. S. Jespersen, J. Nygård, P. Krogstrup, and C. M. Marcus. Exponential protection of zero modes in majorana islands. *Nature*, 531(7593):206–209, 2016.

[166] M. T. Deng, S. Vaitiekenas, E. B. Hansen, J. Danon, M. Leijnse, K. Flensberg, J. Nygård, P. Krogstrup, and C. M. Marcus. Majorana bound state in a coupled quantum-dot hybrid-nanowire system. *Science*, 354(6319):1557–1562, 2016.

[167] Eduardo JH Lee, Xiaocheng Jiang, Manuel Houzet, Ramón Aguado, Charles M Lieber, and Silvano De Franceschi. Spin-resolved andreev levels and parity crossings in hybrid superconductor–semiconductor nanostructures. *Nature nanotechnology*, 9(1):79–84, 2014.

[168] Jelena Klinovaja, Peter Stano, and Daniel Loss. Transition from fractional to majorana fermions in rashba nanowires. *Phys. Rev. Lett.*, 109:236801, Dec 2012.

[169] Jelena Klinovaja and Daniel Loss. Giant spin-orbit interaction due to rotating magnetic fields in graphene nanoribbons. *Phys. Rev. X*, 3:011008, Jan 2013.

[170] Morten Kjaergaard, Konrad Wölms, and Karsten Flensberg. Majorana fermions in superconducting nanowires without spin-orbit coupling. *Phys. Rev. B*, 85:020503, Jan 2012.

[171] MM Desjardins, LC Contamin, MR Delbecq, MC Dartiailh, LE Bruhat, T Cubaynes, JJ Viennot, F Mallet, A Rohart, Thiaville, et al. Synthetic spin–orbit interaction for majorana devices. *Nature materials*, 18(10):1060–1064, 2019.

[172] Narayan Mohanta, Tong Zhou, Jun-Wen Xu, Jong E. Han, Andrew D. Kent, Javad Shabani, Igor Žutić, and Alex Matos-Abiague. Electrical control of majorana bound states using magnetic stripes. *Phys. Rev. Applied*, 12:034048, Sep 2019.

[173] Stefan Rex, Igor V. Gornyi, and Alexander D. Mirlin. Majorana modes in emergent-wire phases of helical and cycloidal magnet-superconductor hybrids. *Phys. Rev. B*, 102:224501, Dec 2020.

[174] Sara Turcotte, Samuel Boutin, Julien Camirand Lemyre, Ion Garate, and Michel Pioro-Ladrière. Optimized micromagnet geometries for majorana zero modes in low g-factor materials. *Phys. Rev. B*, 102:125425, Sep 2020.

[175] L.N. Maurer, J.K. Gamble, L. Tracy, S. Eley, and T.M. Lu. Designing nanomagnet arrays for topological nanowires in silicon. *Phys. Rev. Applied*, 10:054071, Nov 2018.

[176] Yu Liu, Saulius Vaitiekėnas, Sara Martí-Sánchez, Christian Koch, Sean Hart, Zheng Cui, Thomas Kanne, Sabbir Khan, Tanta, Upadhyay, Cachaza Espiñeira, Charles Marcus, Jordi Arbiol, Kathryn A. Moler, and Peter Krogstrup. Semiconductor–ferromagnetic insulator–superconductor nanowires: Stray field and exchange field. *Nano Letters*, 20(1):456–462, 01 2020.

[177] S Vaitiekėnas, Y Liu, P Krogstrup, and CM Marcus. Zero-bias peaks at zero magnetic field in ferromagnetic hybrid nanowires. *Nature Physics*, 17(1):43–47, 2021.

[178] Kim Pöyhönen, Daniel Varjas, Michael Wimmer, and Anton R Akhmerov. Minimal zeeman field requirement for a topological transition in superconductors. *arXiv preprint arXiv:2011.08263*, 2020.

[179] Josias Langbehn, Sergio Acero Gonzalez, Piet W Brouwer, and Felix von Oppen. Topological superconductivity in tripartite superconductor-ferromagnet-semiconductor nanowires. *arXiv preprint arXiv:2012.00055*, 2020.

[180] Aleksei Khindanov, Jason Alicea, Patrick Lee, William S Cole, and Andrey E Antipov. Topological superconductivity in nanowires proximate to a diffusive superconductor-magnetic insulator bilayer. *arXiv preprint arXiv:2012.12934*, 2020.

[181] Arne Vansteenkiste, Jonathan Leliaert, Mykola Dvornik, Mathias Helsen, Felipe Garcia-Sanchez, and Bartel Van Waeyenberge. The design and verification of mumax3. *AIP Advances*, 4(10):107133, 2014.

[182] John P. T. Stenger, Benjamin D. Woods, Sergey M. Frolov, and Tudor D. Stanescu. Control and detection of majorana bound states in quantum dot arrays. *Phys. Rev. B*, 98:085407, Aug 2018.

[183] Javier Osca, Daniel Ruiz, and Lloren ç Serra. Effects of tilting the magnetic field in one-dimensional majorana nanowires. *Phys. Rev. B*, 89:245405, Jun 2014.

[184] Stefan Rex and Asle Sudbø. Tilting of the magnetic field in majorana nanowires: Critical angle and zero-energy differential conductance. *Phys. Rev. B*, 90:115429, Sep 2014.

[185] Y Jiang, E J de Jong, V van de Sande, S Gazibegovic, G Badawy, E P A M Bakkers, and S M Frolov. Hysteretic magnetoresistance in nanowire devices due to stray fields induced by micromagnets. *Nanotechnology*, 32(9):095001, dec 2020.

[186] Liang Jiang, David Pekker, Jason Alicea, Gil Refael, Yuval Oreg, Arne Brataas, and Felix von Oppen. Magneto-josephson effects in junctions with majorana bound states. *Physical Review B*, 87(7):075438, 2013.

[187] C. Bureau-Oxton. Fabrication de nanoaimants pour le contrôle rapide d'un spin électronique dans une boîte quantique double. *Université de Sherbrooke*, 2014.

[188] Georg W. Winkler, Andrey E. Antipov, Bernard van Heck, Alexey A. Soluyanov, Leonid I. Glazman, Michael Wimmer, and Roman M. Lutchyn. Unified numerical approach to topological semiconductor-superconductor heterostructures. *Phys. Rev. B*, 99:245408, Jun 2019.

[189] John P. T. Stenger, Michael Hatridge, Sergey M. Frolov, and David Pekker. Braiding quantum circuit based on the 4π josephson effect. *Phys. Rev. B*, 99:035307, Jan 2019.